Nanoscale Investigations of Thermal and Momentum Transport in Graphene – Water Systems

A Thesis Presented for the
Master of Science
Degree
The University of Tennessee, Knoxville

Drew Champion Marable
May 2017

Copyright © 2017 by Drew Champion Marable
All rights reserved.

ACKNOWLEDGEMENTS

I would like to express my gratitude to my mentor, Dr. Seungha Shin, for his guidance and support throughout my time in graduate school. I would also like to thank my father and mother, Michael and Leslie Marable, my two brothers, Dallas Marable and Alick Yowela, as well as the rest of my family and friends for their encouragement and support. Lastly, a special thanks goes out to my fellow lab mates, Ali Yousefzadi Nobakht and Jiaqi Wang, for their friendship, fruitful conversations, and constructive insight.

ABSTRACT

Demand for miniaturized electronic devices has given rise to new challenges in thermal management. Integration with graphene, a two-dimensional (2D) material with excellent thermal properties, allows for further reduced sizes and combats thermal management issues within novel devices. Moreover, due to its wide availability and adequate thermal properties, liquid water is commonly used within traditional thermal systems to enhance cooling performance; as such, water is expected to yield similar performance in smaller-scale applications. However, at reduced sizes descending to the nanoscale realm, system behaviors deviate from traditional macroscale-based theory as interfacial effects become amplified. Employing insight provided by molecular dynamics simulations, this thesis investigates momentum and thermal transport characteristics, stemming from interfacial interactions, of graphene/water systems to unravel their nanoscale contributions on system-wide thermal performance.

The convective heat transfer process for a laminar flow of liquid water in graphene nanochannels is emphasized as a joint assessment of momentum and thermal transport, with understandings obtained from initial investigations. In preliminary momentum transport analysis, wettability assessments identified graphene/water system behavior as highly dependent on interfacial surface interactions. Extension to flow simulations further revealed that surface interactions significantly impact momentum transport of flowing water behavior and slip development; attributing to the anatomically smooth nature of 2D graphene, slip flow is observed even in cases of extreme hydrophilicity. In thermal transport assessments, increasing surface interactions are shown to enhance heat transfer due to decreased interfacial thermal resistance. In convection heat transfer analysis, momentum and thermal transport are found to be strongly correlated; however, thermal transport was determined to be more influential on resultant system characteristics than momentum transport. Additionally, system size dependence on momentum and thermal transport is observed, with convective performance suggested as the ratio of thermal slip length to system size.

Findings presented in this thesis are expected to enhance knowledge of the physics behind solid/liquid interfacial phenomena and establish more accurate descriptions of nanoscale momentum and thermal transport. Although constrained by limited dimensional/time scales, this work is anticipated to aid in laying the ground work for understanding nanoscale thermal characteristics, with aim at developing novel thermal systems.

TABLE OF CONTENTS

Chapter One Introduction 1
1.1 Significance of Transport Phenomena in Nanoscale Systems 1
1.2 Scope of Work 2
Chapter Two Methodology: Molecular Dynamics 3
2.1 Introduction 3
2.2 Molecular Interactions 3
2.2.1 Force Calculations 3
2.2.2 Force Fields/Pair Potentials 4
2.3 MD Algorithm Implementation 7
2.3.1 Time Integration 7
2.3.2 Boundary Conditions 8
2.3.3 Neighbor Lists 9
2.4 Statistical Sampling Methods 9
2.5 Modelling of Graphene – Water Systems 10
2.5.1 Water: Structure and Modelling 10
2.5.2 Graphene: Structure and Modelling 12
2.5.3 Graphene – Water Systems: Structure and Modelling 13
Chapter Three Surface Interactions and Momentum Transport 15
3.1 Introduction 15
3.2 Surface Interactions and Wettability 15
3.2.1 Introduction to Wettability 15
3.2.2 Wettability Setup and Simulation Details 16
3.2.3 WCA Methodology 16
3.2.4 Wettability Analysis and Deductions 17
3.3 Poiseuille Flow and Viscosity 18
3.3.1 Introduction to Poiseuille Flow and Viscosity 18
3.3.2 Details and Analysis of Water Flow in Graphene Nanochannels 19
3.3.3 Setup and Evaluation of Water Viscosity in MD 21
3.3.4 Viscosity Conclusion 24
3.4 Surface Interactions and Momentum Transport Conclusion 25
Chapter Four thermal Transport I – Interfacial Heat Transfer 26
4.1 Introduction to Interfacial Heat Transfer 26
4.2 Setup and Simulation Details 26
4.3 Interfacial Heat Transfer Analysis 28
4.4 Interfacial Heat Transfer Conclusion 29
Chapter Five Thermal Transport II – Investigation into the Microscopic Mechanisms Influencing Convective Heat Transfer of Water Flow in Graphene Nanochannels 30
5.1 Abstract 30
5.2 Introduction 31
5.3 Methodology 32
5.3.1 Simulation Details 32
5.3.2 Fluid Flow Method 33
5.3.3 Governing Equations 35

5.3.4 Control Parameters 37
5.4 Results and Discussion 38
5.4.1 Velocity and Temperature Development 38
5.4.2 Microscopic Mechanisms 41
5.4.3 Fully-Developed Heat Transfer 43
5.5 Conclusions 47
Chapter Six Conclusions 49
6.1 Summary and Contributions 49
6.2 Possible Extensions 49
6.2.1 Ongoing Work: Convective Heat Transfer in CNTs 49
6.2.2 Ongoing Work: Phase Change 50
6.2.3 Future Work: Desalination 51
6.3 Outlook 51
List of References 53
Appendix 62
LAMMPS 63
Simulation Setup and Pre-Processing 63
Data File 63
Input File: Initialization 63
Input File: Atom Definition 64
Input File: Simulation Settings 65
Input File: Force Field Specifications 65
Input File: Fix Options 67
Input File: Compute Commands 69
Input File: Output Options 69
Data Acquisition and Post-Processing 70
Vita 71

LIST OF TABLES

Table 2.1. AIREBO potential parameters of Stuart et al. [58] employed in the REBO [59] description of graphene intralayer carbon interactions. 6
Table 2.2. Parameter values defining tested water model properties from Refs. [55, 68, 69]..... 12
Table 2.3. Parameter values characterizing graphene – water interaction strength and distance. 14
Table 3.1. Dynamic viscosities for the SPC/E, TIP4P, and TIP4P/2005 water models over a range of temperatures. Error is calculated by $(\mu\text{-}\mu_{ext})/\mu_{ext}$. 24
Table 5.1. Simulation test case parameters. 38

LIST OF FIGURES

Figure 2.1. Simple 2D schematic of simulated atom image replication using periodic boundary conditions. 8
Figure 2.2. (a) Simulated water molecule, and (b) a box of water molecules; the black line defines the periodic boundary of the simulation cell. 11
Figure 2.3. (a) Magnified image of graphene's honeycomb structure, and (b) multiple graphene layers. 12
Figure 3.1. Initial setup for WCA assessment showing 1839 water molecules above a two-layer graphene substrate. 16
Figure 3.2. Sample illustration of fitting a tangent line to determine the resulting WCA. 17
Figure 3.3. Final water droplet configurations for: (a) $\varepsilon_{c\text{-}o}$ = 0.2834 kJ/mol (θ_c = 114°), (b) $\varepsilon_{c\text{-}o}$ = 0.4763 kJ/mol (θ_c = 68°), (c) $\varepsilon_{c\text{-}o}$ = 0.5728 kJ/mol (θ_c = 42°), and (d) $\varepsilon_{c\text{-}o}$ = 1.0553 kJ/mol (θ_c = 0°). 17
Figure 3.4. WCA decrease with carbon – oxygen interaction strength; not shown is the value for $\varepsilon_{c\text{-}o}$ =1.0553 kJ/mol, which is θ_c = 0°. 18
Figure 3.5. Setup of water flow in between two parallel graphene plates; flow is generated by adding a body force, $f_{b,x}$, to each water molecule. 19
Figure 3.6. Velocity profiles with parabolic fitting for water flow with different LJ $\varepsilon_{c\text{-}o}$ values. 20
Figure 3.7. Resulting hydrodynamic slip lengths at the range of interaction strengths (black squares), and their corresponding WCA values (red circles). To better guide the eye and identify trend behavior, curve fitting is applied to slip length relations. 21
Figure 3.8. Water densities across the channel for the range of temperatures using the TIP4P/2005 water model. 22
Figure 3.9. Velocity profiles of the TIP4P/2005 water model at the range of temperatures; quadratic fit lines employed for viscosity calculations are show to better guide the eye. 23
Figure 3.10. Viscosity values as a function of temperature as compared to the interpolated experimental viscosity values; curve fit lines are added to better identify viscosity changes with temperature for each water model. 24
Figure 4.1. Setup schematic for the determination of interfacial thermal resistance. Heat periodically flows from T_h to T_c with the black outline defining the periodic boundary. 27
Figure 4.2. (a) Temperature across one side of the periodic domain, and (b) energy injected/extracted by the thermostated graphene layers. 27
Figure 4.3. Interfacial thermal resistance decrease as a function of interaction strength. 28
Figure 4.4. Magnified liquid water density at the interface for varying levels of C-O interaction strengths ($\varepsilon_{c\text{-}o}$). 29
Figure 5.1. Schematic of the simulation domain separated into three regions: (i) forcing region, (ii) temperature rescaling region, and (iii) data collection region. 34
Figure 5.2. Maxwell-Boltzmann (MB) velocity distributions. The blue open circles and red cross markers represent that of the *x*- and *z*-axis distributions from MD, respectively; the black solid line corresponds to the MB distribution curve at 300 K. 35
Figure 5.3. Velocity distribution across the dimensionless channel height ($z^* = z/H$, and H = 5.0 nm) with various wall-fluid interaction strengths ($\varepsilon_{c\text{-}o}$). With increasing $\varepsilon_{c\text{-}o}$, average velocity decreases while the parabolic curvature increases. 39

Figure 5.4. Temperature development inside a nanochannel with dimensions of 22.0×3.0×7.0 nm^3. (a) Isotherm diagram of temperature development (isothermal lines are inverted to better guide the eye.) (b) Non-dimensional mean temperature (θ_m) development in the *x*-axis flow direction. (c) Development of non-dimensional (θ) temperature profiles across the channel height (*z*-axis) at various *x*-directional points in the direction of the flow..... 39
Figure 5.5. Flow development with axial conduction at different Peclet numbers showing (a) mean dimensionless temperature (θ_m) development, (b) dimensionless temperature gradient ($\partial\theta/\partial z^*$) at the wall, (c) comparison of local surface (q_s''), surface water conduction (q_k''), change of surface advection (q_u''), and viscous (q_v'') heat flux and (d) local Nusselt number (Nu_D). 40
Figure 5.6. Thermal (l_k) and hydrodynamic (l_s) slip lengths for varying (a) interaction strengths ($\varepsilon_{c\text{-}o}$), (b) channel heights (H), (c) velocities ($u_{f,avg}$), and (d) wall temperatures (T_w); fit lines are added to better guide the eye..... 42
Figure 5.7. Fully-developed Nusselt number ($Nu_{D,fd}$) trends for varying (a) interaction strength ($\varepsilon_{c\text{-}o}$), (b) channel height (H), (c) water velocity ($u_{f,avg}$), and (d) wall temperature (T_w)..... 44
Figure 5.8. Density profiles for increasing values of solid-fluid interaction strengths ($\varepsilon_{c\text{-}o}$). The inset is a magnified image of density at the interfacial region. 45
Figure 5.9. (a) Fully-developed $Nu_{D,fd}$ trends for increasing channel heights (H) at different carbon-oxygen interaction strengths ($\varepsilon_{c\text{-}o}$). (b) Comparison of l_s and l_k for all test parameters. (c) $Nu_{D,fd}$ values corresponding to normalized hydrodynamic slip lengths. (d) Fully developed $Nu_{D,fd}$ trend for normalized thermal slip length values..... 46
Figure 6.1. Setup of water in a CNT for convection assessment..... 50
Figure 6.2. Snap shots of water boiling on a heated graphene substrate over a period of time, *t*. 50
Figure 6.3. Periodic freezing of a graphene flake – water solution over a span of time, *t*. 51
Figure 6.4. (a) Initial setup of salt water solution on top of a porous graphene structure, and (b) ion migration through porous graphene structure..... 51

CHAPTER ONE

INTRODUCTION

Demand for miniaturized, high power and efficient electronics devices has spurred many research efforts and beneficial innovations within the industry. However, as researchers push towards sizes descending into the micro- and nano-scale level, difficulties in thermal management and heat dissipation become of increasing concern [1]. To combat these issues, investigators have looked to new materials and techniques as potential avenues to mitigate excessive heat build-up.

At the turn of the century, new developments in experimental synthesis presented new opportunities in the form of exploration into the characteristics of two-dimensional (2D) materials (e.g., graphene, h-BN, MoS_2, etc.). From initial and subsequent research endeavors, graphene, in particular, was hailed as a "novel" material with immense applicational potential due to its excellent thermal and electrical conductive properties [2-4]. Parallel to these events in the early 2000s, computational capabilities also exploded during this time period. Allowing for more affordability and thus, accessibility to numerically-based studies, researchers capitalized on utilizing computational means to circumvent the costly procedures of experimental efforts. Moreover, computational simulations afforded researchers a vast number of investigational possibilities into the exploration of numerous dimensional and time scales (i.e., quantum, molecular, meso, etc.) for insight on minute details otherwise unaccounted for within experiments. Stemming from this, many different methods have been proposed as solutions to scientific and engineering conundrums; namely, the utilization of nano-/micro- structuring and material interactions with fluids to alleviate excessive heat buildup within small dimensional scales [5, 6].

When dimensional sizes are decreased to the nanoscale level, the fundamental principles of fluid and thermal dynamics are shown to deviate from their theorized macroscale or continuum behavior [7-17]. Therefore, fundamental understandings of the mechanisms behind these phenomena must be uncovered to enable utilization of past research developments within innovative applicational areas.

1.1 Significance of Transport Phenomena in Nanoscale Systems

Transport phenomena pertains to the exchange of energy, mass, and momentum transfer within a system of interest. All of which are based on similar mathematical frameworks to provide fundamental analysis within engineering, physics, chemistry, etc. Over the past few hundred years, investigations into the interworkings of energy, mass, and momentum transfer have developed extensive mathematical behavioral descriptions of transport phenomena and processes (e.g., heat conduction [energy transfer], molecular diffusion [mass transfer], and fluid flow [momentum transfer]). These investigations have led to universally accepted conservation laws and theories based on continuum approximations such as the Laws of Thermodynamics, Fourier's Law of Heat Conduction, the Navier-Stokes equations, Newton's Laws of Viscosity, Fick's Laws of Diffusion, and many more.

Developments in computational abilities and numerical assessments have enabled for evaluations of fundamental particle behaviors at decreased dimensional scales. The conduct and mannerisms of particles and atomistic interactions act as the basis for outward macroscale characteristics of any particular media, and are what provides the foundation for theoretical laws and continuum descriptions. As researcher began to investigate the application of macroscale

theories for the description of nanoscale molecular behavior, many studies found deviations from hypothesized conduct [12, 16]. Within studies of individual solid and liquid media interactions, in addition to interactions between the two, contact interfaces were found to be of critical importance within the determination of thermal properties and resultant momentum-based characteristics [18]. Namely, nonconformity to the continuum based no-slip boundary condition was observed within viscous flows on incompressible liquids [8, 9, 12, 13, 19-21], and temperature discontinuity was reported to occur at nanoscale interfaces [22-26]. As such, contributions of interfacial interactions and their effects can significantly affect observed material properties; these effects become amplified within nanoscale systems and can lead to considerable property augmentation relative to that of bulk materials. Thus, as dimensional scales of thermal and electronic devices continue to decrease, it is of great importance to understand the fundamental mechanisms behind interfacial effects on momentum and thermal transport, and their subsequent projection of influence on systems outward expression of observed properties.

1.2 Scope of Work

Within the scope of this thesis, momentum and thermal transport phenomena between graphene and liquid water are investigated via MD simulations utilizing LAMMPS [27]. Graphene is chosen for its highly conductive properties and 2D nature that allows for its structure to be manipulated for specific applicational requirements. Liquid water is selected as the investigated fluid due to its widely common use within traditional thermal transport and heat dissipation systems. In order to achieve successful exploration of thermal and momentum transport interworkings, one must acquire and build upon knowledge necessary to implement and accomplish an effective investigation. This thesis first details the principles behind molecular dynamics simulations, of which is extensively employed to conduct this research. Next, a layout of MD algorithm implementation and the simulated systems of interest, are described. The next two chapters describe simulation methods and analysis of investigations into wettability, fluid flow in nanochannels, and heat transfer within graphene – water interacting systems; these Chapters act as the building blocks to conducting and analyzing the following chapter detailing convective heat transfer in graphene nanochannels. Following these, ongoing and future work on convection in carbon nanotubes, confined – water phase change, and desalination is presented. Lastly, this thesis' concluding remarks are stated.

CHAPTER TWO

METHODOLOGY: MOLECULAR DYNAMICS

2.1 Introduction

In the world of computational simulations and numerical research that span a vast range span time and length scales, molecular dynamics (MD) provides an ability to investigate the nanoscale time evolution of Newtonian-based atomistic movements and subsequent interactions. Within an MD simulation, for any given molecular system of interacting particles (governed by potential models), Newton's equations of motion are numerically integrated to yield atom trajectories and other quantities (thermodynamic, force, pressure, etc.) for the evaluation of properties of interest. The uniqueness of MD resides in its capability to "bridge-the-gap" between quantum- and meso- scales, in addition to theory and experiment as it facilitates the direct observation of simulated molecular-level phenomena. MD investigations have broad application to inter-disciplinary study, including, but not limited to, biomechanics, polymers and materials, chemistry, fluid dynamics, heat transfer and thermodynamics, and phase transitions.

MD simulations have been widely employed for the analysis of the individual behaviors of both graphene [28-31] and water [32-35], in addition to contacts between the two media [36-39]. Within numerous research efforts, MD has emerged as the method of choice to investigate graphene's fundamental properties and uncovering its applicational abilities. Water properties of all (solid [40, 41], liquid [34, 35], and gaseous [42, 43]) phases have been extensively investigated with MD techniques, and more recently simulations have begun to explore graphene – water interactions to characterize graphene surface characteristics [44-48], fluid flow behaviors [21, 49], and heat transfer performance [23, 50].

This chapter seeks to form a detailed understanding of the methodologies and approaches required for simulations of complex molecular systems (i.e., a vast number of interacting atoms within a system of dissimilar media) in three-dimensional space. Central to the implementation of MD simulation procedures, the force calculations that dictate resulting atomistic interactions and their ensuring behavior are first introduced; time integration techniques used to update subsequent particle positions after interaction are then discussed. Furthermore, avenues of simulation optimization are presented as increasingly complex systems can become more computationally demanding. The chapter concludes with explanations of statistical sampling thermodynamic properties for data acquisition and reliability, and modeling systems of interest, in MD.

2.2 Molecular Interactions

2.2.1 Force Calculations

The core tenant of molecular dynamics simulations relies upon numerically solving the classical Newton's equations of motion in a step-by-step manner to obtain realistic predictions of particle movements and interactions therein. As each atom (or molecule) within a system must satisfy Newton's Law, $F = ma$, particle motion (represented by particle position, velocity, and acceleration) is determined from subsequent interaction forces acting on atoms by:

$$F = -\nabla U(r), \tag{2.1}$$

and

$$m\frac{d^2r}{dt^2} = -\frac{dU(r)}{dr}, \tag{2.2}$$

where m is the particle mass, a is a particle's acceleration, t is time, r is the set of $3N$ coordinates and $U(r)$ is the potential energy function. The potential energy function characterizes system-wide energy produced from particle interactions described by the interatomic potential, and is a fundamental constraint within the determination of system behavior as forces are derived from resulting potential energy. Therefore, the interatomic potential model must accurately characterize particle interactions to correctly estimate system behaviors.

2.2.2 Force Fields/Pair Potentials

Many interatomic potential models exist within MD to provide the potential energy function, $U(r)$, with the essential physics of particle-particle interaction characteristics [51]. Based on the N-body problem where each body is representative of a finite particle [52], $r = (r_1, r_2, \ldots, r_N)$, interaction potential models range in form and are selected to describe numerous systems of interest, with each delivering varying levels of accuracy and computational efficiency. Interatomic potential models can be loosely broken down into two main classifications: Pair Potentials and Many-Body Potentials (these also encompass Bond Order Potentials).

Pair Potentials: Utilization of pair potentials is most simple and computational efficient method of describing non-bonded interactions between two particles. In this model, only pairwise Lennard-Jones (LJ) [53] interactions between two particles of interest are considered with the potential energy depending on the distance, or cutoff radius, between the two entities. Although pair potential models can lack in accurately describing all essential behaviors and properties of some materials and fluids, these models can sufficiently represent vital physics necessary in simulations of complex fluids and systems. Therefore, pair potentials are utilized with the modeling of inter layer graphene – graphene and graphene – water interactions, in addition to interatomic interactions between water molecules. Although employing mixing rules and procedures are of common use for describing nonhomogeneous molecular interactions, more accurate parameters from literature are utilized in this thesis to better characterize system behaviors. Specific modeling parameters and values characterizing all interactions that employing the pair potential type will be later identified.

Within force calculations, pair potentials are employed to determine the resultant potential energy function between two interacting bodies; in particular, this potential type is employed for determining water – water and graphene – water interactions. As previously mentioned, pair potentials are employed over that of more complex many-body potentials for computational efficiency and their ability to accurately represent physics in a sufficient manner. Potential energy for interactions between two bodies, the simplest pair potential function for describing atomistic interactions, is defined as the sum of pairwise interactions between two particles i and j, at their respective positions, r_i and r_j, by:

$$U_{LJ}(r_{ij}) = \sum_i \sum_{j>i} U(r_{ij}), \tag{2.3}$$

where $r_{ij} = r_i - r_j$ and $r_{ij} = |r_{ij}|$.

The most commonly used pair potential function is the 12-6 Lennard-Jones (LJ) [54] potential as a representation for repulsion and van der Waals forces, written as:

$$U_{LJ}(r_{ij}) = 4\varepsilon_{ij}\left[\left(\frac{\sigma_{ij}}{r_{ij}}\right)^{12} - \left(\frac{\sigma_{ij}}{r_{ij}}\right)^{6}\right], \tag{2.4}$$

where ε_{ij} and σ_{ij} are the LJ interaction energy strength and distance at which the potential energy is zero between two particles, and r_{ij} is the distance between the two particles. Although simple in form, the 12-6 LJ potential is adequate in the of description of non-bonded interactions between two bodies. Moreover, this potential function can be varied with modifications to better describe long and short ranged intermolecular interactions by means of truncation and/or including electrostatic charges. As is required by most water model descriptions [55], for additions of molecular charge within the potential function, a Coulombic (or electrostatic) potential term for pairwise interactions is included as:

$$U_{C}(r_{ij}) = \sum_{i<j} \frac{q_i q_j}{4\pi\varepsilon_0 r_{ij}}, \tag{2.5}$$

where q_i and q_j are the respective charges of two particles, i and j, ε_0 is the permittivity of free space.

Many-Body and Bond-Order Potentials: Many-body "pairwise" potentials are widely employed to describe interactions involving bonded elements (e.g., metals and biological materials) within MD simulations. These types of potentials (EAM [56], Stillinger-Weber [57], AIREBO [58], Brenner [59, 60], Tersoff [61], etc.) can take into account potential energy changes attributed to bond bending by atom displacement from subsequent acting forces, as well as local atoms within the neighboring environment. Moreover, as an offshoot of many-body potentials, bond-order potentials (AIREBO, Brenner, Tersoff, etc.), which are particularly employed within this thesis, also take into account neighboring atoms and bond bending; they further this by describing atom bonding states and bond strength between two atoms and also account for environmental influences on atom and bond behaviors within the potential energy [58]. Derived from density function theory (DFT) simulations and quantum mechanical data, bond-order potentials are primarily employed in the modeling of chemical reactions and strongly bonded materials as they can accurately replicate bond breaking/formation [58, 59, 61, 62]. Thus, as graphene, being a strongly covalently-bonded material, is extensively simulated within this thesis' investigations, these types of bond-order potentials are employed to model the intralayer C-C interactions within a graphene sheet. It must be noted that many-body potentials are not further covered as they do not fall within the scope of this thesis.

In cases of more complex systems, bond-order potentials, as an offshoot of many-body potentials, are employed for force calculations of bonded elements. Many bond-order potentials exist and range in description of bonded element behaviors; in particular, the Adaptive Intermolecular Reactive Empirical Bond Order (AIREBO) potential was developed by Stuart et al. [58] to characterize a system of interacting carbon and/or hydrogen atoms. This bond-order potential was developed to describe carbon-containing nanostructures and is well suited for the modeling of carbon nanotubes and graphene [47, 63, 64], and is utilized in this thesis. Represented by the sum of pairwise interactions and consisting of three separate terms, the AIREBO potential includes covalently bonded interaction energy, LJ terms, and torsional terms, written as:

$$E = \frac{1}{2}\sum_{i}\sum_{j\neq i}\left[E_{ij}^{REBO} + E_{ij}^{LJ} + \sum_{k\neq i,\, jl\neq i,\, j,k}\sum E_{ij}^{TORSION} \right]. \tag{2.6}$$

In this equation, the REBO energy term [59] is employed to describe covalently bonded pairwise interactions as:

$$E_{ij}^{REBO} = U_{ij}^{R} + b_{ij}U_{ij}^{A}, \tag{2.7}$$

where U_{ij}^{R} and U_{ij}^{A} are the repulsive and attractive pairwise potentials between atoms *i* and *j* of the specified atom type (carbon in the instance of this thesis), and b_{ij} is the bond order term used to modify the bonding strength between atoms *i* and *j* due to local environmental changes. Moreover, the repulsive and attractive pairwise potentials within the REBO energy term of Eq. (2.7) are respectively defined as:

$$U_{ij}^{R} = w_{ij}(r_{ij})\left[1 + \frac{Q_{ij}}{r_{ij}}\right]A_{ij}e^{-\alpha_{ij}r_{ij}}, \tag{2.8}$$

and

$$U_{ij}^{A} = -w_{ij}(r_{ij})\sum_{n=1}^{3} B_{ij}^{(n)}e^{-\beta_{ij}^{(n)}r_{ij}}, \tag{2.9}$$

where Q_{ij}, A_{ij}, α_{ij}, $B_{ij}^{(n)}$, and $\beta_{ij}^{(n)}$ depend on the atom type (carbon); these parameter values are given in Table 2.1. As the REBO energy term is short-ranged in nature, the w_{ij} term acts as a flag to either include and exclude REBO interactions when the distance between atoms pairs exceed that of their bonding distance.

Table 2.1. AIREBO potential parameters of Stuart et al. [58] employed in the REBO [59] description of graphene intralayer carbon interactions.

CC Interaction Parameter	CC Value*	Eq. No.
Q_{ij} (nm)	0.031346	(2.8)
α_{ij} (nm^{-1})	47.465391	(2.8)
A_{ij} (kJ/mol)	252594.6609	(2.8)
$B_{ij}^{(1)}$ (kJ/mol)	285692.2576	(2.9)
$B_{ij}^{(2)}$ (kJ/mol)	405.1060393	(2.9)
$B_{ij}^{(3)}$ (kJ/mol)	708.3029777	(2.9)
$\beta_{ij}^{(1)}$ (nm^{-1})	47.204523	(2.9)
$\beta_{ij}^{(2)}$ (nm^{-1})	14.332132	(2.9)
$\beta_{ij}^{(3)}$ (nm^{-1})	13.826913	(2.9)
ε_{ij} (kJ/mol)	0.065491939	(2.4)
σ_{ij} (nm)	0.340	(2.4)

*Original values given in units of (Å) and (eV) are converted to (nm) and (kJ/mol) for consistency

The Lennard Jones (LJ) energy term in Eq. (2.6) includes the LJ energy contribution to the pair of atoms *i* and *j*, and is written as:

$$E_{ij}^{LJ}(r_{ij}) = S\left(t_r\left(r_{ij}\right)\right)S\left(t_b\left(b_{ij}^{*}\right)\right)C_{ij}U_{ij}(r_{ij}) + \left[1 - S\left(t_r\left(r_{ij}\right)\right)\right]C_{ij}U_{ij}\left(r_{ij}\right), \tag{2.10}$$

where U_{ij} is the LJ term defined in Eq. (2.4), which is modified by switching functions, S(t), to adaptively switch on or off the LJ interaction term depending on atom distance, bond strength, and connecting bonds. The $S(t_r(r_{ij}))$ term adjusts LJ interactions between two atoms based on their distance apart, and the $S(t_b(b_{ij}^{*}))$ term modifies LJ interactions of an atom pair depending on their

bond strength. $t_r(r_{ij})$ and $t_b(b_{ij}^*)$ act as scaling terms; b_{ij}^* is the bond order term for nonbonded interactions.

The energy attributed to the torsion term in Eq. (2.6) accounts for dihedral angle contributions to the total energy as:

$$E_{kijl}^{TORSION} = w_{ki}(r_{ki})w_{ij}(r_{ij})w_{jl}(r_{jl})U^{TORSION}(w_{kijl}), \tag{2.11}$$

with

$$U^{TORSION}(w_{kijl}) = \frac{256}{405}\varepsilon_{kijl}\cos^{10}\left(\frac{w_{kijl}}{2}\right) - \frac{1}{10}\varepsilon_{kijl}, \tag{2.12}$$

where $w_{kijl}(r_{kijl})$ are the bonding weights that are employed to efficiently remove dihedral angle torsional energy when bonds are broken; the value of parameter ε_{kijl} is given in Table 2.1.

While the AIREBO potential was employed for initial assessment, this description was found to be exceed the requirements of this thesis' investigations as it caused unnecessary computational efforts due to its long-ranged nature and inclusion of torsion terms. Thus, the 2nd Generation Tersoff-Brenner potential (also known as REBO) [59] is selected to replace the use of the AIREBO potential to model graphene. With the exception of a few spline fitted values [59], the REBO and AIREBO potentials are closely related and very similar in recreation of graphene behaviors (energies, forces, statistical averages, etc.) as REBO employs the same REBO and LJ energy terms from the AIREBO potential. However, the major difference between the two falls on REBO being short-ranged in nature where AIREBO is long-ranged [58, 59]. Since graphene – water interactions are modelled via the pairwise 12-6 LJ potential (as hydrogen atoms are accounted for within SPC/E and TIP4P-iteration water models), and as torsion contributions associated with C-C bond breaking are not expected to occur within the scope of these investigations, the use of REBO to sufficiently model intralayer C-C interactions that constitute a single layer graphene sheet, is justified.

2.3 MD Algorithm Implementation

2.3.1 Time Integration

Within solving the previously aforementioned force calculations, MD utilizes integration methods to accurately forecast system evolution and behavior over time. Adhering to the satisfaction of Newton's laws, while taking into consideration prescribed initial and boundary conditions, interatomic potential models, and thermodynamic constraints, MD generates atomistic trajectories for a system of interacting particles to predict subsequent accelerations $a(t)$, positions $r(t)$, and velocities $v(t)$ of each particle.

The Velocity Verlet [65] algorithm is widely employed for time integration within MD simulations, and within the scope of this thesis, is selected as the method of choice to determine atomistic trajectories due to excellent performance at energy conservation [51]. This Verlet algorithm employs particle accelerations, positions, and velocities from the previous time step, Δt, to generate new particle accelerations, positions, and velocities at each time step iteration. Accelerations are determined from the subsequent forces obtained by solving Newton's seconds law of motion at any particular time, t, by:

$$a_i(t) = \frac{F_i[r_i(t)]}{m}. \tag{2.13}$$

Employing Eq. (2.13) leads to the determination of updated particle positions and velocities as:

$$r_i(t+\Delta t) = r_i(t) + v_i(t)\Delta t + \frac{1}{2}a_i(t)\Delta t^2, \tag{2.14a}$$

where

$$v_i(t+\Delta t) = v_i(t) + \frac{1}{2}\left(a_i(t) + a_i(t+\Delta t)\right)\Delta t. \tag{2.14b}$$

Furthermore, the Verlet integration method directly includes computations of the velocity component to provide velocities at every time step for each particle; thus, calculations of kinetic energy can be implemented with a high order of accuracy, which is vital statistical sampling within MD.

2.3.2 Boundary Conditions

Crucial to most all experimental examinations, no matter the field of study, is the initial setting of boundary conditions to aid in determining mathematical solutions; molecular dynamics investigations are no exception to this. The ultimate goal of MD is to evaluate underlying physics at the atomistic scale for translational application to larger dimensions; however, when simulating an increasing number of atoms, computational resources can become very costly and lack in meaningful results when simulation times are insufficient to fully realize system behaviors. To combat this, MD employs the core concept of modeling a simulation cell of atoms as an infinite system by means of introducing periodic boundary conditions (PBCs).

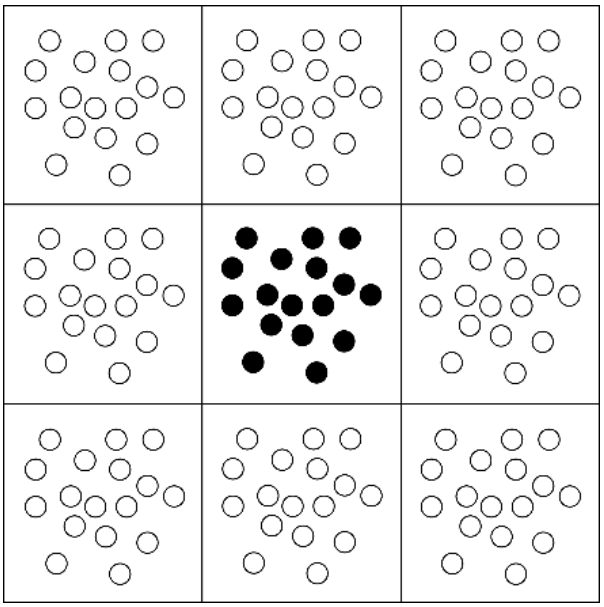


Figure 2.1. Simple 2D schematic of simulated atom image replication using periodic boundary conditions.

PBCs allow for small sample sizes to have increased translational ability of results while retaining computational and cost efficiency that would otherwise be increased when assessing larger sample sizes. PBCs are introduced by surrounding the initial simulation cell box with replica boxes in the *x*-, *y*-, and *z*- axis directions to form an infinite array of the simulated cell, similar to that shown in Fig. 2.1. When particles interact and the resulting collision sends a particle toward a periodic wall, the moving particle will continue across the periodic boundary and re-enter on the

opposite side of the box, or its periodic image. Within this, particles interact with neighboring particles at a specified distance, r_c, from the boundary; this also includes interactions with particles across the periodic image. Moreover, prescribing correlated long-range interactions can lead to the negative influence of a particle interacting with multiple periodic images; thus, care must be taken to account for the influence of periodic phenomena by considering these effects in the time integrated force calculations.

2.3.3 Neighbor Lists

Bearing in mind all the computational expensive constraints an MD algorithm must consider to determine interaction forces between two particles (e.g., potential models, time integration, boundary conditions, etc.), neighbor lists are introduced as a form of bookkeeping to evaluate pairwise calculations. As the distance between any two particles/atoms within a simulation cell increases, their projection of influence on one another becomes increasingly insignificant within force calculations; if one considered forces for all atom pairs, unneeded computational efforts would be wasted as these contributions would be miniscule within resultant force calculations. Thus, neighbor lists are built to only consider atom pairs within a specified cutoff distance, r_c, and exclude interactions beyond that value to increase computational efficiency. This is done by considering each atom, i, and iteratively determining its minimum separation distance, r_{ij}, from all other atoms, j. If long range interactions are specified within the potential definition, pairwise interaction forces will be considered while taking into account their separation distance. If a short-ranged interaction potential is specified where $r_{ij} > r_c$, force calculations beyond this range are ignored and the program loops to the next particle, j; however, as all atom pairs must be considered, this method is still computationally demanding.

To increase computational efficiency, Verlet [65] developed a technique to further the use of the separation length, r_{ij}, for neighbor list construction by introducing an additional distance (or "skin" distance), Δr, to the potential cutoff sphere, r_c, as $r_{ij} = r_c + \Delta r$ where only atoms within the sphere of r_{ij} are considered for their contribution to force calculations, while all other are excluded. It is obvious that the addition of a skin distance increases an atom's sphere of influence, r_{ij}. However, in the process of iteratively identifying neighbors and determining interacting pairs for the resultant list build of r_{ij} over a specified period of timesteps, this Δr term acts as a buffer to ensure that no new atom pairs are added to the pairwise neighbor list over the next few timesteps. By safeguarding against the addition of new interacting atom pairs within the looping process, computational efficiency is increased.

2.4 Statistical Sampling Methods

Statistical sampling methods are utilized as a key metric within MD simulations to determine thermodynamic properties of interest (e.g., temperature, pressure, energy, etc.). To do this, properties are calculated via some form of averaging to obtain key values from the time and/or ensemble averaging methods introduced in statistical mechanics [51]. For the determination of an arbitrary property, A, evolving over a period of time, M, the time average is defined as:

$$\langle A \rangle_{Time} = \frac{1}{M} \sum_{i=1}^{M} A_i . \tag{2.15}$$

In the case of the ensemble average of an arbitrary property, A,

$$\langle A \rangle_{Ensemble} = \int_p \int_r A(p,r)\rho(p,r)dpdr, \tag{2.16}$$

where r is representative of position vectors, p is linear momentum, and ρ is the probability density function. Primarily, ensemble averaging is employed for assessments where conditions are in equilibrium as the probability density function is known; in the case of non-equilibrium situations time averaging is typically employed as ρ is unknown. However, in accordance with the Ergodic hypothesis, $\langle A \rangle_{Time} = \langle A \rangle_{Ensemble}$ when the process is in steady-state [66]. Therefore, as this thesis primarily evaluates non-equilibrium simulation conditions to investigate the final steady-state behaviors of complex systems, time averaging is used to statistically sample results.

Within MD simulations, the type of ensemble can be prescribed based on specific investigational needs and include various thermostating and/or barostating techniques. Although many more exist, the microcanonical (*NVE*), canonical (*NVT*), and isothermal-isobaric (*NPT*) ensembles are primarily employed in this thesis. In the *NVE* ensemble, the number of particles, simulation domain volume, and energy are held constant throughout the implementation of MD algorithm methods to effectively measure changes in a systems total energy. In cases where temperature and pressure are required to be kept constant, the *NVT* (constant number of particles, volume, and temperature) and *NPT* (constant number of particles, pressure, and temperature) ensembles can be utilized. However, vital to most MD investigations is the monitoring and collecting of changes in system-wide total energy. As the sum of kinetic and potential energy, kinetic energy is obtained by rewriting and solving Eq. (2.15) as:

$$KE(t) = \frac{1}{2}\sum_i m_i (v_i(t))^2, \tag{2.17}$$

where m_i and v_i are the respective mass and velocity of particle i, and t is the timestep iteration. Employing kinetic energy calculations and the total potential energy from the potential energy function, total energy can be determined for further data processing. Moreover, when considerations of constant temperature, pressure, etc. are required, these will also be taken into account within ensemble calculations.

2.5 Modelling of Graphene – Water Systems

The methods presented within this section seek to describe the various modeling features of simulated graphene – water systems by detailing construction of initial structural geometries and presenting the parameters used to simulate graphene and water behaviors in a realistic manner. This section is complimented by the earlier discussions of interatomic potentials, and the implementation of LAMMPS (see Appendix). Moreover, since each investigation (Chapters 4, 5, and 6) requires unique simulation constraints, specified parameters will be given for each case.

2.5.1 Water: Structure and Modelling

In constructing initial geometries with many thousands of water (H_2O) molecules, the open source software Packmol [67] is employed fill a specified dimensional volume with water corresponding to a chosen density. To do this, a .pdb file is created to detail the coordinates of a single water molecule; included in the file are the positions of hydrogen and two oxygen atoms that form the tetrahedral shape of water, corresponding to their specific O-H bond length of 0.96 Å and observed H-O-H angle of 104.52° (some water models employ the ideal tetrahedral angle

of 109.47° rather than the observe value; LAMMPS corrects these angles based on input parameterization). Packmol then processes this file to replicate the single water molecule (Fig. 2.2a) and fills the selected volume with a specified density of water molecules (Fig. 2.2b); for the purposes of this thesis, geometries are filled with water at a density of ρ = 1000 kg/m^3 (note: this is the density of only that specific water volume, not the entire simulation cell volume).

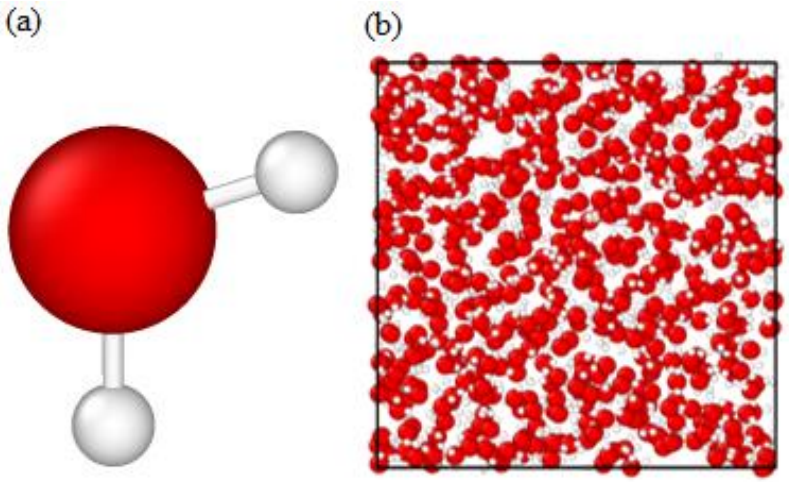


Figure 2.2. (a) Simulated water molecule, and (b) a box of water molecules; the black line defines the periodic boundary of the simulation cell.

In simulating the constructed water molecules, many different pair potential models exist to describe water behavior, with each having a particular characterizing ability for specific areas of interest. Generally speaking, there is no one go-to water model that can accurately represent all behavioral facets of water due to the shear complexity of water mannerisms across multiple phases and corresponding thermodynamic properties therein. However, researchers have developed numerous models, such as the SPC/E [68], TIP3P [55], TIP4P [55], TIP4P/2005 [69], TIP4P/Ice [70], etc., water models, to recreate desired behavioral aspects of water (e.g., density, viscosity, conductivity, water phase diagram, and other thermodynamic properties). As such, these models range in complexity and vary based on the number of interaction point sites, rigidity or flexibility, and polarization effects.

Water models can be classified based on the number of interaction sites; this can range from 2-site to 6-site models, with 3-site and 4-site being the most common and employed in this thesis (i.e., SPC/E and TIP4P-iteration water models) due to their computational affordability and replication accuracies. Within a simulated water model, each site has a point charge and corresponds to an interaction point at each atom in a water molecule. As the name implies, the 3-site model has three different interaction sites at the location of the O and two H atoms. However, in 4-site (or more) models, “dummy” atoms with a negative charge are added near the oxygen atom so to improve electrostatic distribution around the water molecule. These models can either be kept rigid or allowed to be flexible. The common choice is make water molecules reliant upon non-bonded interactions by specifying rigid molecular bonds between the O and H atoms; this method is widely selected as it increases computational efficiency. In some cases, however, allowing bonds to be flexible (i.e., anharmonic O-H bond stretching) has shown to more accurately describe some water properties [71], but at the expensive of computational efficiency; thus, only rigid models are utilized [72].

Table 2.2. Parameter values defining tested water model properties from Refs. [55, 68, 69].

H_2O Interaction Parameter	SPC/E	TIP4P	TIP4P/2005
Type	3-Site	4-Site	4-Site
q_o (e_c)	-0.8476	-1.040	-1.1128
q_H (e_c)	0.4238	0.520	0.5564
$r_{o\text{-}M}$ (nm)	---	0.15	0.1546
$r_{o\text{-}H}$ (nm)	1.0	0.9572	0.9572
$\theta_{H\text{-}o\text{-}H}$ (°)	109.47	104.52	104.52
$\varepsilon_{o\text{-}o}$ (kJ/mol)	0.6497	0.6485	0.7748
$\sigma_{o\text{-}o}$ (nm)	0.3166	0.31536	0.31589

For the purposes of this thesis, polarized water models are not included within this study as non-polarizable models are found to effectively describe water behavior [70, 73]. Thus, the non-polarized SPC/E, TIP4P, and TIP4P/2005 water models are employed in this thesis' investigations. Included in each model are long-range electrostatic interactions and dispersion forces using Coulomb's law and the Lennard-Jones potential, respectively. Outside of varying by charge site, these models primarily differ in LJ ε and σ value, and O and H charge; detailed parameters for each water model are listed in Table 2.2. Inter- and intra- molecular interactions of all three models are simulated via the pair potential description from Section 2.2, and are represented by combining Eqs. (2.4) and (2.5) as:

$$U_{LJ}(r_{ij}) = 4\varepsilon_{ij}\left[\left(\frac{\sigma_{ij}}{r_{ij}}\right)^{12} - \left(\frac{\sigma_{ij}}{r_{ij}}\right)^{6}\right] + \sum_{i<j}\frac{q_i q_j}{4\pi\varepsilon_0 r_{ij}}. \tag{2.18}$$

2.5.2 Graphene: Structure and Modelling

Graphene's structure consists of a single layer of carbon atoms in a hexagonal "honeycomb" lattice structure (Fig. 2.3a). Each of the six atoms that form a hexagonal ring is separated by an intralayer carbon spacing (or bond length) of 1.41 Å [74]; additionally, as this thesis investigates systems composed of single- and multi-layer graphene, a distance of 3.35 Å [75] is specified as the interlayer spacing between multiple graphene sheets (Fig. 2.3b).

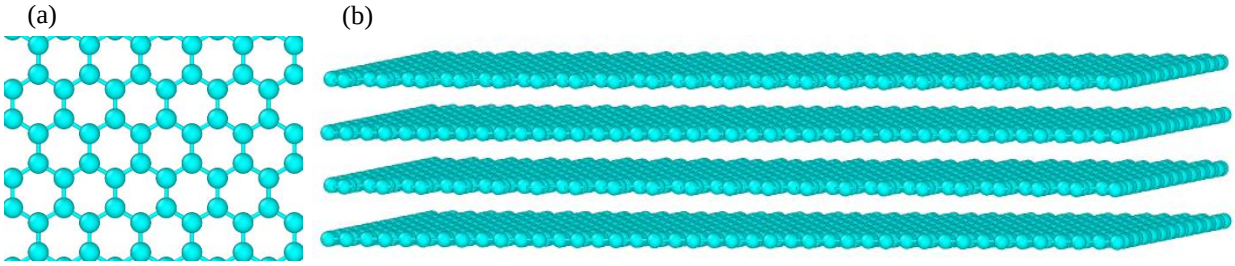


Figure 2.3. (a) Magnified image of graphene's honeycomb structure, and (b) multiple graphene layers.

Employing the physical details of graphene's structure, initial geometries are built with the aid of the open source software Visual Molecular Dynamics (VMD) [76] and its "Nanotube Builder" function. VMD allows for specification of graphene size, edge configuration (armchair or zigzag), and number of layers; once created, atomic coordinates can then be exported as many different file formats (.xyz, .lammpstrj, .pdb, .js, etc.). These various formats allow for simulation, visualization, and/or additional modification; namely, the .pdb file is used for further processing

to complete fabrication of graphene – water systems (later discussed). Additionally, as each simulation calls for particular initial geometries, further details for each investigation regarding their specific dimensions and configurations will be provided.

As earlier detailed, graphene is modeled by the 2nd generation Tersoff-Brenner (REBO) bond-order potential to effectively characterize carbon atoms constrained by strongly covalent sp^2 C-C bonds. In this description, while also considering C-C bond length, intralayer carbon behavior is defined by the LJ and other parameters in the previously presented Table 2.1. Moreover, interlayer C-C interactions between multiple layers of graphene are modeled by the 12-6 LJ pair potential parameters [Eq. (2.4)] obtained from Ref. [77]; no charge is associated with interlayer graphene interactions.

It must be noted that the only commonality among simulated graphene structures is the use of the armchair edge configuration; this was selected by default as there is no difference between the two configurations when graphene is periodically modeled as an infinite sheet. Moreover, while graphene can be twisted, rolled, and manipulated to form three-dimensional nanotubes, nanostructures, etc., only flat 2D graphene structures are employed for use within the scope of this thesis.

2.5.3 Graphene – Water Systems: Structure and Modelling

Once the processes for constructing individual graphene and water structures is known, fabrication of integrated systems only requires a few more simple procedures. The .pdb files for both graphene, obtained from VMD's nanotube builder function, and water (single water molecule) are then combined through processing with Packmol. Three-dimensional (3D) coordinates of graphene sheet(s) position, in addition to desired water block dimensions and coordinates are speficied in the Packmol input script and then submitted for processing. Packmol outputs a new .pdb file of the combined structures with their corresponding positions; this file is then uploaded to VMD, and employing VMD's Tk Console, a LAMMPS readable data file is then produced that specifies atom/molecule coordinates and definitions as well as angle and bond definitions. This acts as the data file of initial atom configurations employed in LAMMPS simulations; further details will be provided in the Appendices.

Modeling interactions between dissimilar media can be a difficult task. Many studies have sought to parameterize graphene – water interactions by means of mimicking experimental graphene wettability (characterized by the wetting contact angle, WCA, and is discussed later in Chapter 3) results, in addition to analyzing fundamental assessments employing MD and DFT simulations. The main focus of these studies were to precisely characterize C-O and C-H interaction strength, distance, and cutoff radius for LJ term (ε_{ij}, σ_{ij}, and r_c) definition, so to accurately describe graphene – water interactions within MD simulations. From these past investigations, although the terms of $\sigma_{\text{c-o}}$ and r_c were shown to have some influence, it was determined that the interaction strength ($\varepsilon_{\text{c-o}}$) between graphene and water was the primary mechanism inducing wetting appearances, as illustrated by resulting atom configurations. Furthermore, studies found that while inclusion of C-H characterization can indeed have some effect on carbon – water relations, interactions of this type are usually deemed negligible due to their weak influence and thus, neglected from parameterization [78]. Therefore, for the purposes of this thesis, all graphene – water interactions are accounted for by the 12-6 LJ potential [Eq. (2.4)], where only the interactions between graphene carbon atoms and oxygen atoms of a water molecule are defined with no associated electrostatic description.

Employed by many studies in the past, this method of modeling C-O interactions via dispersion (or van der Waals) forces is primarily utilized as an effort to increase computational efficiency and thus, is employed within the scope of this thesis. Characterizing LJ parameter values for surface – water interactions are specified in Table 2.3; moreover, the cutoff value for all (no matter the atom type, material, etc.) LJ interactions is specified as r_c = 10 Å. Detailed simulation techniques employing MD algorithms and structural characterizations will be further described in Chapters 3, 4, and 5; commands used for LAMMPS implementation are detailed in the Appendices.

Table 2.3. Parameter values characterizing graphene – water interaction strength and distance.

	Case 1	Case 2	Case 3	Case 4	Case 5	Case 6	Case 7	Case 8
$\varepsilon_{c\text{-}o}$ (kJ/mol)	0.1869	0.2834	0.3920	0.4763	0.5728	0.6693	0.7748	1.00553
$\sigma_{c\text{-}o}$ (nm)	0.319	0.319	0.319	0.319	0.319	0.319	0.319	0.319

CHAPTER THREE

SURFACE INTERACTIONS AND MOMENTUM TRANSPORT

3.1 Introduction

As the first iterative step in this thesis' pursuit of unraveling momentum transport characteristics in nanoscale environments, fundamental graphene – water surface interactions are examined by means of assessing surface wettability. Understandings of wettability are then applied to the study of a Poiseuille flow of liquid water inside nanochannels to evaluate nanoscale flowing water behavior and viscosity. The topics presented in this chapter acts as building blocks that form a basis for fundamental momentum analysis; each topic is significantly crucial understanding the role of momentum transport within the overarching study of convective heat transfer with nanoscale graphene – water systems.

3.2 Surface Interactions and Wettability

3.2.1 Introduction to Wettability

A surface's ability to either attract or repel water is known as its wettability, and is defined by the its resulting wetting contact angle (WCA). Classified as either hydrophobic (> 90°) or hydrophilic (< 90°), surface wettability seeks to describe a material's properties for functional application to diverse areas such as waterproofing [79], fluid transportation [80], thermal management [81, 82], and many others [83-87]. The evaluation of a material's wetting properties is not a new task within research; many experimental and numerical (MD) studies have been conducted to evaluate the observable WCA on a wide range of materials and substrates (e.g., Si, glass, gold, silver, etc.). In addition, more recent studies have been performed to evaluate and effectively detail graphene wettability properties for effective applicational purposes. However, experimentalists have faced many challenges in isolating a single layer (or even multiple layers) of pure graphene to conclusively investigate graphene wettability (WCA ranging from approximately 85° to 100° [36, 44, 45], however new studies [88-90] suggest it could be as low as 64° for water on an anatomically pure graphene sheet).

Through numerical efforts utilizing DFT and MD simulations, researchers both aided in narrowing down the precise WCA value for a graphitic surface (roughly 90°), and developing potential models for replicating the range of experimentally determined WCA from literature. Therefore, understanding nanoscale wetting traits and behaviors becomes a necessity within nanoscale environments of interacting materials and fluids. In this study, the WCA is determined from the resulting configuration of MD simulated atoms; surface interaction strength will be studied by evaluating the interatomic potential between water molecules and constituent 2D-material atoms (representing the force field). Simulations are primarily conducted to assessed the effects of varying levels of graphene – water interaction strength ($\varepsilon_{c\text{-}o}$) for understanding within future investigations. Tuning this LJ $\varepsilon_{c\text{-}o}$ parameter allows for manipulation of resulting surface interactions as measured by the WCA; by increasing this value, the graphene wall is inferred to produce more hydrophobic tendencies, while decreasing this value is thought to yield more hydrophilic characteristics. Therefore, to understand graphene – water surface interactions, differing values of $\varepsilon_{c\text{-}o}$ are selected and range from 0.1869 kJ/mol to 1.0553 kJ/mol as presented in

the earlier Table 2.3. Although varying number of water molecules and graphene layers are also investigated, this however is not of primary focus.

3.2.2 Wettability Setup and Simulation Details

Two graphene layers are employed for assessment and are the supporting substrate on which the liquid water molecules will be placed and interact (Fig. 3.1); graphene sheet dimensions are set as 11.0×11.0 nm^2 in the *x*- and *y*- axis directions and correspond to 4680 carbon atoms in each graphene sheet. Moreover, previous studies vary in form by either keeping graphene sheets as a rigid slab or allowing them fluctuate normally; for increased data accuracy and more realistic graphene – water behaviors, this investigation allows the graphene sheets to fluctuate in a normal manner; this is done by holding in place the outer-most graphene layer (or base layer) at its original position using a weak harmonic spring constant; coupled with interlayer C-C interactions, this base sheet then acts as an anchor and to the above graphene layers, thus allowing them to behave in a realistic manner while remaining in their originally specified positions. A block of 1839 liquid water molecules (ρ = 1000 kg/m^3) is then placed above (*z*-axis direction) these graphene layers; the water block volume is 5.0×5.0×2.2 nm^3. PBCs are applied in all three dimensions; the *z*-axis dimension is extended to 8.0 nm to allow for droplet formation at high hydrophobicities, and negate potential cross-periodic image interactions along the *z* direction.

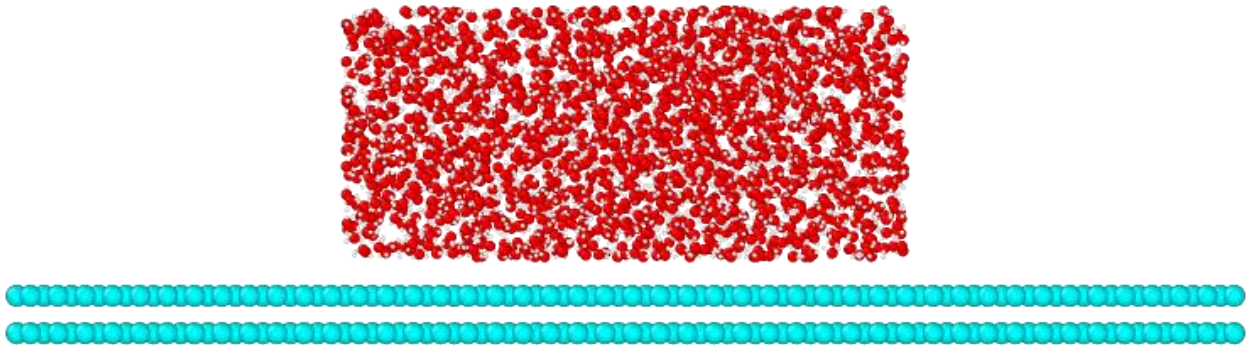


Figure 3.1. Initial setup for WCA assessment showing 1839 water molecules above a two-layer graphene substrate.

In all wettability simulations, only the TIP4P/2005 water model is employed to describe water behavior. The 12-6 LJ potential parameters characterizing graphene – water interactions are summarized Table 2.3, where the LJ $\varepsilon_{c\text{-}o}$ is varied to assess differing levels of interaction strengths and their resulting WCA values. The interaction distance at which potential energy is zero is set as $\sigma_{c\text{-}o}$ = 3.19 Å for all simulations.

Each simulation requires a total run time of 2.0 ns with a 2.0 fs time step and is separated into two phases. The system is first equilibrated in the *NVT* ensemble for 0.5 ns at *T* = 300.0 K. After which, the system is then placed in the *NVE* ensemble with thermostated removed; this is implemented so to ensure that data collection is not distorted by thermostating techniques. Data is then collected by sampling atom trajectories every 0.1 ns.

3.2.3 WCA Methodology

WCA (θ_c) measurements for each surface condition are extracted by analyzing the resulting configuration of water molecules on the graphene surface via the methods of Refs. [91, 92]. First,

the water droplet boundary outline is found by determining the center-of-mass its resulting water density profile. With the interface location known, a tangent line is then fit to the solid – liquid interface; the angle is then measured as the angle made by the tangent at the surface-water interface as in Fig. 3.2, with θ_c is calculated as:

$$\theta_c = \frac{x_c - x_0}{z_c - z_0}, \tag{3.1}$$

where (x_c, z_c) is the fitted circle centroid with a radius of r, z_0 is the cutoff distance above the substrate, and x_o is the radius of the boundary data [= $x_c - (r^2 - |z_0 - z_c|^2)^{1/2}$].

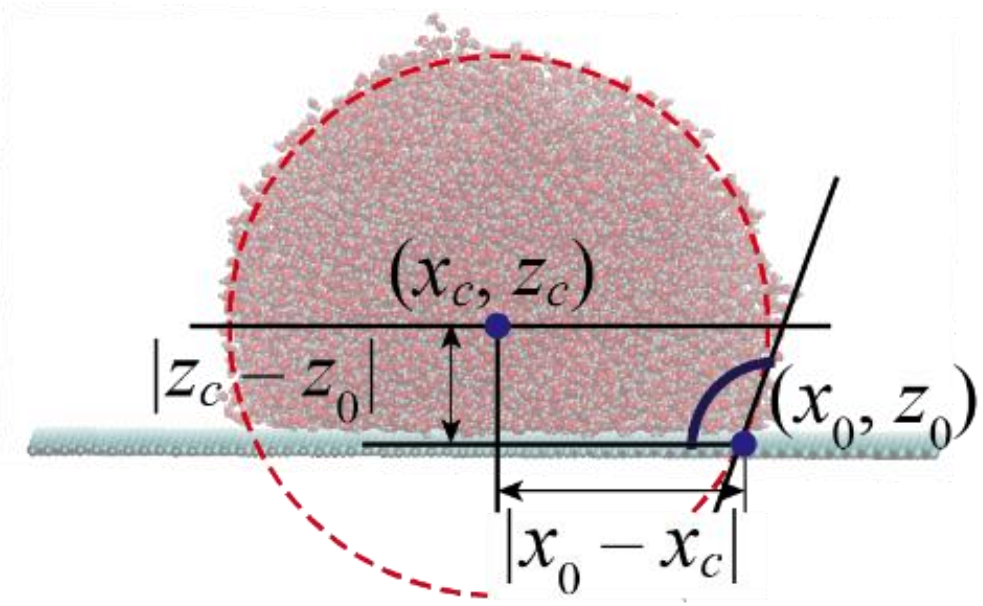


Figure 3.2. Sample illustration of fitting a tangent line to determine the resulting WCA.

3.2.4 Wettability Analysis and Deductions

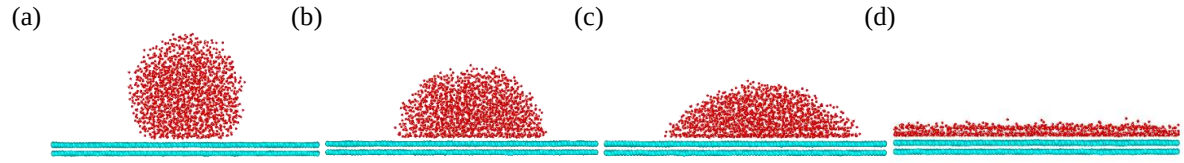


Figure 3.3. Final water droplet configurations for: (a) $\varepsilon_{c\text{-}o}$ = 0.2834 kJ/mol (θ_c = 114°), (b) $\varepsilon_{c\text{-}o}$ = 0.4763 kJ/mol (θ_c = 68°), (c) $\varepsilon_{c\text{-}o}$ = 0.5728 kJ/mol (θ_c = 42°), and (d) $\varepsilon_{c\text{-}o}$ = 1.0553 kJ/mol (θ_c = 0°).

From its initial structure (Fig. 3.1), the system is allowed to relax over the simulation duration until the water droplet reaches its steady-state configuration on top of the graphene base. At very low $\varepsilon_{c\text{-}o}$ values, water is seemingly repelled by the graphene sheet; in these instances, the inter-molecular interactions between the water molecules and the graphene sheet are not overcome by their attraction to one another (expressed by the $\varepsilon_{c\text{-}o}$ term). However, as shown in the snapshots of Fig. 3.3, increasing this term gives way to greater graphene – water affinities that yield receding

contact angles; Fig. 3.4 better illustrates the drastic changes in wetting behavior attributed to the manipulation of graphene – water interaction strength.

Consistent with previous reports, this is further characterized by the almost linear relationship between $\varepsilon_{c\text{-}o}$ and resultant WCA value in Fig. 3.4. Additionally, respective WCA values for $\varepsilon_{c\text{-}o}$ = 0.3920 kJ/mol and $\varepsilon_{c\text{-}o}$ = 0.4762 kJ/mol are found to be 91° and 68°, which are in similar agreement with previous determinations [36, 89, 90]. Moreover, past the value of $\varepsilon_{c\text{-}o}$ = 0.7748 kJ/mol, complete wetting is observed as WCA values yield an angle of 0°. At larger $\varepsilon_{c\text{-}o}$ values, the interaction energy is insufficient to surpass the inter-molecular attractions within the separate interactions between water molecules and intra-layer graphene sheet carbon atoms. As this value is increased, atomic affinities within each media are overcome to produce increasing attraction and thus, decreasing WCA values. This study is utilized for understanding slip flow and heat transfer behaviors and mechanics in subsequent sections and chapters.

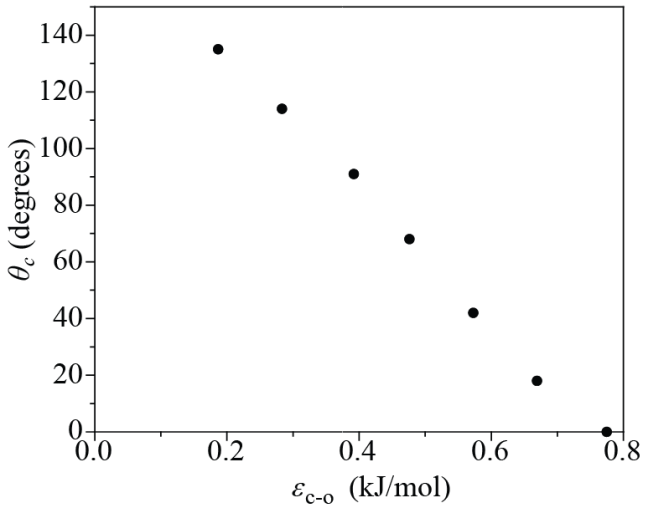


Figure 3.4. WCA decrease with carbon – oxygen interaction strength; not shown is the value for $\varepsilon_{c\text{-}o}$ =1.0553 kJ/mol, which is θ_c = 0°.

3.3 Poiseuille Flow and Viscosity

In conjunction with understandings of surface interactions obtained from wettability analysis in the previous Section, this study seeks to provide insight into the mechanisms of momentum transport at the nanoscale level. To evaluate nanoscale momentum transfer, a Poiseuille flow of liquid water inside nanochannels is employed as a two-pronged investigation to assess flowing water behavior and viscosity. Moreover, this study of momentum transfer is highly important to later chapters as understanding flow behavior and employed water model viscosity replication are critical to the ultimate study of nanoscale convection heat transfer.

3.3.1 Introduction to Poiseuille Flow and Viscosity

Key to momentum transport analysis of solid and liquid media in contact is that of the fluids density and viscosity, as these intrinsic properties are highly influential on the resulting flow behavior. Viscosity (μ, Pa-s), defined as a ratio of shear stress to a velocity gradient in a fluid, represents a fluids internal resistance (or friction) to the transfer of momentum to adjunct fluid layers (or its surroundings), and is critical in understanding nanoscale fluid flow. To assess

momentum transport in MD, fluid flow can be generated by either a wall-driven Couette flow to shear the liquid or a pressure/force -driven Poiseuille flow, and assessed via post-processing velocity profiles and other recorded data, with each type of flow having its own advantages and drawbacks. For the purposes of this research, investigation of Poiseuille flow was selected for its less-demanding translational ability to future heat transfer assessments than of that offered by Couette flow. However, no matter the type of induced flow, fluid flow behaviors are shown to deviate from macroscale theory with the appearance of liquid slip flow as dimensional scales decrease [49].

We begin this section with investigating a Poiseuille flow of liquid water flow in graphene nanochannels to characterize flow behavior and the appearance of slip for later chapters. As slip is found to arise in cases of flowing water interaction with graphene, we detail our methods employed to circumvent these issues to determine the viscosities of various water models over a range of temperatures.

3.3.2 Details and Analysis of Water Flow in Graphene Nanochannels

Graphene nanochannels are composed of two parallel walls fixed into position at 5.0 nm apart along the *z*-axis direction; this distance is specifically chosen account for liquid layering effects as augmented fluid behaviors arise in very narrow channels [93]. Walls are modeled with the REBO potential, and the length and width of the channel are 3.0 nm in both the *x*- and *y*- axis directions. Each wall is comprised of two graphene sheets (or double-layer graphene, DLG) consisting of 832 carbon atoms, with intralayer C-C interactions modeled by the parameters of Ref. [77]. A 3.0×3.0×5.0 nm^3 block of 1848 liquid water molecules (ρ = 1000.0 kg/m^3) is placed in-between the DLG walls with Fig. 3.5 illustrating this systems setup; for the purposes of this investigation, only the TIP4P/2005 water model is employed. To assess differing levels of surface effects, the interaction strength between graphene and water varies by the range of LJ $\varepsilon_{C\text{-}O}$ values in Table 2.3.

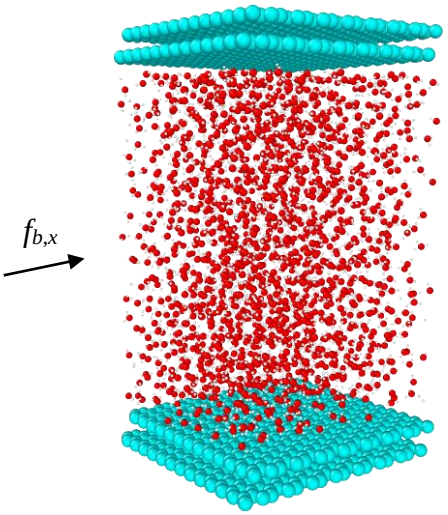


Figure 3.5. Setup of water flow in between two parallel graphene plates; flow is generated by adding a body force, $f_{b,x}$, to each water molecule.

Non-equilibrium molecular dynamics (NEMD) simulations are performed for a total duration of 2.0 ns using a 1.0 fs timestep. An initial equilibration phase is conducted for 0.5 ns.

Once equilibration is complete, further simulation is implemented for 1.5 ns in the *NVT* ensemble; here, the system temperature is controlled by Nose-Hoover [11, 12] thermostating methods at a temperature of T = 300 K. In this NEMD simulation phase, Poiseuille flow is generated by applying a flow-driving body force, $f_{b,x} = 1.38\times10^{-13}$ N/molecule (corresponding to a velocity of 20 m/s for the $\varepsilon_{c\text{-}o}$ value of water on an uncontaminated graphitic surface), in the x-axis direction to each liquid water molecule. With PBCs applied in the x- (flow direction) and y- axis directions, and fixed in the z-axis with the 2D slab method, the body force will cause the flowing water molecules to exit one side of the periodic box and re-enter from the opposite side of the periodic image. As the system evolves, a velocity profile of the liquid water molecules will begin to emerge; velocity and density data are frequently recorded into equally spaced bins distributed across the z-axis.

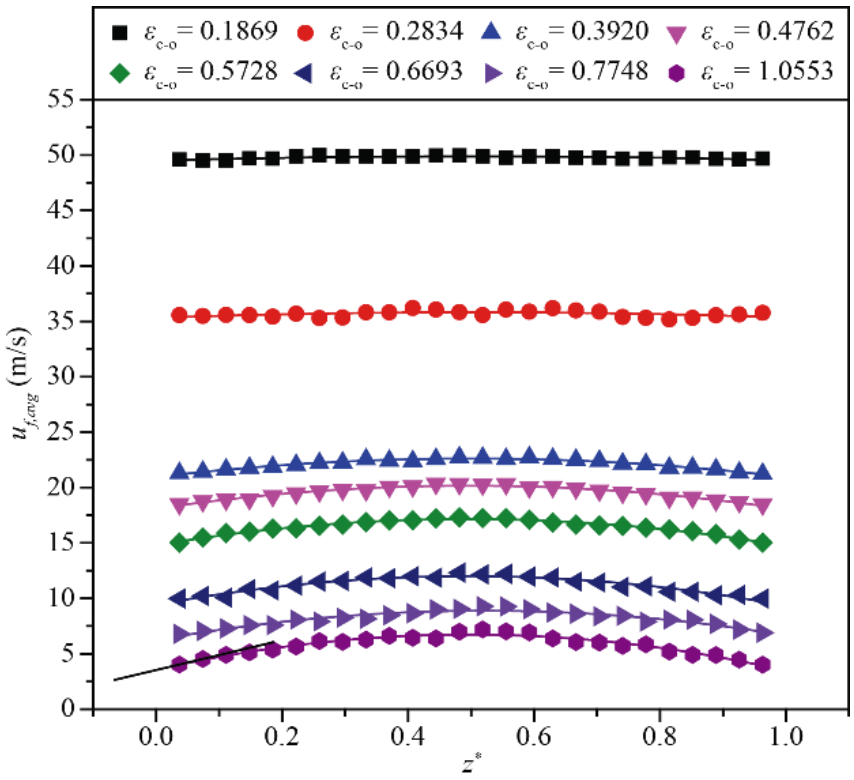


Figure 3.6. Velocity profiles with parabolic fitting for water flow with different LJ $\varepsilon_{c\text{-}o}$ values.

In analyzing water flow behavior, as depicted by the resulting velocities profiles in Fig. 3.6, it is apparent that slip is a prevalent factor across the entire range of interaction strengths. To quantify the magnitude of slip in NEMD Poiseuille flow for each case, the slip length, l_s, is determined by:

$$u_s = l_s \left.\frac{\partial u_x}{\partial z}\right|_{z=0}, \tag{3.2}$$

where u_s is the water velocity at the surface (or wall interface) and $\partial u_x/\partial z$ is the velocity gradient in the liquid at the wall. In concurrence with previous reports [94] and as detailed in this student's recently published study [95], flowing water interaction with atomically smooth graphene-walled nanochannels is found to induce large magnitudes of slippage, even at increasing interaction

strengths that yield extremely hydrophilic (WCA = 0°) surface conditions (Fig. 3.7); this is further summarized in the later Chapter 5.

Moreover, as the aim of this Section is to not only study flowing water behavior, but to also determine water viscosity. In the case of Poiseuille flow, viscosity is given by:

$$\frac{d}{dz}\left(\mu\frac{du_x}{dz}\right)=-\rho f_{b,x}, \tag{3.3}$$

where ρ is the liquid water density. As viscosity determinations are reliant upon the velocity gradient in the fluid, the presence of hydrodynamic slippage at the graphene – water interface is indicated to be a very significant inhibitor to evaluations when post-processing resultant velocity data; consequently, a no-slip environment is required for precise evaluations of viscosity calculations.

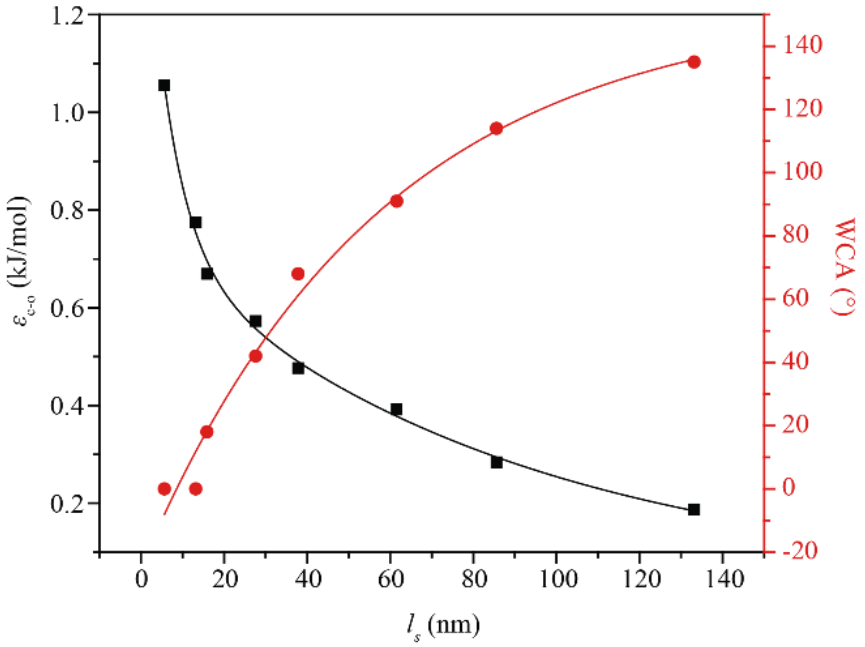


Figure 3.7. Resulting hydrodynamic slip lengths at the range of interaction strengths (black squares), and their corresponding WCA values (red circles). To better guide the eye and identify trend behavior, curve fitting is applied to slip length relations.

3.3.3 Setup and Evaluation of Water Viscosity in MD

Increased research into liquid water interactions at the nano-scale level has led to an emphasis on the need to accurately replicate water's viscosity within MD simulations and ultimately, the development of many different water models with varying behaviors. As the water models presented in Chapter 2 vary in charge site number, LJ potential parameters, and charge value (see Table 2.2), it is imperative to pin-point the best suited water model for any given simulation requirements. Viscosity can be determined through various avenues within MD simulations. Some previous investigations into viscosity using the Green-Kubo [96, 97] and Stokes-Einstein [98] methods utilizing an autocorrelation function of the stress tensor have been reported, however these techniques require extensive computational resources. Employing a similar methodology as Section 3.3.2, a Poiseuille flow of liquid water through a nanochannel is

generated and resulting velocity profiles assessed; the viscosity of the SPC/E, TIP4P, and TIP4P/2005 water models various water models at the temperatures of T = 280, 300, 320, 340, and 360 K is then determined. It is from this assessment on which we base our selection of water model for the study of thermal transport.

To properly assess water properties and circumvent issues of slip within viscosity calculations, we modify our investigation with the methodology of Markesteijn et al. [32] and that of a previous report that studied the viscosity of liquid argon [99]. In these modifications, the simulation setup/methods and data recording techniques detailed in the previous section are held constant (e.g., channel dimensions, number of water molecules, etc.), however the anatomically smooth graphene walls are replaced by topographically rough 3D walls, modeled as silicon, fixed into position. Each Si wall consists of 576 atoms and interacts with oxygen atoms with the LJ values obtained from Lorentz Berthelot mixing rules of $\varepsilon_{Si\text{-}o}$ = 2.787 kJ/mol and $\sigma_{Si\text{-}o}$ = 0.324 nm [100].

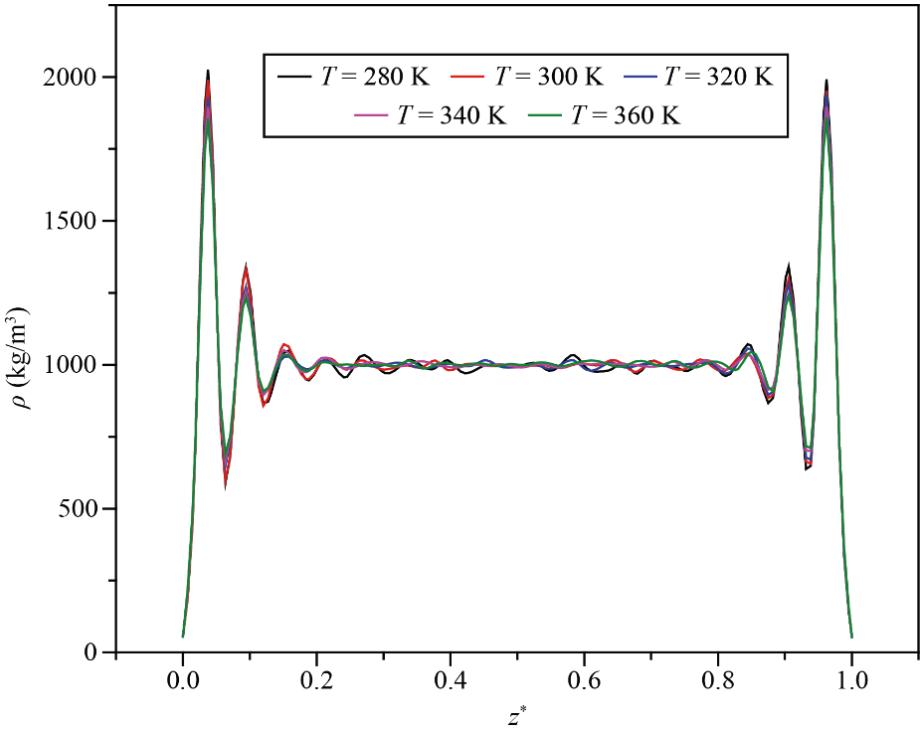


Figure 3.8. Water densities across the channel for the range of temperatures using the TIP4P/2005 water model.

Density across the channel must be considered in viscosity calculations, particularly at nanoscale dimensions, due to the influence of solid – liquid interactions on liquid layering near the walls. These effects decrease in influence when sufficiently far away from the walls; as depicted in Fig. 3.8, density fluctuations are seen near the walls in which the water molecules congregate due to the Lennard-Jones interactions between the wall and oxygen atoms. The bulk density is seen in the middle of the nanochannel, away from the walls at a distance of approximately 0.12 nm (or roughly 10 molecular diameters); in this region is where continuum conditions are found. Bulk densities for all water models and at various temperatures are a constant ρ = 1000.0 kg/m^3 due to a constant volume, however, temperature differences are shown to produce an effect on liquid layering densities at the wall. As illustrated by Fig. 3.8, densities for the TIP4P/2005 water

model are seen to decrease at the wall as temperatures increase, indicating the influence of liquid laying density of viscosity. At the continuum distance (0.12 nm), and utilizing the obtained density and velocity profiles for the differing cases of varying interaction strengths, velocity profiles can be approximated with quadratic fitting to determine viscosity by rewriting Eq. (3.3) as:

$$\mu = \frac{-\rho f_x}{d^2 u_x / dz^2}, \tag{3.4}$$

where d^2u_x/dz^2 is the second derivative of the velocity profile fit with respect to the channel height. At the same amount of applied force, maximum velocities vary at the range of temperatures; this is attributed to decreased density at the wall due to higher temperatures allowing for increased velocities inside the channel. The resulting velocity profile and quadratic fitting line for the TIP4P/2005 water model at T = 300 K is shown in Fig. 3.9.

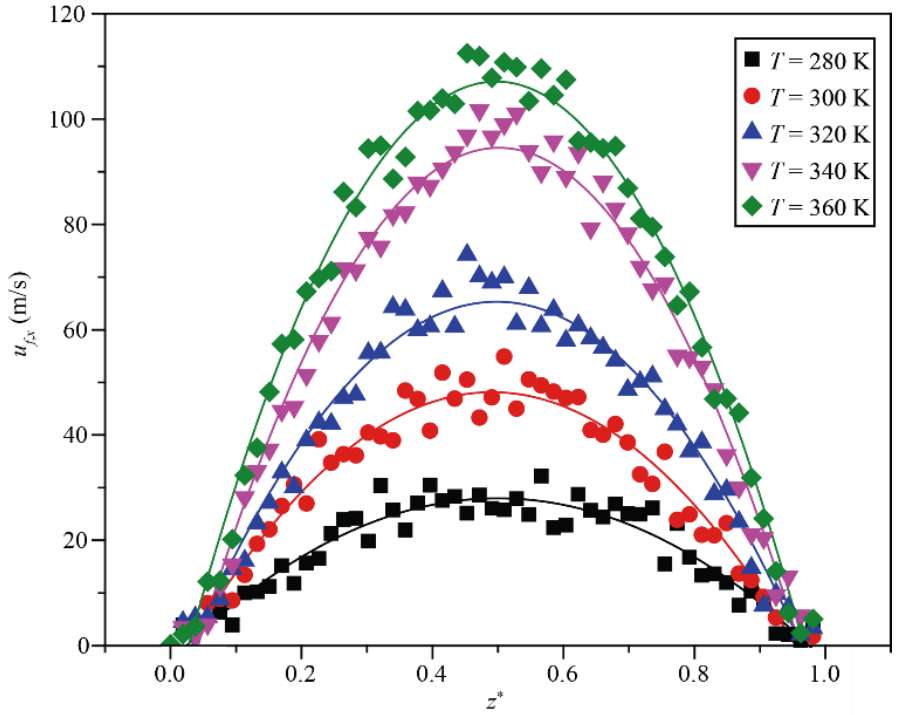


Figure 3.9. Velocity profiles of the TIP4P/2005 water model at the range of temperatures; quadratic fit lines employed for viscosity calculations are show to better guide the eye.

The previous MD study of various viscosity values by Markestijn et al. [32] compared their found values with that of experimental data [101]; they found that the TIP4P displayed the most amount of error in recreating water viscosity, while the SPC/E water produced a moderate error and the TIP4P/2005 yielding the least error as compared to experimental viscosity values. As the purpose for this assessment is to evaluate viscosity at temperatures of T = 280, 300, 320, 340, and 360 K, and due to the lack of experimental viscosity data at these exact temperatures, experimental values are interpolated to provide approximate viscosity values at these exact temperatures.

In analyzing resultant viscosity values of the various tested water models and their relation to temperature, it is revealed that the TIP4P/2005 water model recreates a viscosity of μ = 0.892 mPa-s at T = 300 K, which is within an error of 5.4% of interpolated experimental value at the same temperature. At the same temperature (T = 300 K), the SPC/E and TIP4P water models

recreated water viscosities of μ = 0.756 mPa-s and μ = 0.486 mPa-s, respectively. The SPC/E water model gives a reasonable error of roughly 19.86%, however the TIP4P model displays a large deviation from experimental data with underestimation of 48.48%. Thus, for the investigated water models over a range of temperatures, the TIP4P/2005 model is shown to more accurately follow experimental viscosity data, as illustrated in Fig. 3.10.

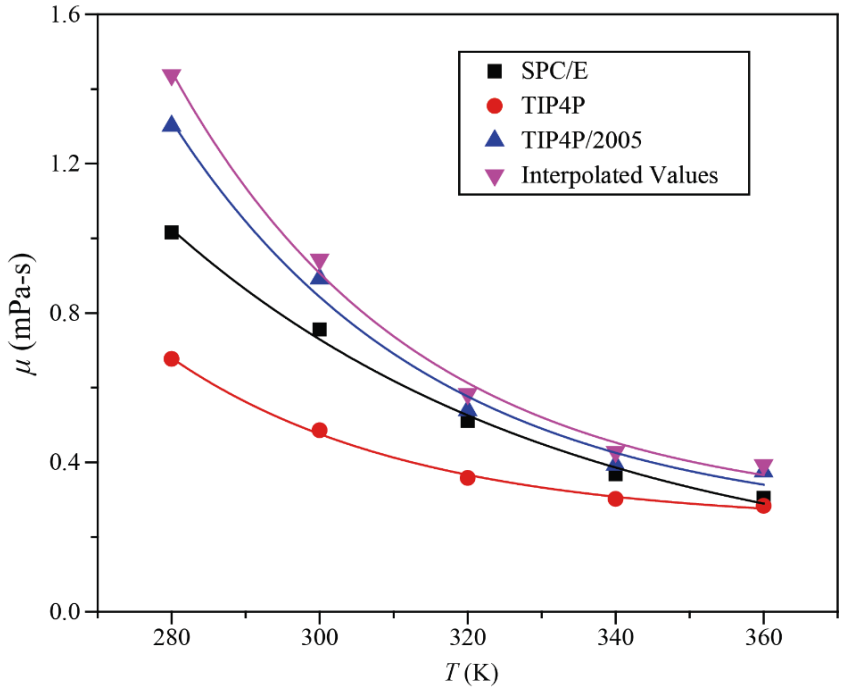


Figure 3.10. Viscosity values as a function of temperature as compared to the interpolated experimental viscosity values; curve fit lines are added to better identify viscosity changes with temperature for each water model.

Moreover, this thesis finds that the TIP4P water model exhibits the most amount of error ranging from 27% to 53%, while SPC/E water produced moderate error of roughly 12% to 29%; the TIP4P/2005 water model was shown to yield the least amount with an error of only 4% to 9%. These error ranges are found to be consistent with Ref. [32] and are shown in Table 3.1.

Table 3.1. Dynamic viscosities for the SPC/E, TIP4P, and TIP4P/2005 water models over a range of temperatures. Error is calculated by $(\mu-\mu_{ext})/\mu_{ext}$.

	SPC/E		TIP4P		TIP4P/2005		Interpolation
T (K)	μ (mPa-s)	Error (%)	μ (mPa-s)	Error (%)	μ (mPa-s)	Error (%)	μ_{ext} (mPa-s)
280	1.016	-29.32	0.677	-52.90	1.301	-9.49	1.437
300	0.756	-19.86	0.486	-48.48	0.892	-5.44	0.943
320	0.511	-12.36	0.358	-38.60	0.539	-7.56	0.583
340	0.368	-14.13	0.302	-29.53	0.393	-8.30	0.428
360	0.304	-22.45	0.283	-27.92	0.375	-4.62	0.393

3.3.4 Viscosity Conclusion

The SPC/E, TIP4P, and TIP4P/2005 water molecules are investigated via MD simulations to determine which model is best suited for recreating experimental viscosity values at the temperatures of T = 280, 300, 320, 340, and 360 K. The resultant water velocity gradient at the

wall is obtained from MD outputted velocities profiles; using this data along with the determined water density inside the nanochannel, and the known values of nanochannel height and flow-driving body force, viscosity values for these three water models are determined. Calculated values are compared to interpolated experimental results. Although we note that interpolation can influence exact percent error determinations, it is found that the TIP4P model greatly underestimates viscosity values, while the SPC/E model performs adequately in the recreation of viscosity behavior over the range of employed temperatures. As the TIP4P/2005 water model is found to produce the most realistic recreation of water behavior to obtain accurate viscosity values at the range of investigated temperatures; therefore, this model is recommended for use in MD simulations investigating momentum transport within liquid water flow.

3.4 Surface Interactions and Momentum Transport Conclusion

In this chapter, surface interactions were found to be highly influential to the resulting configuration of water molecules on a graphene substrate as represented by the WCA. Application of wettability assessments to analysis of water flow behavior in a graphene nanochannel demonstrated that slip flow arises, even at highly hydrophilic surface conditions. Thus, methodology was modified to facilitate a no-slip boundary condition to determine the viscosity and flow behavior of several different MD simulated water models; it was found that the TIP4P/2005 model best replicated water viscosity over a range of temperatures. Knowledge of surface interactions on graphene – water and flow behavior, and of water model property replication, are utilized for application and understandings in Chapters 4 and 5.

CHAPTER FOUR

THERMAL TRANSPORT I – INTERFACIAL HEAT TRANSFER

4.1 Introduction to Interfacial Heat Transfer

Interfacial heat transfer between two dissimilar media is investigated to characterize heat flow behaviors within a graphene – water system. Interfacial contact between two nanoscale media is indicated to heavily influence system properties and performances [23, 102, 103]. More specifically, diminished (or in some cases, enhanced) heat transfer behaviors are thought to arise in nanoscale environments where interfacial phenomena can amplify temperature discontinuities. In particular, interfacial thermal boundary (Kapitza) resistance, as the reciprocal of thermal boundary conductance, is the measure of an interface's resistance to thermal flow, and is an avenue used to characterize heat transfer within many types of systems. In nanoscale graphene – water environments, previous studies found interfacial thermal resistance to be dependent on the number of graphene layers and liquid layering density, while varying water block dimensions had little effect. As the ultimate goal of this thesis is to evaluate nanoscale convective heat transfer, understanding these previously studied interfacial heat transfer behaviors must be understood as they become integral components within future evaluations. The influence of differing interfacial conditions, as characterized by surface hydrophobicity/hydrophilicity, on thermal transport are evaluated by employing the same range of carbon – oxygen interaction strength values (Table 2.3) used to assess surface interactions and momentum transfer in Chapter 3. Thus, NEMD simulations are employed to evaluate thermal conduction and resistance at the interface between graphene and stationary liquid water by imposing a temperature gradient across the system and evaluating heat addition/subtraction to the system.

4.2 Setup and Simulation Details

In this particular study, the TIP4P/2005 water model is employed for heat transfer assessments as it was found to more accurately replicate water viscosity values over a wide range of temperatures (Chapter 3.3); this is of the upmost importance for later studies on convection. Employing the earlier stated parameters for graphene and water, and the method of Alexeev et al. [23], a $3.0\times3.0\times5.0$ nm^3 block of liquid water molecules (corresponding to 1734 water molecules of $\rho = 1000$ kg/m^3) is sandwiched between two blocks of four graphene layers (3.0×3.0 nm^2, with an x-axis interlayer spacing distance of $d = 0.335$ nm between each sheet) along the x direction. Two supplementary layers, are added to each graphene block to act as the "hot" and "cold" heat baths (or thermostating layers) for establishing a temperature gradient. In generating a temperature gradient in a periodic system, induced energy will travel in both the positive and negative ($+x$ and $-x$, in this case) directions from its place of origin. Thus, to account for heat flow across the periodic image, a symmetric copy of the aforementioned system is introduced along the x-axis. This effectively renders the system to behave as if each water block is confined between eight total graphene sheets. The inner-most four graphene layers are selected for thermostating to negate the effects of water in direct contact with a thermostating layer.

The 2D-slab method is not employed in this investigation; PBCs in all three axis directions are utilized. Systems are relaxed and equilibrated in the *NPT* ensemble at a temperature of $T_0 = 300$ K and pressure of 1.0 bar for 0.5 ns with a 1.5 fs timestep. After relaxation, Nose-Hoover

thermostating techniques are applied to the "hot" (T_h) and "cold" (T_c) graphene layers as $T_{h,c} = T_0 \pm \delta/2$ where δ = 100 K, respectively. Heat flux and temperature data are periodically collected throughout the duration of this phase (t = 2.5 ns); graphene and water temperature data are recorded into 100 equally spaced bins along the x-axis direction. A schematic of the system is shown in Fig. 4.1.

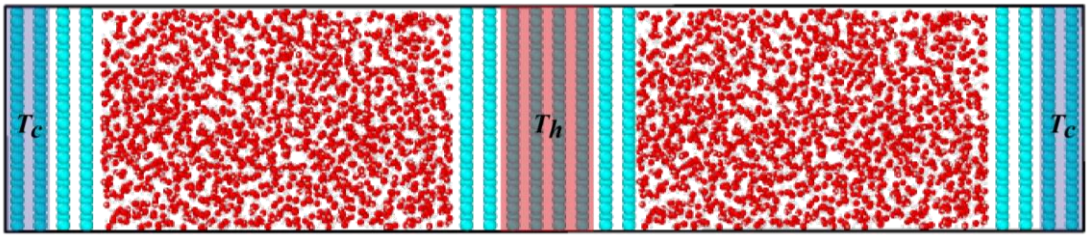


Figure 4.1. Setup schematic for the determination of interfacial thermal resistance. Heat periodically flows from T_h to T_c with the black outline defining the periodic boundary.

Upon analysis of results, the interfacial resistance, $R_{w/f}$, can be determined as an extension of Fourier's law, written as:

$$R_{w/r} = \frac{\Delta T}{J}, \tag{4.1}$$

with

$$J = 0.5\frac{d}{dt}\Delta E(t), \tag{4.2}$$

where ΔT is the temperature jump at the interface and J is the heat flux across the interface. Evaluation of resulting temperature profiles (Fig. 4.2a) enable for analysis of the water temperature gradient across the system and thus, temperature jump at the wall; heat flux across the system (Fig. 4.2b) is calculated from the recorded energy addition/subtraction by the thermostating layers. As the system is periodic in nature and heat flows in both the positive and negative directions, heat flux, being a measure of per unit time and area (W/m^2), is determined as half the energy conducted from the T_h to T_c heat baths.

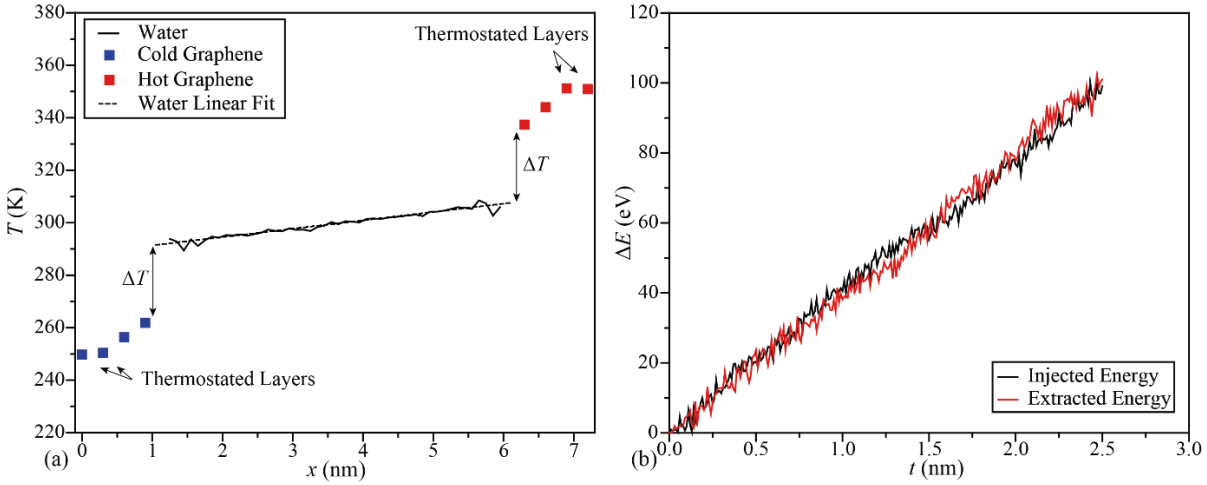


Figure 4.2. (a) Temperature across one side of the periodic domain, and (b) energy injected/extracted by the thermostated graphene layers.

4.3 Interfacial Heat Transfer Analysis

As respectively illustrated in Figs. 4.2a and 4.2b, the resultant temperature profiles and the recorded energy injection/extraction from the thermostated graphene layers are analyzed to compute $R_{w/f}$ via Eq. (4.1). As clearly seen in Fig. 4.2a, statistical fluctuations in recorded temperature inhibits pin-pointing an exact value of water temperature at the graphene interface, thus hindering the determination of temperature jump at the "hot" and "cold" sides of the water block. As surmised by a previous study [23], these fluctuations primarily arise due to influences of interfacial phenomena on liquid layering densities at the wall; to circumvent these issues, a linear regression is fit to the bulk region of water temperature profiles to obtain an approximate interfacial temperature. As detailed in Chapter 3, the bulk region is roughly 10 molecular diameters away from the interface and is outside the area affected by large density fluctuations caused by interfacial phenomena. For each surface condition, the recorded energy from the "hot" and "cold" thermostats (Fig. 4.2b) are evaluated to compute the heat flux, J [Eq. (4.2)], across the system.

Analysis of each surface condition yields significant influence on resulting interfacial heat transfer behaviors, as illustrated in Fig. 4.3. $R_{w/f}$ is seen to decrease in an exponential manner by roughly one order of magnitude for the range of tested C-O interaction strength values. In a comparable study employing the SPC water model and Tersoff potential for graphene description, interfacial thermal resistance was found to decrease in similar form as a relation between $R_{w/f}$ and WCA. Moreover, and although the same study also found interfacial thermal resistance to be dependent on the number of graphene layers, we only investigate the use of two graphene sheets as the number of layers is not this thesis' current focus. However, the behavior of interfacial thermal resistance, no matter the number of graphene layers, is shown to be highly dependent on surface interactions.

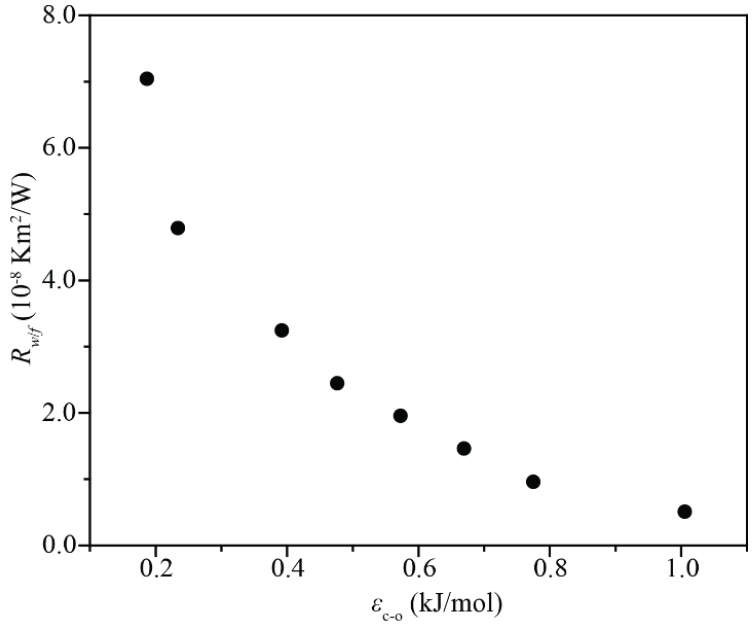


Figure 4.3. Interfacial thermal resistance decrease as a function of interaction strength.

To understand this behavior, we look to assess the liquid layering density at the interface for each $\varepsilon_{c\text{-}o}$ value. In conjunction with this thesis' previous study on wettability and as suggested

by the interfacial water density profiles shown in Fig. 4.4, graphene and water have an increased affinity for one another at larger interaction strengths producing more hydrophilic conditions; this, in turn, allows for a greater number of liquid water molecules to populate the areas closest to the walls. In agreement with previous findings [19, 23, 104], increased interfacial densities allow for more molecules to interact with the graphene wall, thus enabling for energy to be more easily transferred to the bulk water and yielding less thermal resistance across the interface. Conversely, at more hydrophobic surface conditions stemming from lower interaction strengths, a decrease in water density at the interface inhibits effective heat transfer due to a smaller amount of molecules available to receive heat from the wall; hence, $R_{w/f}$ is increased at higher values of $\varepsilon_{c\text{-}o}$.

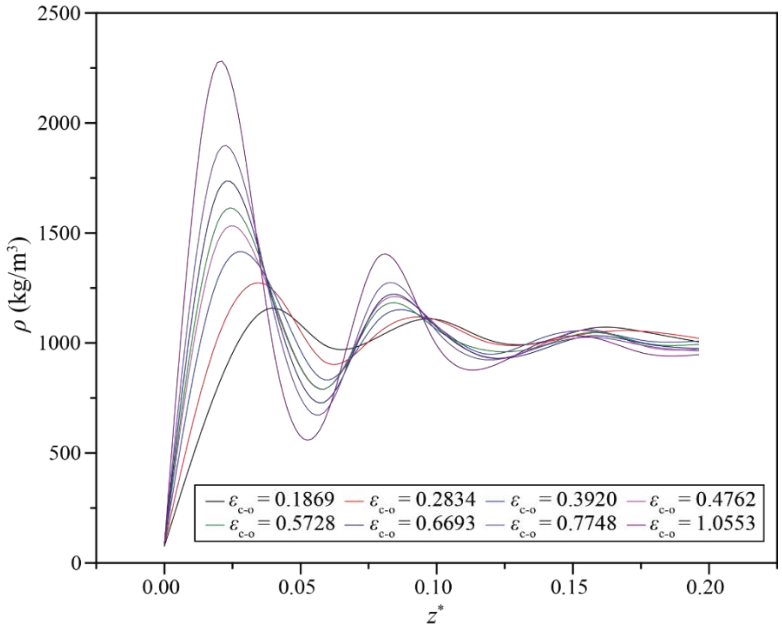


Figure 4.4. Magnified liquid water density at the interface for varying levels of C-O interaction strengths ($\varepsilon_{c\text{-}o}$).

4.4 Interfacial Heat Transfer Conclusion

Surface interactions are shown to be highly influential on heat transfer in nanoscale environments as characterized by the interfacial thermal resistance between graphene and water. Energy is found to be more easily transferred across the solid – liquid interface when there is a higher density of available energy carriers, whereas lower interfacial liquid densities act as a barrier inhibiting heat from across the system. Thus, nanoscale heat transfer is shown to be highly dependent on interfacial phenomena; this study is highly critical the examinations of Chapter 5, where thermal transport is further explored.

CHAPTER FIVE

THERMAL TRANSPORT II – INVESTIGATION INTO THE MICROSCOPIC MECHANISMS INFLUENCING CONVECTIVE HEAT TRANSFER OF WATER FLOW IN GRAPHENE NANOCHANNELS

A version of this chapter was originally published by Drew C. Marable, Seungha Shin, and Ali Yousefzadi Nobakht:

D.C. Marable, S. Shin, A. Yousefzadi Nobakht, "Investigation into the Microscopic Mechanisms Influencing Convective Heat Transfer of Water Flow in Graphene Nanochannels," *International Journal of Heat and Mass Transfer*, 109 (2017) 28-29.

With the exception of formatting changes, the removal of Equation 1 (in the published version), and abstract modifications to better suit this thesis, this article is as published in the listed publishing journal; no revisions to data or findings have been made. This student, Drew Champion Marable, acted as the principal investigator and led all research efforts including simulation setup, testing, analysis, and writing; Dr. Suengha Shin, the student's advising professor and lead principal investigator, facilitated the means to conduct this investigation and guidance in the form of topic direction, analysis, and writing. Ali Yousefzadi Nobakht acted as a co-principal investigator and assisted in final analysis and manuscript writings.

5.1 Abstract

This chapter both furthers the investigations of Chapter 4 on thermal transport, as well as a combined assessment of momentum (Chapter 3) and thermal transport. In this study, convection heat transfer is assessed for laminarly flowing liquid water through graphene nanochannels. As MD simulations provide insight on atomistic physical motion, the minute details and mechanisms influencing overall heat transfer behaviors can be directly assessed. Thus, despite the presence of unrealistic axial conduction from temperature resetting and periodic boundary conditions within MD, hydrodynamically and thermally fully-developed water flow conditions are observed. It is indicated that the physics of convective heat transfer deviate from traditional macroscale theory as the no-slip boundary condition is violated with dimensional sizes descending towards the nanoscale; investigation into hydrodynamic slip and thermal slip, termed microscopic mechanisms, is performed for their influence on nanoscale convective outcomes. The parameters of graphene-water interaction strength, channel height, water velocity, and wall temperature are manipulated to evaluate resultant convection behaviors while comparing the effects of differing magnitudes of microscopic mechanisms imposed under various test conditions. This study finds microscopic interfacial mechanisms to significantly augment momentum and thermal behaviors and thus the conduct of convective heat transfer. Hydrodynamic and thermal slip are strongly correlated in all test case scenarios with the exception of velocity manipulation; the influence of thermal slip is found to dominate over that of hydrodynamic slip as surface advection is insignificant in high heat flux environments. Convective performance correlation is suggested as the ratio of thermal slip length to system size.

5.2 Introduction

The development of nanoscale electrical and mechanical devices has presented new challenges in thermal management and heat dissipation as these issues become important at smaller dimensional sizes [1]. The incorporation of nanochannels as a cooling method to efficiently remove excess heat is one avenue suggested for thermal management in these small scale devices [5, 7, 105, 106]. Through previous works [6, 107], graphitic materials, and in particular the two-dimensional (2D) material graphene, has been identified as a material to improve microchannel thermal performance due to its excellent thermal conductivity, high surface-to-volume ratio, and ability to most effectively reduce the overall thermal resistance, as compared to that of more common silicon and aluminum substrates, when used as the primary substrate material of a microchannel heat sink [24]. Integration of graphene presents itself as a unique material for liquid cooling devices as 2D materials enable for the possibility of a single-layer channel wall and thus, effective heat dissipation devices at further reduced dimensional scales. In graphene-applied fluid cooling systems, graphene interlayer interactions are much weaker than intralayer interactions, therefore more emphasis and influence is placed on graphene-fluid interactions to dictate overall system performance.

The process of convection heat transfer in the macroscale realm has been thoroughly studied and is well established based on the no-slip boundary condition in which it is theorized that the fluid velocity at the wall should be equivalent to the wall velocity [108]. However, in contradiction to this theory, numerous studies have shown that at much smaller scales (or nanoscale) the no-slip boundary condition in liquids does not hold true and gives way to the development of slip flow as a result of surface effects dominating fluid flow behavior [8, 9, 11, 12, 17, 19-21, 109, 110]. Furthermore, the convection heat transfer process, characterized by the dimensionless Nusselt number, *Nu*, has been observed to deviate from that of traditional theory as dimension sizes decrease into the micro- and nanoscale realm [7, 11, 14-16, 111]. Reports indicate that temperature discontinuity (or temperature jump) at the wall due to interfacial thermal resistance decreases interfacial fluid temperature gradients and ultimately yields deviated convective behaviors from that of the macroscale [16, 22, 24-26].

Although the study of nanoscale fluid flow characteristics and deviations from established theory have been extensively studied [13, 19-21, 112], investigation into nanoscale convection heat transfer has been relatively unexplored. The study of sub-micrometer environments is necessary to fully understand momentum and heat transfer deviation from traditional theory [18]. Convection by monatomic molecules (e.g., Ar) has been the subject of a previous MD study [16]; however, the convective behaviors of complex liquid flows must be characterized and better understood within the nanoscale realm as liquid water is predominately employed as a liquid cooling media in many macroscale and microscale heat dissipation apparatus. In addition, convection in high-slip liquid fluid flows, as with 2D materials and increasingly hydrophobic interfaces, must be examined to improve understandings of momentum and energy transport within nanoscale systems [18].

Therefore, the behaviors and underlying mechanics within the nanoscale convective heat transfer process of liquid water, a complex fluid, flowing through nanochannels with double-layer graphene (DLG) acting as the channel walls are evaluated using non-equilibrium molecular dynamics (NEMD) techniques utilizing the LAMMPS package [27]; the majority of simulations relied on Extreme Science and Engineering Discovery Environment (XSEDE) resources [113].

The effects of various fluid-wall interaction strengths, channel heights, water velocities, and wall temperatures, in addition to their subsequent interfacial phenomena, are discussed.

5.3 Methodology

5.3.1 Simulation Details

Nanochannels consist of two parallel walls held into position using weak harmonic springs at a specified *z*-axis spacing, with each wall of the nanochannel being composed of double-layer graphene (DLG). From initial assessments of single-, double-, and triple- layer graphene for viable system wall composition, DLG is selected for its ability to ensure that the fluid-interacting wall is not directly thermostated, which can potentially result in molecular movement distortions and the reduction of data accuracy, as in the case of single-layer graphene. Moreover, in addition to increased computational efficiency over that of triple-layer graphene, DLG is chosen as multiple interlayer interactions are excluded to allow for a more direct focus on interfacial interactions and their subsequent effects.

The TIP4P/2005 [69] model is employed for the simulation of liquid water due to its predictable replication of ambient bulk water properties [114] with O-H bond length of 0.09572 nm, H-O-H bond angle of 104.52°, and charges of O ($-1.04e_c$) and H ($0.52e_c$), where e_c is the charge of an electron. Here, a dummy atom (or massless charge site) M is introduced 0.01546 nm away from the O atom to improve electrostatic distribution around the water molecule. In addition to electrostatic forces, the dispersion/repulsion force is considered for intermolecular interactions and is modeled as the 12-6 Lennard-Jones (LJ) potential mode using Eq. (2.6). For the dispersion/repulsion force between water molecules, only O-O interactions are considered with parameters of $\varepsilon_{o\text{-}o}$ = 0.7748 kJ/mol and $\sigma_{o\text{-}o}$ = 0.3159 nm. Water molecules are kept rigid, maintaining bond length (O-H) and angle (H-O-H) constant using the SHAKE algorithm [72]. Liquid water molecules corresponding to a density of ρ = 1000 kg/m^3 are placed in-between the two nanochannel walls; an additional 0.25 nm of spacing between the block of liquid water molecules and each nanochannel surface is added so to account for the water unoccupied volume [104, 115, 116].

Intralayer carbon interactions are modelled with the Tersoff-Brenner [59] potential, and interlayer carbon interactions are modeled by the 12-6 LJ potential with parameters from Ref. [77]. Water-carbon interactions are also described by the 12-6 LJ potential, where only the interactions between the carbon and oxygen atoms are defined so to increase computational efficiency; LJ interactions between carbon and hydrogen atoms were not introduced as these types of interactions are deemed negligible [78]. Moreover, previous investigations [45, 117], in which interactions between carbon and hydrogen atoms are neglected by modelling interactions between the water molecules and graphene atoms via dispersion (or van der Waals) forces, also employ this method of accounting for all water-graphene interactions by the LJ carbon-oxygen potential. The LJ values characterizing carbon-oxygen interactions were selected as $\varepsilon_{c\text{-}o}$ = 0.4763 kJ/mol and $\sigma_{c\text{-}o}$ = 0.319 nm to obtain the most recent experimental water contact angle on a contaminant-free graphitic surface [88-90]. The cut-off distance for all Lennard-Jones interactions is r_c = 1.0 nm.

The Verlet algorithm [65] is employed to integrate Newton's equations of motion within the simulation domain. In an effort to increase computational efficiency, periodic boundary conditions are applied to the *x*- and *y*- axis directions while the *z*-axis is fixed as non-periodic. The particle-particle particle-mesh (PPPM) technique [118] is utilized to compute Coulombic

interactions. The 2D-slab method [119] is employed to prevent Coulombic computations in the *z*-axis by adding a vacuum space and an electrostatic layer correction above and below the simulation domain to exclude wall-wall interactions across the *z*-axis boundary.

A channel height of H = 5.0 nm is chosen for the nanoscale evaluation of convection heat transfer. To ensure that fully-developed laminar flow inside the nanochannel is achieved, the corresponding channel length, L, for this height is determined through the inverse Graetz number, $Gz^{-1} = L/(D_H RePr)$, as a function of the Reynolds number, Re, Prandtl number, Pr, and hydraulic diameter, $D_H = 4A_c/P = 2H$, where A_c is the cross-sectional area and P is the wetted perimeter. Re and Pr were determined for each test case and calculated using characteristic lengths ($2H$) and the various required properties that were independently found from separate simulations (e.g., viscosity, thermal conductivity, etc.); properties were verified for consistency with previous reports and traditionally accepted values [69, 120, 121]. Re was found to be in the range of Re = 0.065 – 1.21 and Pr was determined as roughly Pr = 4.8. Statistical (or continuum) behavior of nanoscale fluid flow is expected to influence thermal and hydrodynamic development; in our system, this is characterized through the dimensionless Knudsen number, $Kn = \lambda/D_H$, as a ratio of the molecular mean free path, λ, to a characteristic length set as the hydraulic diameter. Since a liquid is employed as the working fluid within our simulations, we approximate the mean free path of liquid water as the average intermolecular distance between two water molecules as $\delta \sim \lambda \sim (V_m/N_A)^{1/3} \sim 0.3$ nm, where V_m is the molar volume and N_A is Avogadro's number [122, 123]; thus, we find our system Knusden (Kn, ~ 0.03) number value to be neither fully in the free molecular nor continuum regime [124, 125]. In addition to the possibility of size effects rending the no-slip boundary condition, based on continuum Navier-Stokes approximations, difficult to predict and/or invalid at the nanoscales [126-128], we hypothesized that continuum fluid behaviors may be observed with considerable influences from microscopic mechanisms (the potential presence of slip flow). From this, we anticipate potential slip flow behavior to require a larger channel entry length than of the length determined from setting Gz^{-1} = 0.05 for the continuum regime; hence, to ensure full flow development inside the nanochannel, a large value of Gz^{-1} = 0.4 is chosen [123, 129, 130]. Moreover, considering the potential effects of axial conduction as well as the areas of the liquid pumping and temperature rescaling regions, the respective channel length is found to be L = 12.0 nm. It must be noted that we do not claim for our molecular system (and others later described) to fully or statistically satisfy the aforementioned continuum based non-dimensional numbers, however to a certain extent, they do have the ability to be representative of similar physical description of continuum fluid behavior and is evidenced in the following sections by the observance of resulting laminar flows and the formation of fully developed velocity and temperature profiles. A channel width of W = 3.0 nm is selected and does not vary across all simulations; this value is chosen for computational efficiency as it was found that an increased channel width (W = 4.0, 5.0, and 6.0 nm) produced no influence on resulting convective behaviors.

5.3.2 Fluid Flow Method

Flow simulations typically utilize periodic boundary conditions coupled with a constant flow-driving body force in the *x*-direction, $f_{b,x}$, applied to each water molecule; this allows for the liquid to exit one side of the periodic box (outlet) and re-enter across the periodic boundary (inlet). However, due to the additional energy of the body force and the presence of a temperature gradient within the channel, the energy between the inlet and outlet is not conserved, thereby distorting the convective heat transfer process. In order to effectively simulate convective heat transfer, the

thermal pump method [16, 131] is introduced to the fluid domain. The thermal pump method divides the fluid domain into three separate regions: a forcing region, a temperature reset region, and a data collection region, as depicted in Fig. 5.1.

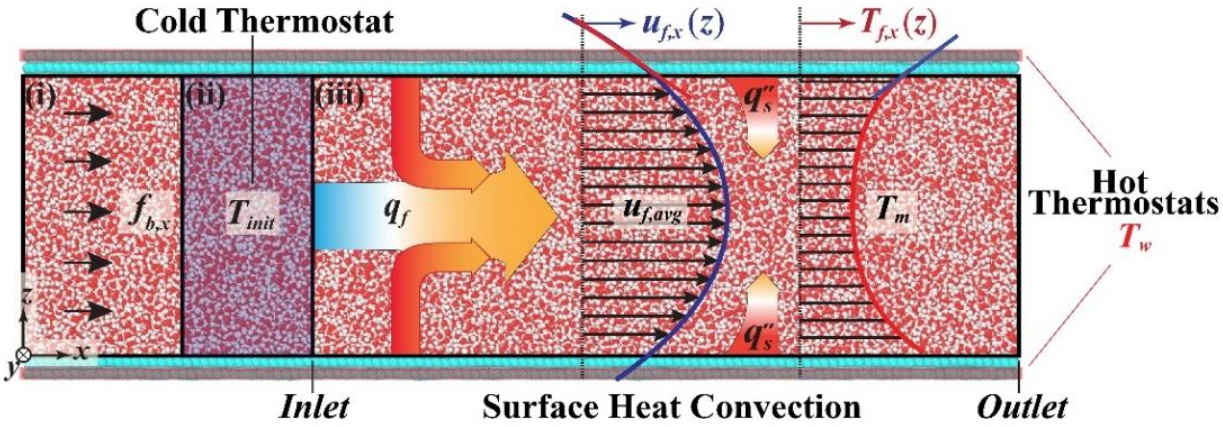


Figure 5.1. Schematic of the simulation domain separated into three regions: (i) forcing region, (ii) temperature rescaling region, and (iii) data collection region.

The forcing region is applied to the x-directional coordinates of 0.0 nm < x < 0.8 nm and is kept constant for all simulations; the water molecules inside this region experience a constant body force of $f_{b,x}$ to drive flow. Temperature resetting is performed only for water molecules inside the region of 0.8 nm < x < 1.4 nm; as with the forcing region, these x-directional coordinates are held constant for all simulations and test cases. In order to reset the water inlet temperature while maintaining the average velocity of water, thermal velocities are rescaled after removing the streaming velocity bias from the forcing region and then the previously removed streaming velocity bias is added back to the liquid water molecules. After the water molecules undergo temperature rescaling, molecules enter into the data collection region in which the convective heat transfer process is observed with water flowing from the inlet at a specified initial temperature and heated by the thermostated walls. Simulations are performed for a total duration of 7.0 ns using a 1.0 fs time step. An initial equilibration phase is implemented in the *NVT* ensemble (constant number of particles, volume, and temperature) [132, 133] for 1.0 ns to thermally relax the system. After the relaxation period (i.e., negligible fluctuation in T and u_f profiles), further simulation is carried out for 6.0 ns in the *NVE* microcanonical ensemble (constant number of atoms, volume, and energy) to update the velocities and coordinates of the fluid atoms; in this simulation period, the outer-most graphene walls are heated to specified constant thermostated temperature, T_w, while only the specified fluid domain area is rescaled to a constant inlet temperature, T_{init}, using Langevin thermostats [134].

The assessment of convection heat transfer is evaluated by means of collecting and analyzing velocity and temperature distributions, in addition to heat flux through the water-interacting walls. Velocity and temperature data are collected into equally distributed bins across the x- and z-axis directions while surface heat flux data in the z direction is recorded at similarly spaced channel subsections only along the x-axis (or flow) direction. Simulation data is collected over the simulation duration, after relaxation.

The use of thermostats to control temperature in MD simulations, as an artificial procedure of energy addition and extraction within systems, has the potential to cause unrealistic system

behaviors. However, as shown in Fig. 5.2, velocity distributions of the fluid agree well with the Maxwell-Boltzmann velocity distribution at a temperature of 300 K; thus, validating our use of the thermal pump method to effectively simulate the convective heat transfer process.

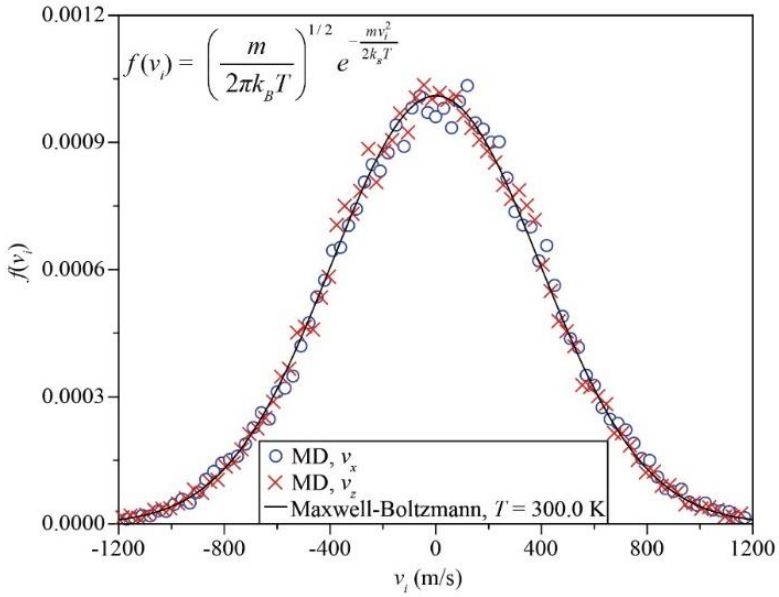


Figure 5.2. Maxwell-Boltzmann (MB) velocity distributions. The blue open circles and red cross markers represent that of the *x*- and *z*-axis distributions from MD, respectively; the black solid line corresponds to the MB distribution curve at 300 K.

5.3.3 Governing Equations

The convective heat transfer process is evaluated based on the local heat transfer coefficient, $h(x)$, at a *x*-directional position according to:

$$h = \frac{q_s''(x)}{T_w - T_m(x)}, \tag{5.1}$$

where $q_s''(x)$ is the local heat flux across the channel surface (interface between water and graphene, W/m^2), T_w is the wall temperature, and $T_m(x)$ is the local mean temperature at *x*, defined as:

$$T_m(x) = \frac{\int_0^H c\rho(z)u_{f,x}(z)T(x,z)dz}{\int_0^H c\rho(z)u_{f,x}(z)dz}, \tag{5.2}$$

where H is the channel height, c is the specific heat capacity and is assumed to be constant, ρ is the fluid density, $u_{f,x}(z)$ is the fluid velocity in the *x*-direction, and $T(x, z)$ is the fluid temperature along the *x*-axis. Using the local average velocity and kinetic energy obtained from MD allows for the determination of $u_{f,x}(z)$ and $T(x, z)$. The heat flux across the channel surface is calculated as [51]:

$$q_s'' = \frac{Q}{A_s \Delta t} = \frac{1}{V}\left\{\sum_i e_i u_{i,z} + \sum_{i<j}\left[f_{ij}\cdot\left(u_i + u_j\right)\right]z_{ij}\right\}, \tag{5.3}$$

where Q is the total energy that passes through the non-thermostated walls, A_S is the wall surface area interacting with water, Δt is the elapsed time, V is the volume of the simulation domain, e_i is the internal energy of the atom, $u_{i,z}$ is the i-th atom velocity in the z direction, $\boldsymbol{u}_i$ and $\boldsymbol{u}_j$ are the velocities of atoms i and j, $\boldsymbol{f}_{ij}$ is the pairwise force vector between different atoms, and z_{ij} is the directional position vector between atoms i and j. Traditional determination of convection heat transfer by internal flow is characterized through the non-dimensional Nusselt number, Nu_D, as a ratio of convection to conduction normal to the interface. By combining Eqs. (5.1), (5.2), and (5.3), we evaluate Nu_D as:

$$Nu_D = \frac{hD_h}{k_f} = \frac{2Hq_s^{"}}{k_f\left[T_w - T_m(x)\right]}, \tag{5.4}$$

where k_f is the thermal conductivity of the fluid. Without advection effects, q_s" is equivalent to water conduction heat flux in the z direction at the channel surface; i.e., $q_s" = -k_f(\partial T/\partial z)|_{z=0}$. h and Nu_D are also calculated by using the conduction heat flux based on the temperature gradient at the wall as:

$$h = \frac{k_f}{T_w - T_m(x)}\left.\frac{\partial T}{\partial z}\right|_{z=0}, \tag{5.5a}$$

and

$$Nu_D = \frac{hD_h}{k_f} = \frac{2H}{T_w - T_m(x)}\left.\frac{\partial T}{\partial z}\right|_{z=0}. \tag{5.5b}$$

The use of these two methods allow for comparative evaluation of nanoscale convective phenomena by accounting for heat flux across the channel surface, interfacial water conduction, and heat changes due to local advection. In addition, hydrodynamic and thermal slip at the wall are used to characterize and better identify underlying microscopic mechanisms contributing to the behavior of convection heat transfer within tested systems. The hydrodynamic slip length is utilized to identify the flow behaviors within each system and characterized as:

$$l_s = \frac{\Delta u_{f,w/f}}{\left.\left(\frac{\partial u_{f,x}}{\partial z}\right)\right|_{z=0}}, \tag{5.6}$$

where l_s is the slip length, $\Delta u_{f,w/f}$ is the difference between the fluid velocity at the wall and the wall velocity (u_w = 0 m/s), or slip velocity, and $(\partial u_{f,x}/\partial z)|_{z=0}$ is the velocity gradient in the fluid. Similar to the hydrodynamic slip length, fluid thermal behaviors at the interface are identified by the thermal slip length to relate the effect of temperature jump at the interface and interfacial thermal resistance, or Kapitza resistance, according to:

$$l_k = k_f R_{w/f} = \frac{\Delta T_{w/f}}{\left.\left(\frac{\partial T}{\partial z}\right)\right|_{z=0}}, \tag{5.7}$$

where l_k is the thermal slip length, $R_{w/f}$ is the interfacial thermal (Kapitza) resistance, $\Delta T_{w/f}$ is the difference between the fluid temperature at the wall and the wall temperature or the fluid temperature jump at the wall, and $(\partial T/\partial z)|_{z=0}$ is the fluid temperature gradient at the wall. Extrapolating a quadratic function to the wall allows for the determination of $\Delta T_{w/f}$ and $(\partial T/\partial z)|_{z=0}$.

5.3.4 Control Parameters

Previous reports [7, 16, 135] indicate that microscopic mechanisms, characterized by hydrodynamic and thermal slip at the interface, alter channel flow characteristics at smaller scales to yield deviated convective behaviors from that of the theoretical macroscale Nu_D value for fully-developed laminar flow in-between two parallel plates at constant wall temperature [136, 137]. Varying magnitudes of microscopic mechanisms are expected to emerge as flow characteristics are known to differ with wall wettability ($\varepsilon_{c\text{-}o}$), channel height (H), water velocity ($u_{f,avg}$), and wall temperature (T_w). Therefore, the influence of hydrodynamic and thermal slip on subsequent nanoscale convection heat transfer behaviors are assessed for the imposed test conditions of $\varepsilon_{c\text{-}o}$, H, $u_{f,avg}$, and T_w.

Characterized by the wetting contact angle on the wall surface, the influence of wall wettability is performed by means of controlling the LJ $\varepsilon_{c\text{-}o}$ parameter [36]. Manipulation of this parameter allows for tuning the graphene wall to become either more hydrophobic or hydrophilic; decreasing the LJ $\varepsilon_{c\text{-}o}$ value leads to reduced water-carbon interaction and produces to more hydrophobicity, while an increase in $\varepsilon_{c\text{-}o}$ value enhances interactions to yield more hydrophilicity. Selected values $\varepsilon_{c\text{-}o}$ of 0.1869, 0.2834, 0.3920 (Werder et al. [36]), 0.4763, 0.5728, 0.6693, 0.7748 ($\varepsilon_{c\text{-}o} = \varepsilon_{o\text{-}o}$), and 1.0553 kJ/mol were found to represent contact angles of 135°, 114°, 91°, 68°, 42°, 18°, 0°, and 0°, respectively, to assess varying magnitudes of hydrophobic and hydrophilic graphene wall interactions with water.

Channel heights in the range of H = 4.0 to 8.0 nm are chosen to assess convection heat transfer size dependence in nanochannels; this range of channel heights was selected so to ensure the appearance of regions with constant bulk density of water and for computational affordability. Moreover, systems with channel heights of less than 4.0 nm were found to be unstable and produce unreliable data; we attribute instabilities in this range to large temperature and pressure gradients imposed by the thermal pump method in these smaller volumes. In the same manner as determining the initial dimensions of 12.0×3.0×5.0 nm^3, Knusden numbers for the range of selected channel heights are also in the slip flow regime with values of Kn = 0.0375, 0.0300, 0.0250, 0.0214, 0.0188 for channel heights of 4.0, 5.0, 6.0, 7.0, and 8.0 nm, respectively. Thus, we maintain a constant Gz^{-1} = 0.4 for each channel height to obtain the resulting dimensions of 8.0×3.0×4.0 nm^3, 12.0×3.0×5.0 nm^3, 16.0×3.0×6.0 nm^3, 22.0×3.0×7.0 nm^3 and 28.0×3.0×8.0 nm^3 and correspond to 3282, 6117, 9897, 15736, and 22959 water molecules included in the system, respectively. Due to the varying amount of water molecules in each channel height simulation, the added flow-driving body force is specifically chosen for each channel height to ensure that the resulting water velocities are a constant 20 m/s across all tests of channel height variations; this is implemented for accurate comparison and evaluation of results.

The water flow velocity inside the graphene nanochannel is generated by means of applying a flow-driving body force to the forcing region of the liquid pump setup. The magnitude of the flow-driving force is incrementally increased from a minimum value of 9.6×10^{-15} N/molecule to a maximum value of 5.6×10^{-14} N/molecule in order to observe linearly increasing average water velocity ($u_{f,avg}$) from 10 m/s to 105 m/s, respectively.

Wall temperature effects on the convective heat transfer process within nanochannels are observed by increasing the thermostated wall temperature from a minimum temperature of T_w = 350 K to a maximum temperature of T_w = 1000 K. Wall heating via thermostats is only applied to the outer-most graphene sheets so that the potential effects of direct thermostating on the fluid-interacting wall will not cause distortions in the molecular movements of water.

Table 5.1. Simulation test case parameters.

Control Parameters	$\varepsilon_{c\text{-}o}$ (kJ/mol)	H (nm)	$u_{f,avg}$ (m/s)	T_w (K)
Control Range	0.1869 – 1.0553	4.0 – 8.0	10.0 – 105.0	350.0 – 1000.0
Constant*	0.4763	5.0	20.0	400.0

*Common simulation among all test cases

In order to allow for a common test case across all four investigated areas, unless otherwise stated simulation parameters are as follows: LJ interaction energy strength and distance are specified as $\varepsilon_{c\text{-}o}$ = 0.4763 kJ/mol and $\sigma_{c\text{-}o}$ = 0.319 nm, respectively, channel dimensions are kept constant as 12.0×3.0×5.0 nm^3 to correspond to 6117 water molecules filling the nanochannel, a flow-driving body force of 1.52×10^{-14} N/molecule is applied to the molecules in the forcing region which equates to a water velocity of approximately 20 m/s for these dimensions, the inlet temperature is held constant at T_{init} = 300 K, and the walls are thermostated to a temperature of T_w = 400 K. The tested control parameters are summarized in Table 5.1. Moreover, the amount of error is expected to be low with the level of uncertainty ranging from roughly 3% to 5%, which is estimated from three separate simulations for three different test cases (H = 4.0, 5.0, and 6.0 nm).

5.4 Results and Discussion

5.4.1 Velocity and Temperature Development

Resultant velocity and temperature distributions from MD are utilized to describe hydrodynamic and thermal development within simulated systems for the characterization of convection heat transfer. In each system setup, hydrodynamic flow fields are formed as water molecules exit the liquid pump and temperature rescaling regions; velocity distributions are determined from MD and in all test cases the flow is laminar with *Re* on the order of 1. As expected, velocity distributions remain invariant in the flow direction, which gives indication that fully-developed hydrodynamic conditions have been achieved. Fully-developed flow characteristics are observed to vary when manipulating the parameters of $\varepsilon_{c\text{-}o}$, H, $u_{f,x}$, and T_w; most noticeable are changes in flow behavior and average velocity distribution for differing magnitudes of wettability (Fig. 5.3). In this case, lower interaction strengths (more hydrophobic) result in a high velocity plug-like flow with little distribution curvature, whereas increasing $\varepsilon_{c\text{-}o}$ (more hydrophilic) possess a more parabolic velocity distribution curvature and exhibit lower average velocities. In analyzing velocity distributions and as portrayed in Fig. 5.3, slip flow behavior is present within all simulated test cases; slip effects and their influences on system behavior will be discussed later.

Water temperature distributions characterize thermal development inside the nanochannels as cold (T_{init} = 300 K) water leaves the inlet and flows past the heated walls; temperature distributions are the primary avenue used for the evaluation of convection heat transfer within the various system parameter configurations. Thermal development for each tested case is illustrated by its resulting isotherm, mean temperature distribution, and temperature evolution at various points along the x-axis as in Fig. 5.4; for visualization purposes, a nanochannel with dimensions of 22.0×3.0×7.0 nm^3 is chosen for depiction. While typically neglected in macrochannels, axial conduction is clearly present within the liquid water as shown in Figs. 5.4a and 5.4b. To an extent, the nature of our employed simulation method can induce unrealistic axial conduction as a temperature gradient will be imposed across the system domain due to water molecules interacting across the periodic image. However, while physical influences of the simulation setup and procedure must also be considered, the presence and magnitude of axial conduction is largely

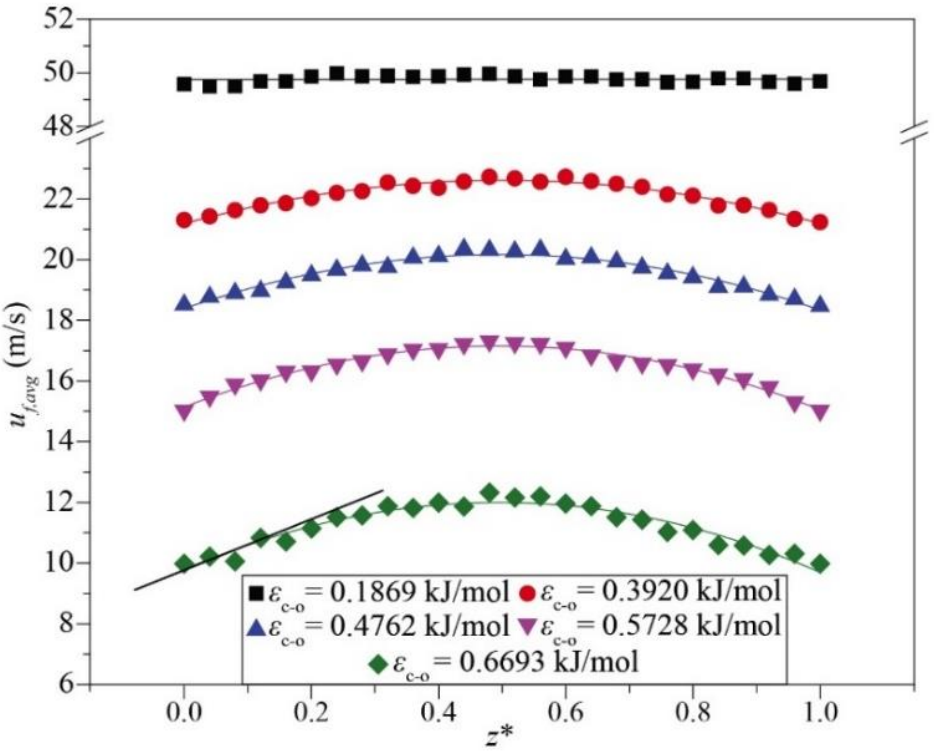


Figure 5.3. Velocity distribution across the dimensionless channel height ($z^* = z/H$, and H = 5.0 nm) with various wall-fluid interaction strengths ($\varepsilon_{c\text{-}o}$). With increasing $\varepsilon_{c\text{-}o}$, average velocity decreases while the parabolic curvature increases.

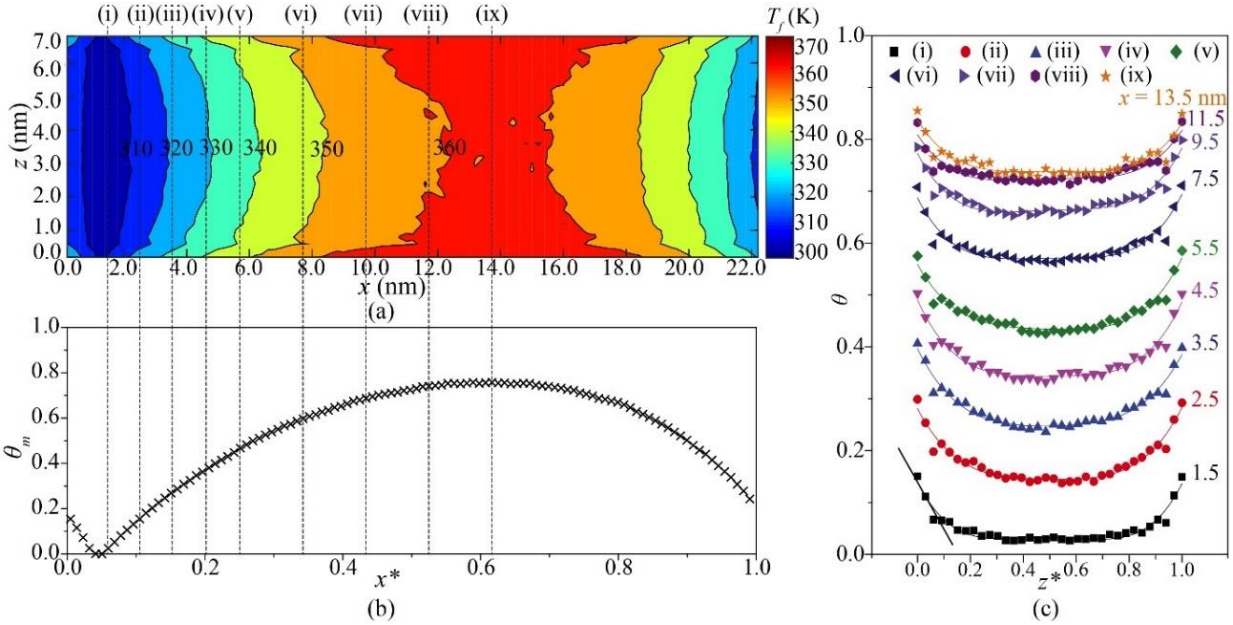


Figure 5.4. Temperature development inside a nanochannel with dimensions of 22.0×3.0×7.0 nm^3. (a) Isotherm diagram of temperature development (isothermal lines are inverted to better guide the eye.) (b) Non-dimensional mean temperature (θ_m) development in the x-axis flow direction. (c) Development of non-dimensional (θ) temperature profiles across the channel height (z-axis) at various x-directional points in the direction of the flow.

facilitated by the fluid flow and heat transfer behaviors of the nanoscale liquid media [138]. Therefore, the influence of axial conduction on thermal development is considered for all test cases within this assessment of the nanoscale convection process.

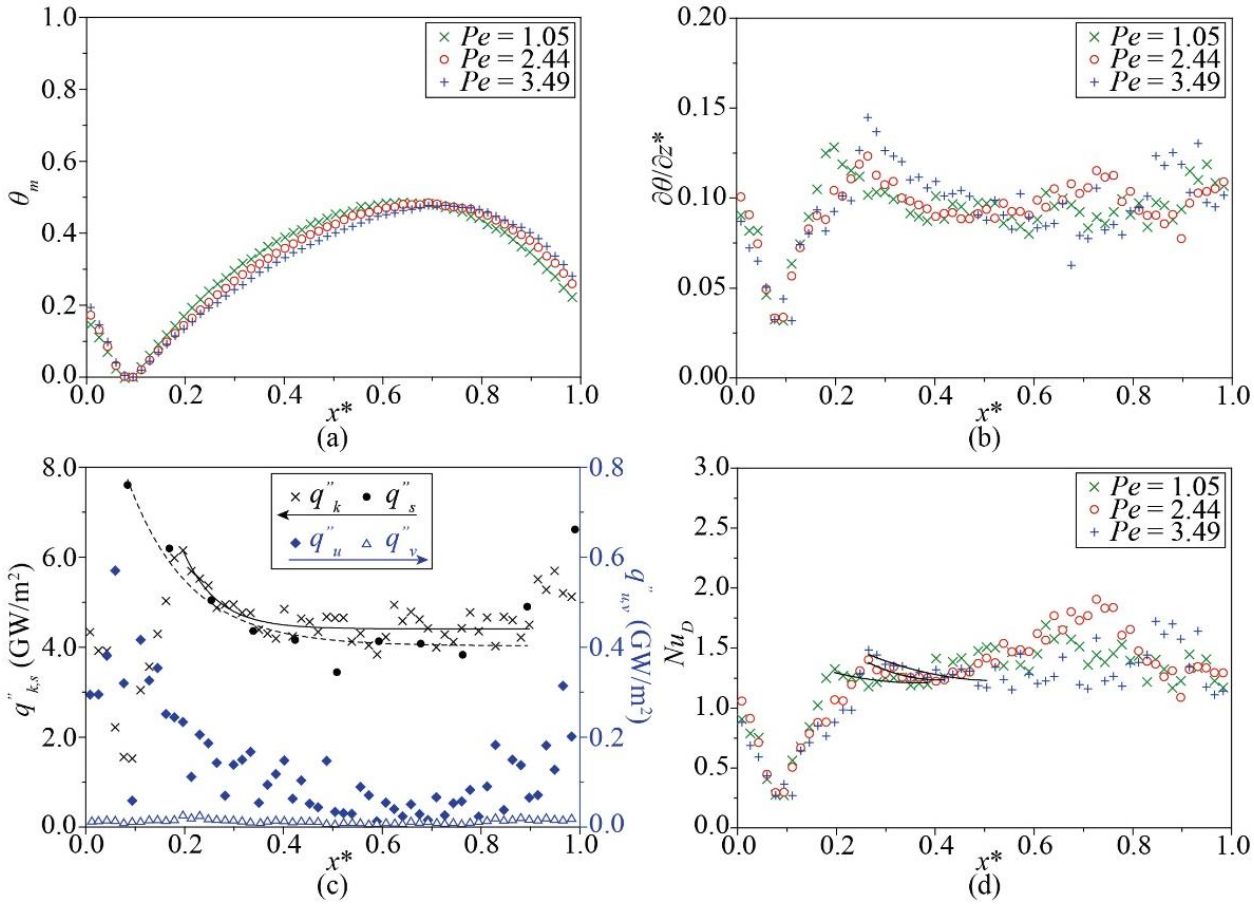


Figure 5.5. Flow development with axial conduction at different Peclet numbers showing (a) mean dimensionless temperature (θ_m) development, (b) dimensionless temperature gradient ($\partial\theta/\partial z^*$) at the wall, (c) comparison of local surface (q_s''), surface water conduction (q_k''), change of surface advection (q_u''), and viscous (q_v'') heat flux and (d) local Nusselt number (Nu_D).

Axial conduction can arise in instances of low *Re* and *Pr*, where thermal diffusion is more important than advection due to small inertia and high thermal diffusivity, to effectively distort the development of mean fluid temperature. Therefore, the significant parameter is the Peclet number, $Pe = RePr$; in laminar flows, previous reports indicate that axial conduction emerges at $Pe < 10$ and its influence decreases as *Pe* increases in micro and nanochannels [130, 138]. Since *Pe* numbers range from 0.8 to 6.0 for the varying parameters of $\varepsilon_{c\text{-}o}$, *H*, $u_{f,x}$, and T_w, axial conduction is indicated to be a present factor within all test cases. Thus, a decrease in mean fluid temperature downstream is expected due to the influence of axial conduction and the temperature rescaling region (low *T*) across the periodic image. Fig. 5.5a, showing the dimensionless T_m [$\theta = (T - T_{init})/(T_w - T_{init})$; $\theta = \theta_m$ when $T = T_m$] with respect to dimensionless channel distance from the entrance ($x^* = x/L$) for varying *Pe*, confirms the lessening influence of axial conductions influence within nanochannels at higher *Pe*. Despite the presence of unrealistic effects, the fluid temperature gradient at the surface decreases from the inlet and trends to a flattened profile that displays little

deviation as in Fig. 5.5b; this indicates that the internal flow is thermally fully developed. Although observation limitations within thermal development of internal flow may be present, this MD approach allows for the analysis of fully-developed convection behavior.

Local heat flux (q_s'') values must be determined according to Eq. (5.4) in order to evaluate the local Nusselt number (Nu_D) that characterizes convection. When utilizing the no-slip boundary condition in macroscale analysis, interfacial water conduction, as determined from the surface temperature gradient [$q_k'' = -k_f(\partial T/\partial z)|_{z=0}$], can replace surface heat flux (q_s''). However, slip flow exists in all tested systems. Thus, the supplied heat from the wall (q_s'') is unable to be replaced by interfacial conduction (q_k'') as slip flow contributions facilitate an increase in advection heat flux (q_u'') due to non-zero flow velocity at the surface, as in Fig. 5.3. q_u'' is calculated from the surface fluid velocity (or slip velocity, $u_{f,s}$) and temperature change ($\Delta T_{f/w}$) with an approximation of constant ρ and c ($q_u'' = \rho u_{f,s} c \Delta T_{f/w}$). Fig. 5.5c shows that q_u'' is at least one order of magnitude smaller than both q_k'' and q_s'', therefore q_u'' is negligible in the data collection region for fully-developed Nu_D calculations. As prescribed simulation conditions in MD induce large amounts of heat, heat flux with respect to viscous dissipation, $q_v'' = \mu(\partial u/\partial z)^2$ where μ is the dynamic viscosity of the water and is found from Ref. [32], is insignificant to influence q_k'' or q_s'' and can be ignored. Fig. 5.5c also shows close agreement between the determinations of q_k'' and q_s'' with a difference of only 9.32%; this comparatively small difference is attributed to negligible q_u'' and q_v''. Additionally, variations in water thermal conductivity near the interface are anticipated to influence the q_k'' calculation, however this contribution is expected to be minor as q_k'' and q_s'' are in relative agreement [139]. Therefore, due to the close agreement of heat flux calculation approaches and the computationally expensive procedure of determining localized heat fluxes (q_s'') within small regions, q_k'' is employed for calculations of the local Nusselt number in Fig. 5.5d. This method also displays the axial conduction's effect on the local Nusselt number in which Nu_D trend profiles are almost flat at lower *Pe*; conversely, higher *Pe* values give way to more exponential and traditional Nu_D trends. Here, we focus on fully-developed convection behaviors, rather than flow development in the entry region, which are properly characterized by the local Nusselt number, $Nu_{D,fd}$, due to attenuated axial conduction, as illustrated in Fig. 5.5d. Average Nu_D can also be calculated using $\overline{Nu}_D = (1/k)\int_0^L h(x)dx$, as it approaches that of local fully-developed Nu_D if the channel length is sufficiently long. However, as inclusion of entrance regions under the influence of unrealistic axial conduction may distort resulting values for average Nu_D (due to the limited simulation cell size), we report fully-developed Nusselt numbers, $Nu_{D,fd}$, for all test cases in the following sections.

5.4.2 Microscopic Mechanisms

In addition to hydrodynamic and thermal development, velocity and temperature distributions are employed to enhance clarity and understanding of microscopic mechanisms influencing simulated system behavior. Characterizing these mechanisms, or microscopic interfacial interactions, allows for hydrodynamic and thermal slip lengths, Eqs. (5.6) and (5.7), respectively, to be considered for their influence of system outcomes within convection assessments. Hydrodynamic slip length provides information describing fluid flow behavior, the potential effects of surface advection and friction heating, and slip flow magnitude; the thermal slip length relays the significance of temperature jump and Kapitza resistance to system performance. We report deviation from the no-slip boundary condition in all tested simulation cases with the emergence of hydrodynamic and thermal slip at the interface as characterized by l_s

and l_k, respectively, in Fig. 5.6. In consistency with our water volume definition, although there is a small amount of uncertainty, the first liquid layer or slab closest to the wall was defined as the liquid-solid boundary [49, 94] with Fig. 5.6 displaying omission of the water unoccupied volume. We acknowledge that a previous report indicates [140] hydrodynamic slip length to be independent from the shear rate in the linear regime. From this, we clarify that although our findings are seemingly in contrast to the mentioned reference, we attribute reported changes in hydrodynamic slip length to manipulation of our control parameters.

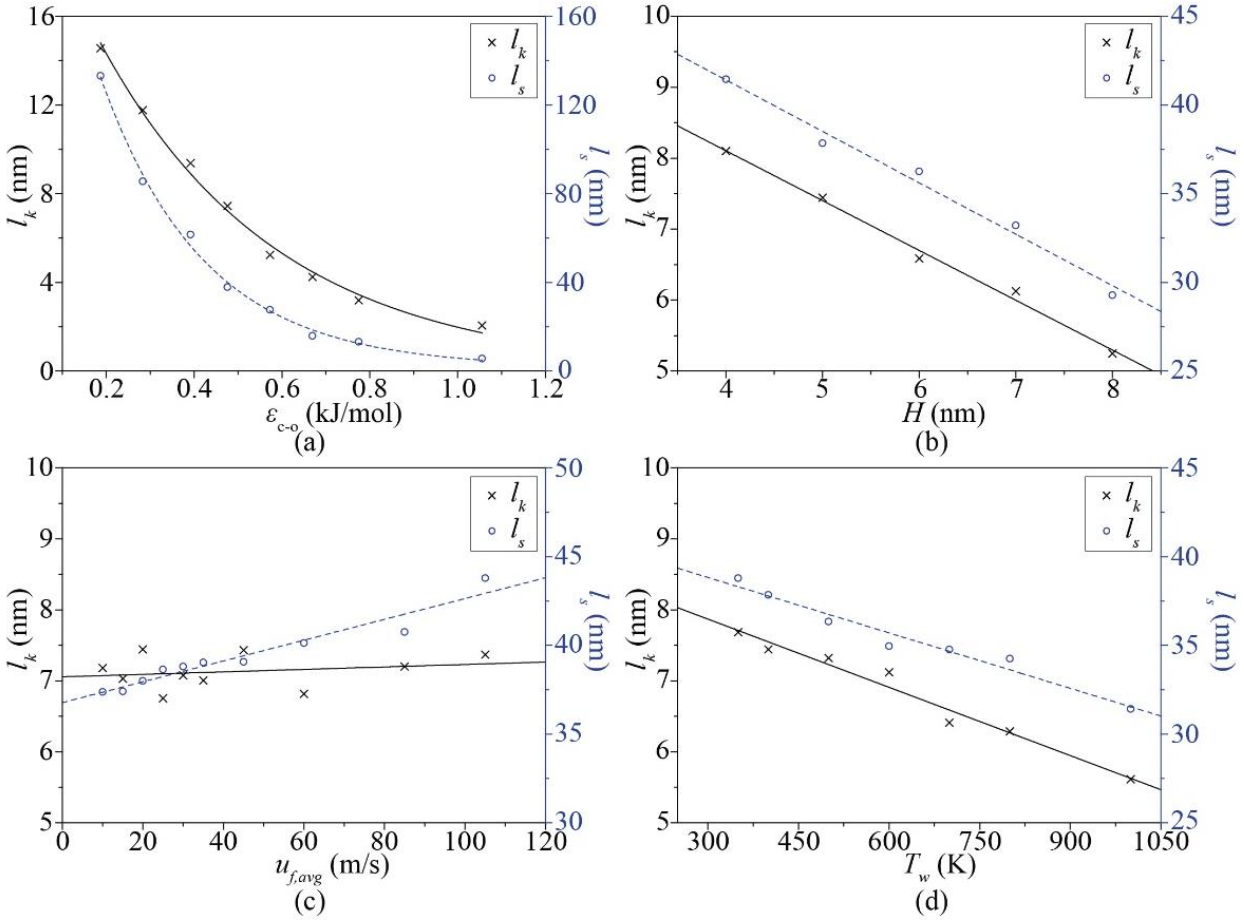


Figure 5.6. Thermal (l_k) and hydrodynamic (l_s) slip lengths for varying (a) interaction strengths ($\varepsilon_{c\text{-}o}$), (b) channel heights (H), (c) velocities ($u_{f,avg}$), and (d) wall temperatures (T_w); fit lines are added to better guide the eye.

Among all tested parameters, varying wall wettability produces the most dramatic changes in hydrodynamic and thermal slip lengths as in Fig. 5.6a. As a result of increasing hydrophilicity due to larger surface interaction strengths, and thus increased friction at the interface [10], hydrodynamic slip at the boundary decreases from l_s = 133.17 nm for highly hydrophobic interactions to l_s = 5.64 nm for highly hydrophilic interactions. Likewise, Kapitza resistance is seen to follow in a similar manner with thermal slip lengths exponentially decreasing from 14.55 and 2.05 nm for the largest variations of $\varepsilon_{c\text{-}o}$; we note that this observation of thermal slip length exponentially varying with liquid-solid interaction strength is consistent with previous reports [141, 142], however further assessment should be performed to validate this exponential trend in nanoscale liquid flows. This behavior stems from a larger accommodation of water molecules and

stronger coupling with the wall interface as interfacial interactions increase; therefore, temperature jump at the wall and thus, $R_{w/f}$ will decrease to allow for more effective heat transfer. Even with increasing interaction strengths past that at which results in a WCA of 0° ($\varepsilon_{c\text{-}o}$ = 0.7748 and 1.0553 kJ/mol) the no-slip boundary condition is still violated; this is attributed to the atomically smooth nature of 2D graphene sheets acting at the channel walls [94].

In Fig. 5.6b, an increase in channel height from H = 4.0 to 8.0 nm is shown to yield decreasing hydrodynamic slip lengths from l_s = 41.45 to 29.27 nm; this observation is consistent with a previous report [143] that attributes this behavior to the lessening effects of microscopic mechanisms at the interface projecting their influence on fluid behavior as dimensional scales increase. In comparable form, a similar decrease is observed for thermal slip length from l_k = 8.10 to 5.24 nm at the same range of channel heights. We further the referenced suggestion and infer this to also be true with regard to thermal behaviors; the significance of temperature jump at the wall and Kapitza resistance will cease to interfere with heat transfer behaviors as size trends towards macroscale.

In concurrence with previous reports [13, 94, 144], due to larger momentum difference at the liquid-solid boundary, hydrodynamic slip length increases with higher water velocities from l_s = 37.37 to 43.78 nm for the channel velocities of $u_{f,avg}$ = 10 and 105 m/s, respectively. However, unlike all other thermal slip length trends in other test cases, l_k with respect to changing velocity is seen to remain relatively constant at 7.13 ± 0.228 nm in Fig. 5.6c. While an increase in thermal slip length is expected as with hydrodynamic slip length, we propose that momentum changes at the surface due to increasing velocity are not significant enough to produce noticeable effects on the resulting thermal diffusion within the channel. To further support this claim, channel velocities are significantly smaller than calculated thermal velocities on the order of 680 m/s for resulting simulation water temperatures; therefore, it is inferred that manipulation of channel velocity will produce no meaningful change in thermal slip length until the fluid media velocity is on the order of its thermal velocity.

A decrease in hydrodynamic slip length from l_s = 38.78 to 31.41 nm is observed for increasing wall temperatures from 350 to 1000 K (Fig. 5.6d). This is contrary to conventional knowledge in which it might be assumed that higher fluid temperatures will yield increased water velocities, and thus increased slip lengths. While average velocities (at the same magnitude of prescribed flow-driving force) are seen increase from 18.47 to 34.17 m/s for T_w = 350 and 1000 K, respectively, this behavior is attributed to the fact that as temperature increases, atom kinetic energy and thus momentum transfer due to collisions will become enhanced to allow for decreasing slip lengths [145]. Similarly, enhanced heat transfer due to increased collisions at higher temperatures will allow for decreased Kapitza resistance [146] and thus more effective diffusion of heat from the wall to the water. Subsequently, with increasing thermostated wall temperature from T_w = 350 K to T_w = 1000 K thermal slip lengths are observed to decrease from l_k = 7.68 to 5.61 nm.

5.4.3 Fully-Developed Heat Transfer

Due to their negligible influence within macroscale convection analysis, the microscopic mechanisms of hydrodynamic and thermal slip at the interface are unaccounted for. Conversely, as dimensions decrease and efforts are made to assess nanoscale thermal analysis, microscopic mechanisms must be considered for their role within the convection process as their influence becomes magnified and projected on overall heat transfer performance. Subsequently, for all

simulated test cases the resulting behavior of convection heat transfer displays reduced Nusselt values from that of the theoretical macroscale fully-developed laminar flow, $Nu_{D,fd}$ = 7.541, as seen in Fig. 5.7. The presence and magnitude of hydrodynamic and thermal slip at the interface are shown to impede heat transfer from the graphene wall to the water and dictate the extent of convection effectiveness.

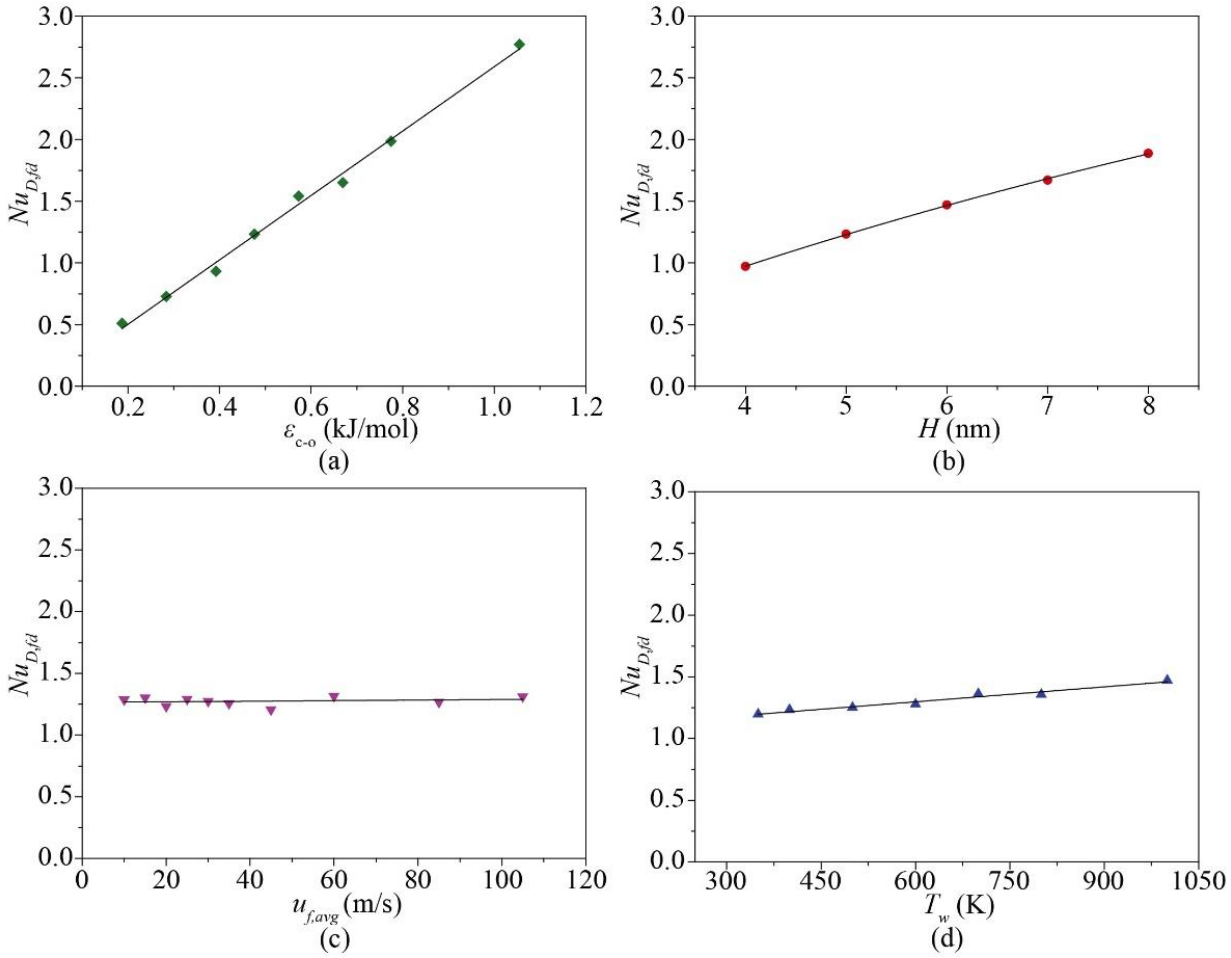


Figure 5.7. Fully-developed Nusselt number ($Nu_{D,fd}$) trends for varying (a) interaction strength ($\varepsilon_{c\text{-}o}$), (b) channel height (H), (c) water velocity ($u_{f,avg}$), and (d) wall temperature (T_w).

Manipulation of the water-graphene surface interaction strength yields significant enhancement to the convection heat transfer process as wall wettability is tuned from hydrophobic to hydrophilic (Fig. 5.7a); our results are consistent with previous reports [7, 16] which indicate that the microscale convection process will become enhanced as increased interactions between the wall and water allow for improved heat transfer. Results show an order of magnitude increase in heat transfer performance from $Nu_{D,fd}$ = 0.594 for the case of extreme hydrophobicity ($\varepsilon_{c\text{-}o}$ = 0.1869 kJ/mol) to Nu_D = 2.771 corresponding the extreme hydrophilicity case ($\varepsilon_{c\text{-}o}$= 1.0553 kJ/mol). This conduct stems from stronger interactions allowing more water molecules to come into contact with the wall, thus inhibiting momentum and advection effects at the interface as illustrated by decreasing hydrodynamic slip lengths. Likewise, thermal slip lengths are seen to decrease because of more wall-fluid interactions enhancing heat transfer at the surface as more

water molecules are available to remove heat from the wall, which is in agreement with previous findings [19, 23]. Density profiles for corresponding $\varepsilon_{c\text{-}o}$ values in Fig. 5.8, which are similar to that of another report [104], displays this increasing water molecule density near the interfacial regions that enable for enhanced heat transfer at higher interaction strengths.

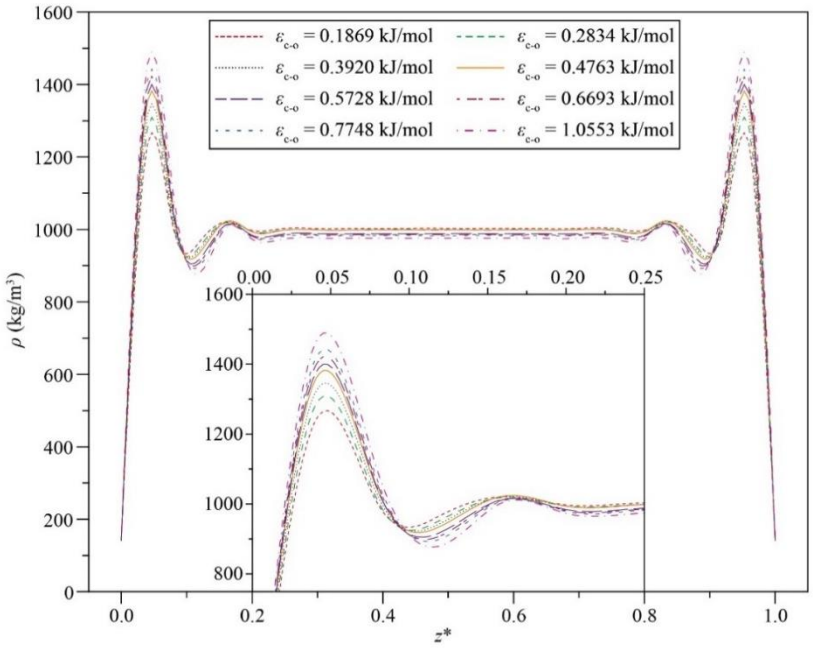


Figure 5.8. Density profiles for increasing values of solid-fluid interaction strengths ($\varepsilon_{c\text{-}o}$). The inset is a magnified image of density at the interfacial region.

As system size increases with channel height from H = 4.0 to 8.0 nm, convection performance displays enhancement with an increase towards that of macroscale behavior from $Nu_{D,fd}$ = 0. 97 to 1.88 as in Fig. 5.7b. It is known in conventional theory that as dimensional scales increase in size within fluid flow applications, Kn will decrease and cease to display slip flow characteristics with trends towards that of continuum behavior. In concurrence with theory and as supported by the aforementioned Kn calculations, hydrodynamic slip lengths, and thus momentum at the interface, are observed to decrease as the influence of solid-fluid interfacial mechanisms weaken with increasing channel dimensions. The same is true in relation to thermal slip; at nanoscales, increasing surface-to-volume ratio permits Kapitza resistance to become a substantial factor that distorts convective performance [11]. Contrary to the previous report by Ge et al. [16] indicating nanochannel size effects produce no detectable change in heat transfer behavior, our observations indicate that as dimensions increase, interfacial mechanisms (i.e., hydrodynamic slip and thermal slip, characterizing temperature jump and Kapitza resistance) gradually become insignificant to allow for more effective heat transfer and thus a trend of convective behaviors towards that of macroscale theory. Convection heat transfer is estimated to achieve macroscale behavior for water flow in graphene nanochannels at a channel height of 32.81 nm and/or 605.72 nm using linear and logarithmic fitting, respectively.

With respect to the influence of increasing water velocity inside the nanochannel from 10 m/s to 105 m/s, convection heat transfer behavior is observed to remain relatively constant and only deviates from $Nu_{D,fd}$ = 1.23 by 1.2% in Fig. 5.7c. Conventional knowledge of nanoscale flow

indicates that increasing channel velocity will yield increased slip lengths as a result of amplified momentum at the interface. Initially, it was assumed that this in turn would enable for more effective diffusion from the graphene wall to the water. However, we now suspect that insubstantial changes in momentum are not enough to produce noticeable effects on the resulting thermal diffusion within the channel. As a result, Kapitza resistance is left unaffected by momentum transport behaviors and produces no change in thermal performance.

As atom kinetic energy increases with thermostated wall temperature, more collisions at the wall-fluid interface occur to allow for enhanced momentum and heat transfer rates; this is verified by the observance of decreases in both hydrodynamic and thermal slip lengths. Signified by the behavior of these microscopic mechanisms, this subsequent improvement in energy transfer allows for enhancement to convective behaviors inside the nanochannel with an increase from $Nu_{D,fd}$ = 1.19 to $Nu_{D,fd}$ = 1.47 for the thermostated wall temperatures of T_w = 300 K and T_w = 1000 K, respectively (Fig. 5.7d). It is noted that although temperatures exceed that at which water would normally experience boiling, no phase change is observed due to the constrained simulation volume and rescaling of temperatures at the channel inlet [147].

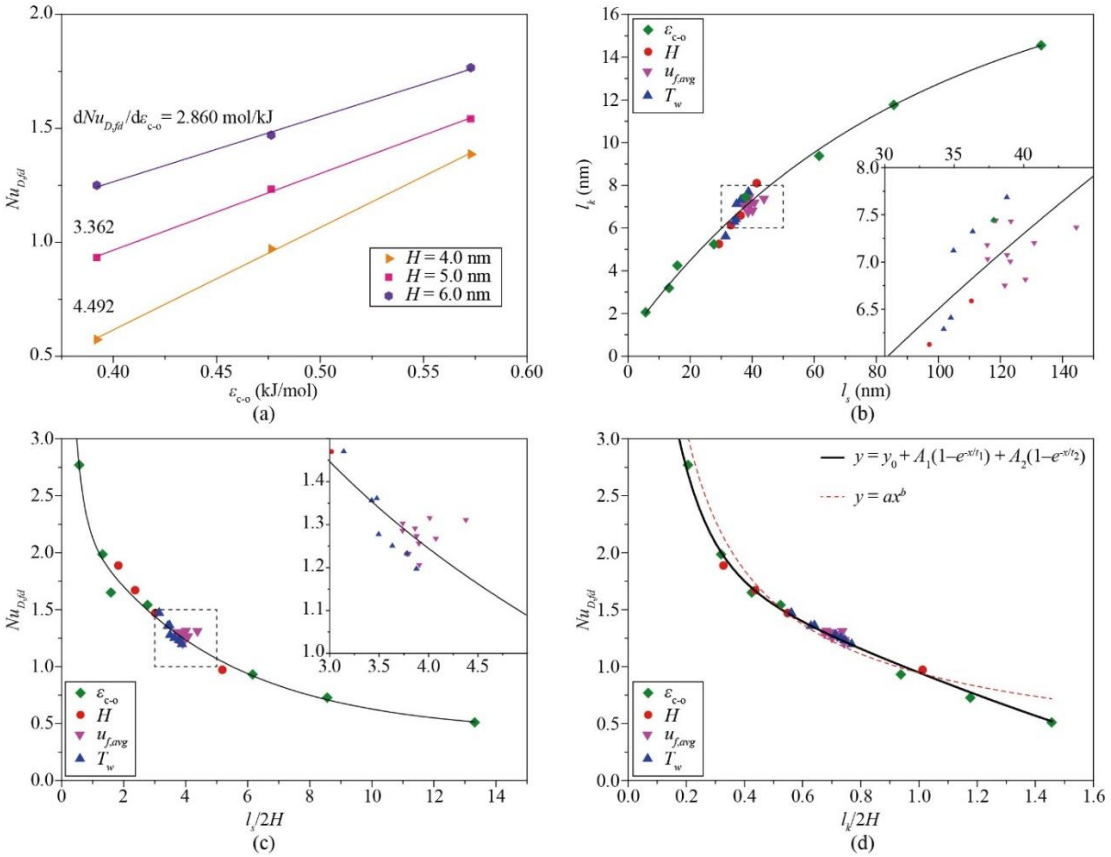


Figure 5.9. (a) Fully-developed $Nu_{D,fd}$ trends for increasing channel heights (H) at different carbon-oxygen interaction strengths ($\varepsilon_{c\text{-}o}$). (b) Comparison of l_s and l_k for all test parameters. (c) $Nu_{D,fd}$ values corresponding to normalized hydrodynamic slip lengths. (d) Fully developed $Nu_{D,fd}$ trend for normalized thermal slip length values.

To further validate and understand the microscopic phenomena influencing convective behaviors (Fig. 5.9), we investigate increasing channel heights of H = 4.0, 5.0 and 6.0 nm at varying carbon-oxygen interaction strengths, or magnitudes of wettability, ($\varepsilon_{c\text{-}o}$ = 0.392, 0.4763

and 0.5728 kJ/mol) in Fig. 5.9a. As found above in Fig. 5.6, increasing interaction strength produces the most drastic changes in the resulting values of l_s and l_k, and thus $Nu_{D,fd}$. However, manipulation of $\varepsilon_{c\text{-}o}$ yields that at smaller channel dimensions, the effects of surface interactions are magnified and project their influence over fluid-fluid interactions within the system to induce more noticeable modifications to overall convective outcomes. Conversely, as dimensional size increases we see a lessening influence of surface mechanisms to the convective heat transfer coefficient, which is consistent with the concept that convective behaviors deviate at nanoscales due to dominating surface effects. Therefore, convection heat transfer is dependent on relative magnitudes of microscopic mechanisms (hydrodynamic and thermal slip) when compared with dimensional size.

Hydrodynamic and thermal slip (l_s and l_k) under various test conditions display good correlation (Fig. 5.9b) although varying $u_{f,avg}$, which has minor influence on l_k, causes slight deviation as in the inset of Fig. 5.9b. This good correlation is attributed to similar control mechanisms in both interfacial momentum and thermal transport, such as strength and frequency of interactions between water molecule and surface. To evaluate the influence of size effects and these l_s and l_k together, $Nu_{D,fd}$ is plotted with respect to normalized slip lengths, $l_s/2H$ and $l_k/2H$, as respectively shown in Figs. 5.9c and 5.9d. Both collective $Nu_{D,fd}$ trends are well correlated with the normalized slip lengths and indicate that larger $l_s/2H$ or $l_k/2H$ results in greater discrepancies from macroscopic convective behavior; i.e., as slip lengths increase or system size decreases, $Nu_{D,fd}$ decreases. However, the correlation with $l_s/2H$ contains more deviation from the overall trend than that with $l_k/2H$; specifically, the deviation appears in the same area (dashed boxes) in Fig. 5.9b while no such deviation and better agreement is found in the trend of $Nu_{D,fd}$ with respect to $l_k/2H$. Therefore, l_k is inferred to be the dominant factor, particularly when surface heat flux is large enough to overcome the surface advection effects imposed by slip flow as in our simulation conditions. Correlation between $Nu_{D,fd}$ and $l_k/2H$ is identified as the black trend line equation of $Nu_{D,fd} = 7.544 - 5.595(1 - e^{-lk/10.838H}) - 5.554(1 - e^{-lk/0.2308H})$ in Fig. 5.9d; furthermore, the red trend line of $Nu_{D,fd} = 0.9452(l_k/2H)^{-0.7313}$ is identified as a simple fit with roughly 5% error, when $0.2 < (l_k/2H) < 1.2$, to estimate the macroscale value of $Nu_{D,fd}$.

5.5 Conclusions

Molecular dynamics simulations of water flowing in graphene nanochannels allows for investigations of the microscopic mechanisms influencing fully-developed convective heat transfer despite the presence of unrealistic axial conduction. Hydrodynamic and thermal slip are shown to be key manipulating factors in the characterization of nanoscale thermal performance. Strength and frequency of fluid-surface interactions influence both hydrodynamic and thermal slip, and thus lead to their strong correlation. However, microscopic mechanisms can be selectively controlled; for example, variation of average fluid velocity smaller than that of thermal velocity only has an effect on hydrodynamic slip (with negligible change in thermal slip). Therefore, although seemingly congruent, hydrodynamic and thermal slip are only partially related to one another as each factor possesses traits that uniquely affect convective behaviors, depending on simulation constraints. As found within our simulations, in environments where the surface heat flux is much larger than that of advection, thermal slip length is the dominating factor that governs resultant convective behavior at nanoscales. By nondimensionalizing slip lengths with system dimensions (i.e., channel height), size effects are incorporated for assessment into the relationship between $Nu_{D,fd}$ and slip lengths; correlation between $Nu_{D,fd}$ and $l_k/2H$ is found and suggested.

Careful assessment of these analogous microscopic mechanisms enables for accurate description of heat transfer behaviors in system sizes descending into the nanoscale realm. Based on enhanced understandings of the mechanisms influencing and dictating nanoscale convection heat transfer within graphene-liquid water systems, this study pertains to various applications such as micro-sized heat exchangers, electric cooling systems, flow and flow boiling enhancement, primary/secondary reactor cooling loops, etc. Future work should seek to further the correlation between hydrodynamic and thermal slip, and nanoscale convection, in addition to assessment of nanochannel dimensions at which the theoretical $Nu_{D,fd}$ value is obtained for optimal design and convective heat transfer performance. Additional studies should seek to evaluate the effects of graphene wall thickness on convective heat transfer similar to that of a recent study by Alexeev et al. [23]. We anticipate future assessment and validation of reported results through extrapolation of data and provided fit equations via simulation of larger dimensional scales and experiments of sub-micrometer (< 1.0 μm) characteristic length microchannels, similar to the methods and techniques performed by Refs. [6, 148-150].

CHAPTER SIX

CONCLUSIONS

6.1 Summary and Contributions

Momentum and thermal transport within interacting graphene – water systems are explored via utilization of molecular dynamics simulations. Acting as building blocks of fundamental knowledge used to lay the foundation for unraveling nanoscale convective heat transfer phenomena, graphene wettability, flow liquid water behavior and simulated water viscosity, and heat transfer across a graphene – water interface are preliminary investigated. Examinations of graphene wetting properties showcase the influential effects surface interactions have on resultant atom configurations and observable behavior. Initial fluid flow studies both observe and confirm previous findings by exploring deviation from the theorized no-slip boundary condition within nanoscale environments. Moreover, as viscosity is a key fluid property employed in convection studies, simulations of liquid water flow in nanochannels is employed to assess accurate replication of simulated viscosity provided by differing water models. Vital to understanding the transfer of heat within the convective process, interfacial heat transfer is investigated to determine conduction and resistance across graphene – water systems. Employing these preliminary understandings, convective heat transfer of water flow in graphene nanochannels is investigated. It is found that nanoscale behaviors significantly deviate from that hypothesized by macroscale theories as momentum and thermal mechanisms, characterized by hydrodynamic and thermal slip, are amplified by nanoscale interfacial effects. Although resulting conclusions are only as reliable as simulation input parameters, simulation constraints are thoroughly vetted and corroborated with numerous numerical, experimental, and theoretical studies that range in investigated scales from the quantum to macroscale level.

6.2 Possible Extensions

Current work seeks to apply nanochannel convection findings to investigations of the convective heat transfer process within carbon nanotubes (CNTs). Moreover, the study of momentum and thermal transport is not only applicable to thermal management in nanoscale electronic devices; extension to numerous fields of study can also benefit from these types of fundamental investigations. In particular, are the areas of phase change for directional solidification and synthesis of nano- and micro- structures, and desalination. This chapter seeks to detail this student's ongoing and planned work in furthering his exploration into graphene water systems.

6.2.1 Ongoing Work: Convective Heat Transfer in CNTs

Exploring convection heat transfer within carbon nanotubes is one area this student is currently investigating. While previous evaluations of nanoscale convection where more abstract as they sought to understand behaviors with water flow between two infinite parallel plates, this study is expected to yield fundamental insight on heat transfer behaviors when liquid water is fully confined. Moreover, fully confined water, as in the case of CNTs, the conduct of bulk liquid water is indicated to differ from that in nanochannels [20, 50] as CNTs allow for an increased surface area for water to interact with. Therefore, the simulation methodology of convection heat transfer

in nanochannels from Chapter 5 is modified and applied to studies on water flow in CNTs (Fig. 6.1). The parameters of CNT diameter (D), graphene – water interaction strength ($\varepsilon_{C\text{-}O}$), water velocity ($u_{f,x}$), CNT wall temperature (T_w), and other effects are planned for study. Findings are anticipated for publication in the coming months.

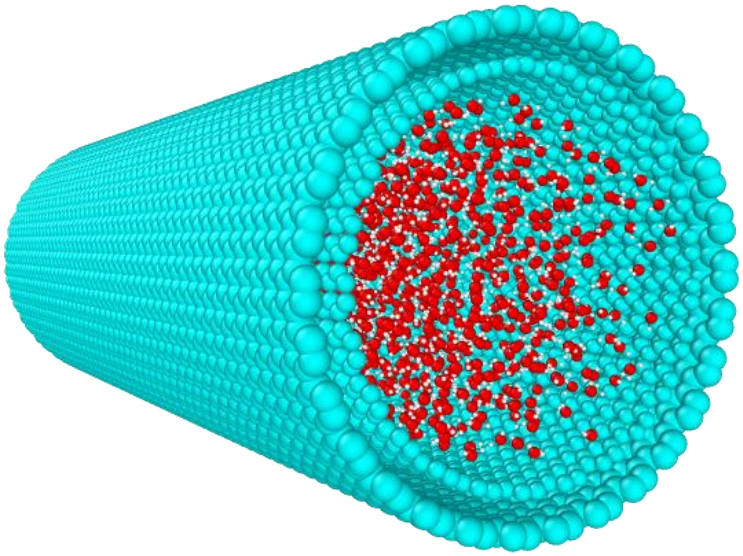


Figure 6.1. Setup of water in a CNT for convection assessment.

6.2.2 Ongoing Work: Phase Change

In this section detailing current work on phase change, the method of Ref. [151] is first investigated to effectively boil water in contact with a graphene sheet (Fig. 6.2). To further investigate phase change behavior, this technique and others are employed to simulate water freezing. The ultimate goal of this work is to uncover a directional freezing mechanisms for nanostructure and graphene aerogel synthesis. Accordingly, graphene flakes are placed in liquid water to study resulting configurations after the freezing process is complete.

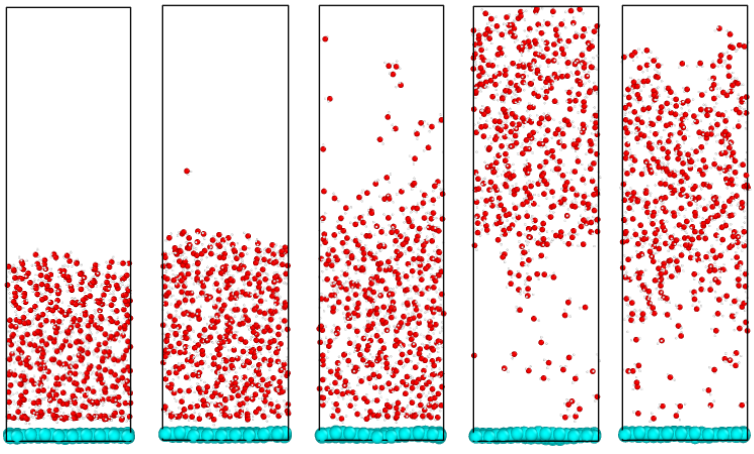


Figure 6.2. Snap shots of water boiling on a heated graphene substrate over a period of time, *t*.

In conjunction with the methodology utilized for boiling and that of Carignano et al. [152], liquid water freezing is investigated. Employing the TIP4P/Ice water model [70] for its ability to more accurately replicate ice melting temperature (T = 272 K), a solutions of graphene flakes in liquid water is then evaluated for its freezing behavior over a period of time, as in Fig. 6.3.

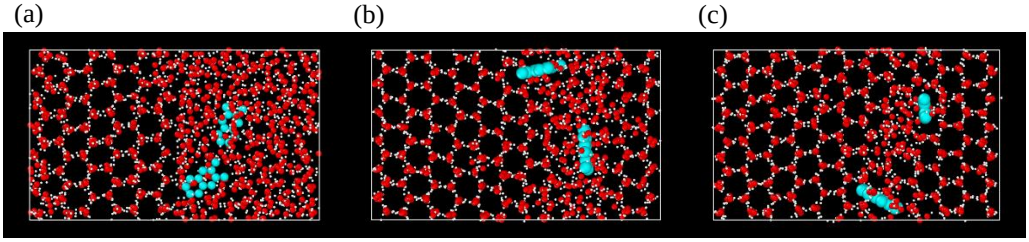


Figure 6.3. Periodic freezing of a graphene flake – water solution over a span of time, *t*.

However, as Figs. 6.3b and 6.3c illustrate, freezing occurs across the periodic image due to the application of PBCs, thus inhibiting exploration of directional freezing. To effectively simulate the process of directional freezing, and to enable for proper volume changes during solidification, systems are modified to account for periodic image effects. Studies on this topic are expected to investigate mechanisms of directional freezing through assessment of freezing temperature, graphene – water attractions, and flake-to-volume ratio.

6.2.3 Future Work: Desalination

Although this is not his current area of investigation, this student plans to explore utilization of graphene nanostructures for the effective desalination of water. This will include the use of nanochannels, nanopores, CNTs, graphene charge, doping, etc., in the graphene structure to effectively separate the Na^+ and Cl^- ions from bulk liquid water. In the shown preliminary investigation (Figs. 6.4a and 6.4b), various layers of charged graphene nanopores are studied to effectively remove and/or sort ions within a salt water solution. Pursuit of these types of studies are planned to take place after investigations of convective heat transfer in carbon nanotubes and directional freezing.

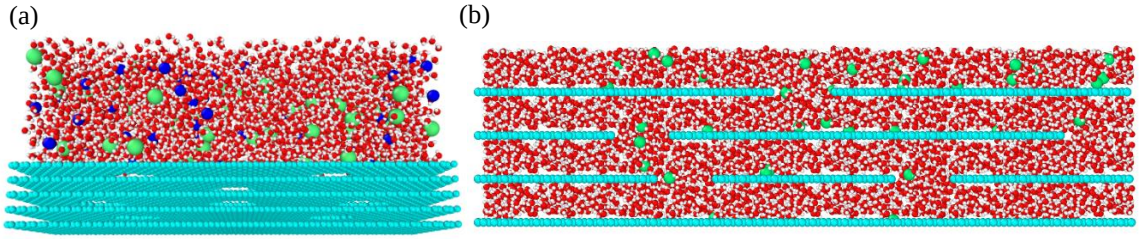


Figure 6.4. (a) Initial setup of salt water solution on top of a porous graphene structure, and (b) ion migration through porous graphene structure.

6.3 Outlook

Though nanoscale MD investigations can at times seem far removed from the macro-, and even micro-, scale realms for functional application purposes, fundamental understandings of nanoscale environments and their interworkings become increasingly vital as both new and old

difficulties arise and persist. With increasing computational abilities, fundamental atomistic endeavors will continue to uncover key principles that dictate and influence observable behaviors at larger scales. Knowing the possibilities MD can provide, this student seeks to contribute to unraveling previously unsolved and undiscovered enigmas that plague advanced manufacturing techniques, novel electronics devices, and even basic humanitarian needs, through his ongoing and future endeavors of investigating CNT convection heat transfer, directional freezing mechanisms, and desalination.

LIST OF REFERENCES

[1] A.L. Moore, L. Shi, Emerging challenges and materials for thermal management of electronics, Materials Today, 17(4) (2014) 163-174.
[2] K.S. Novoselov, A.K. Geim, S.V. Morozov, D. Jiang, Y. Zhang, S.V. Dubonos, I.V. Grigorieva, A.A. Firsov, Electric field effect in atomically thin carbon films, Science, 306(5696) (2004) 666-669.
[3] K. Novoselov, A. Geim, The rise of graphene, Nature Materials, 6 (2007) 183-191.
[4] A.A. Balandin, S. Ghosh, W. Bao, I. Calizo, D. Teweldebrhan, F. Miao, C.N. Lau, Superior thermal conductivity of single-layer graphene, Nano Letters, 8(3) (2008) 902-907.
[5] E. Pop, Energy dissipation and transport in nanoscale devices, Nano Research, 3(3) (2010) 147-169.
[6] J.M.C. Duarte, I.M.A. Contreras, C.R.C. Cely, An optimal high thermal conductive graphite microchannel for electronic devices cooling, Revista Facultad de Ingeniería, (77) (2015) 143-152.
[7] H. Wu, P. Cheng, Friction factors in smooth trapezoidal silicon microchannels with different aspect ratios, International Journal of Heat and Mass Transfer, 46(14) (2003) 2519-2525.
[8] H. Brenner, Beyond the no-slip boundary condition, Physical Review E, 84(4) (2011) 046309.
[9] L. Bocquet, J.-L. Barrat, Flow boundary conditions from nano-to micro-scales, Soft Matter, 3(6) (2007) 685-693.
[10] C. Sendner, D. Horinek, L. Bocquet, R.R. Netz, Interfacial water at hydrophobic and hydrophilic surfaces: Slip, viscosity, and diffusion, Langmuir, 25(18) (2009) 10768-10781.
[11] B.-Y. Cao, J. Sun, M. Chen, Z.-Y. Guo, Molecular momentum transport at fluid-solid interfaces in MEMS/NEMS: a review, International Journal of Molecular Sciences, 10(11) (2009) 4638-4706.
[12] T.A. Ho, D.V. Papavassiliou, L.L. Lee, A. Striolo, Liquid water can slip on a hydrophilic surface, Proceedings of the National Academy of Sciences, 108(39) (2011) 16170-16175.
[13] R.S. Voronov, D.V. Papavassiliou, L.L. Lee, Boundary slip and wetting properties of interfaces: correlation of the contact angle with the slip length, The Journal of Chemical Physics, 124(20) (2006) 204701.
[14] Y.A. Gandomi, M. Edmundson, F. Busby, M.M. Mench, Water Management in Polymer Electrolyte Fuel Cells through Asymmetric Thermal and Mass Transport Engineering of the Micro-Porous Layers, Journal of The Electrochemical Society, 163(8) (2016) F933-F944.
[15] C. Soong, T. Yen, P. Tzeng, Molecular dynamics simulation of nanochannel flows with effects of wall lattice-fluid interactions, Physical Review E, 76(3) (2007) 036303.
[16] S. Ge, Y. Gu, M. Chen, A molecular dynamics simulation on the convective heat transfer in nanochannels, Molecular Physics, 113(7) (2015) 703-710.
[17] B. Ramos-Alvarado, S. Kumar, G.P. Peterson, Solid–Liquid Thermal Transport and Its Relationship with Wettability and the Interfacial Liquid Structure, The Journal of Physical Chemistry Letters, 7(17) (2016) 3497-3501.
[18] B.H. Kim, A. Beskok, T. Cagin, Viscous heating in nanoscale shear driven liquid flows, Microfluidics and Nanofluidics, 9(1) (2010) 31-40.
[19] T.Q. Vo, B. Kim, Transport Phenomena of Water in Molecular Fluidic Channels, Scientific Reports, 6 (2016).
[20] J.A. Thomas, A.J. McGaughey, Reassessing fast water transport through carbon nanotubes, Nano Letters, 8(9) (2008) 2788-2793.

[21] J.A. Thomas, A.J. McGaughey, O. Kuter-Arnebeck, Pressure-driven water flow through carbon nanotubes: insights from molecular dynamics simulation, International Journal of Thermal Sciences, 49(2) (2010) 281-289.
[22] J.-L. Barrat, F. Chiaruttini, Kapitza resistance at the liquid—solid interface, Molecular Physics, 101(11) (2003) 1605-1610.
[23] D. Alexeev, J. Chen, J.H. Walther, K.P. Giapis, P. Angelikopoulos, P. Koumoutsakos, Kapitza resistance between few-layer graphene and water: Liquid layering effects, Nano Letters, 15(9) (2015) 5744-5749.
[24] A.J. Shkarah, M.Y.B. Sulaiman, M.R.B.H. Ayob, H. Togun, A 3D numerical study of heat transfer in a single-phase micro-channel heat sink using graphene, aluminum and silicon as substrates, International Communications in Heat and Mass Transfer, 48 (2013) 108-115.
[25] J.F. Thekkethala, S.P. Sathian, The effect of graphene layers on interfacial thermal resistance in composite nanochannels with flow, Microfluidics and Nanofluidics, 18(4) (2015) 637-648.
[26] H. Ghasemi, C. Ward, Mechanism of sessile water droplet evaporation: kapitza resistance at the solid–liquid interface, The Journal of Physical Chemistry C, 115(43) (2011) 21311-21319.
[27] S. Plimpton, Fast parallel algorithms for short-range molecular dynamics, Journal of Computational Physics, 117(1) (1995) 1-19.
[28] B. Mortazavi, S. Ahzi, Thermal conductivity and tensile response of defective graphene: A molecular dynamics study, Carbon, 63 (2013) 460-470.
[29] L. He, S. Guo, J. Lei, Z. Sha, Z. Liu, The effect of Stone–Thrower–Wales defects on mechanical properties of graphene sheets–A molecular dynamics study, Carbon, 75 (2014) 124-132.
[30] J.-H. Zou, Z.-Q. Ye, B.-Y. Cao, Phonon thermal properties of graphene from molecular dynamics using different potentials, The Journal of Chemical Physics, 145(13) (2016) 134705.
[31] M. Chen, S. Quek, Z. Sha, C. Chiu, Q. Pei, Y. Zhang, Effects of grain size, temperature and strain rate on the mechanical properties of polycrystalline graphene–A molecular dynamics study, Carbon, 85 (2015) 135-146.
[32] A. Markesteijn, R. Hartkamp, S. Luding, J. Westerweel, A comparison of the value of viscosity for several water models using Poiseuille flow in a nano-channel, The Journal of Chemical Physics, 136(13) (2012) 134104.
[33] F. Römer, A. Lervik, F. Bresme, Nonequilibrium molecular dynamics simulations of the thermal conductivity of water: A systematic investigation of the SPC/E and TIP4P/2005 models, The Journal of Chemical Physics, 137(7) (2012) 074503.
[34] F.H. Stillinger, A. Rahman, Improved simulation of liquid water by molecular dynamics, The Journal of Chemical Physics, 60(4) (1974) 1545-1557.
[35] A. Rahman, F.H. Stillinger, Molecular dynamics study of liquid water, The Journal of Chemical Physics, 55(7) (1971) 3336-3359.
[36] T. Werder, J.H. Walther, R. Jaffe, T. Halicioglu, P. Koumoutsakos, On the water− carbon interaction for use in molecular dynamics simulations of graphite and carbon nanotubes, The Journal of Physical Chemistry B, 107(6) (2003) 1345-1352.
[37] G. Scocchi, D. Sergi, C. D'Angelo, A. Ortona, Wetting and contact-line effects for spherical and cylindrical droplets on graphene layers: A comparative molecular-dynamics investigation, Physical Review E, 84(6) (2011) 061602.
[38] T.A. Ho, A. Striolo, Molecular dynamics simulation of the graphene–water interface: comparing water models, Molecular Simulation, 40(14) (2014) 1190-1200.

[39] H. Zhou, P. Ganesh, V. Presser, M.C. Wander, P. Fenter, P.R. Kent, D.-e. Jiang, A.A. Chialvo, J. McDonough, K.L. Shuford, Understanding controls on interfacial wetting at epitaxial graphene: Experiment and theory, Physical Review B, 85(3) (2012) 035406.
[40] M. Matsumoto, S. Saito, I. Ohmine, Molecular dynamics simulation of the ice nucleation and growth process leading to water freezing, Nature, 416(6879) (2002) 409-413.
[41] O.A. Karim, A. Haymet, The ice/water interface: A molecular dynamics simulation study, The Journal of Chemical Physics, 89(11) (1988) 6889-6896.
[42] M.A. Wilson, A. Pohorille, L.R. Pratt, Molecular dynamics of the water liquid-vapor interface, The Journal of physical chemistry, 91(19) (1986) 4873-4878.
[43] R.S. Taylor, L.X. Dang, B.C. Garrett, Molecular dynamics simulations of the liquid/vapor interface of SPC/E water, The Journal of Physical Chemistry, 100(28) (1996) 11720-11725.
[44] F. Taherian, V. Marcon, N.F. van der Vegt, F.d.r. Leroy, What is the contact angle of water on graphene?, Langmuir, 29(5) (2013) 1457-1465.
[45] J. Rafiee, X. Mi, H. Gullapalli, A.V. Thomas, F. Yavari, Y. Shi, P.M. Ajayan, N.A. Koratkar, Wetting transparency of graphene, Nature Materials, 11(3) (2012) 217-222.
[46] J. Rafiee, M.A. Rafiee, Z.Z. Yu, N. Koratkar, Superhydrophobic to superhydrophilic wetting control in graphene films, Advanced Materials, 22(19) (2010) 2151-2154.
[47] J. Zang, S. Ryu, N. Pugno, Q. Wang, Q. Tu, M.J. Buehler, X. Zhao, Multifunctionality and control of the crumpling and unfolding of large-area graphene, Nature Materials, 12(4) (2013) 321-325.
[48] A. Kozbial, Z. Li, C. Conaway, R. McGinley, S. Dhingra, V. Vahdat, F. Zhou, B. D'Urso, H. Liu, L. Li, Study on the surface energy of graphene by contact angle measurements, Langmuir, 30(28) (2014) 8598-8606.
[49] S. Kumar Kannam, B. Todd, J.S. Hansen, P.J. Daivis, Slip length of water on graphene: Limitations of non-equilibrium molecular dynamics simulations, The Journal of Chemical Physics, 136(2) (2012) 024705.
[50] J.A. Thomas, R.M. Iutzi, A.J. McGaughey, Thermal conductivity and phonon transport in empty and water-filled carbon nanotubes, Physical Review B, 81(4) (2010) 045413.
[51] D. Rapaport, The Art of Molecular Dynamics Simulation, The Art of Molecular Dynamics Simulation, by DC Rapaport, pp. 564. ISBN 0521825687. Cambridge, UK: Cambridge University Press, April 2004, (2004) 564.
[52] M. Buehler, Atomistic modeling of materials failure, Springer Science & Business Media, 2008.
[53] A. Rahman, Correlations in the motion of atoms in liquid argon, Physical Review, 136(2A) (1964) A405.
[54] J.E. Jones, On the determination of molecular fields. II. From the equation of state of a gas, in: Proceedings of the Royal Society of London A: Mathematical, Physical and Engineering Sciences, The Royal Society, 1924, pp. 463-477.
[55] W.L. Jorgensen, J. Chandrasekhar, J.D. Madura, R.W. Impey, M.L. Klein, Comparison of simple potential functions for simulating liquid water, The Journal of Chemical Physics, 79(2) (1983) 926-935.
[56] M. Finnis, J. Sinclair, A simple empirical N-body potential for transition metals, Philosophical Magazine A, 50(1) (1984) 45-55.
[57] F.H. Stillinger, T.A. Weber, Computer simulation of local order in condensed phases of silicon, Physical Review B, 31(8) (1985) 5262.

[58] S.J. Stuart, A.B. Tutein, J.A. Harrison, A reactive potential for hydrocarbons with intermolecular interactions, The Journal of Chemical Physics, 112(14) (2000) 6472-6486.
[59] D.W. Brenner, O.A. Shenderova, J.A. Harrison, S.J. Stuart, B. Ni, S.B. Sinnott, A second-generation reactive empirical bond order (REBO) potential energy expression for hydrocarbons, Journal of Physics: Condensed Matter, 14(4) (2002) 783.
[60] D.W. Brenner, Empirical potential for hydrocarbons for use in simulating the chemical vapor deposition of diamond films, Physical Review B, 42(15) (1990) 9458.
[61] J. Tersoff, New empirical model for the structural properties of silicon, Physical Review Letters, 56(6) (1986) 632.
[62] J. Tersoff, New empirical approach for the structure and energy of covalent systems, Physical Review B, 37(12) (1988) 6991.
[63] V. Shenoy, C. Reddy, A. Ramasubramaniam, Y. Zhang, Edge-stress-induced warping of graphene sheets and nanoribbons, Physical Review Letters, 101(24) (2008) 245501.
[64] Z. Xu, M.J. Buehler, Nanoengineering heat transfer performance at carbon nanotube interfaces, ACS Nano, 3(9) (2009) 2767-2775.
[65] L. Verlet, Computer" experiments" on classical fluids. I. Thermodynamical properties of Lennard-Jones molecules, Physical Review, 159(1) (1967) 98.
[66] J. Haile, Molecular dynamics simulation, Wiley, New York, 1992.
[67] L. Martínez, R. Andrade, E.G. Birgin, J.M. Martínez, PACKMOL: a package for building initial configurations for molecular dynamics simulations, Journal of Computational Chemistry, 30(13) (2009) 2157-2164.
[68] H. Berendsen, J. Grigera, T. Straatsma, The missing term in effective pair potentials, Journal of Physical Chemistry, 91(24) (1987) 6269-6271.
[69] J.L. Abascal, C. Vega, A general purpose model for the condensed phases of water: TIP4P/2005, The Journal of Chemical Physics, 123(23) (2005) 234505.
[70] J. Abascal, E. Sanz, R. Garcia Fernandez, C. Vega, A potential model for the study of ices and amorphous water: TIP4P/Ice, The Journal of Chemical Physics, 122(23) (2005) 234511.
[71] J. Medina, R. Prosmiti, P. Villarreal, G. Delgado-Barrio, G. Winter, B. Gonzalez, J. Aleman, C. Collado, Molecular dynamics simulations of rigid and flexible water models: Temperature dependence of viscosity, Chemical Physics, 388(1) (2011) 9-18.
[72] J.-P. Ryckaert, G. Ciccotti, H.J. Berendsen, Numerical integration of the cartesian equations of motion of a system with constraints: molecular dynamics of n-alkanes, Journal of Computational Physics, 23(3) (1977) 327-341.
[73] G. Kamath, S.A. Deshmukh, S.K. Sankaranarayanan, Comparison of select polarizable and non-polarizable water models in predicting solvation dynamics of water confined between MgO slabs, Journal of Physics: Condensed Matter, 25(30) (2013) 305003.
[74] D.R. Cooper, B. D'Anjou, N. Ghattamaneni, B. Harack, M. Hilke, A. Horth, N. Majlis, M. Massicotte, L. Vandsburger, E. Whiteway, Experimental review of graphene, ISRN Condensed Matter Physics, 2012 (2012).
[75] H. Jussila, H. Yang, N. Granqvist, Z. Sun, Surface plasmon resonance for characterization of large-area atomic-layer graphene film, Optica, 3(2) (2016) 151-158.
[76] W. Humphrey, A. Dalke, K. Schulten, VMD: visual molecular dynamics, Journal of Molecular Graphics, 14(1) (1996) 33-38.
[77] L. Girifalco, M. Hodak, R.S. Lee, Carbon nanotubes, buckyballs, ropes, and a universal graphitic potential, Physical Review B, 62(19) (2000) 13104.

[78] M. Gordillo, J. Martı, Hydrogen bond structure of liquid water confined in nanotubes, Chemical Physics Letters, 329(5) (2000) 341-345.
[79] J.C. Bird, R. Dhiman, H.-M. Kwon, K.K. Varanasi, Reducing the contact time of a bouncing drop, Nature, 503(7476) (2013) 385-388.
[80] Y. Zheng, H. Bai, Z. Huang, X. Tian, F.-Q. Nie, Y. Zhao, J. Zhai, L. Jiang, Directional water collection on wetted spider silk, Nature, 463(7281) (2010) 640-643.
[81] Y. Yang, P.-p. Wang, Z.-c. Zhang, H.-l. Liu, J. Zhang, J. Zhuang, X. Wang, Nanowire membrane-based nanothermite: towards processable and tunable interfacial diffusion for solid state reactions, Scientific Reports, 3 (2013).
[82] R. Chen, M.-C. Lu, V. Srinivasan, Z. Wang, H.H. Cho, A. Majumdar, Nanowires for enhanced boiling heat transfer, Nano Letters, 9(2) (2009) 548-553.
[83] C. Ye, M. Li, J. Hu, Q. Cheng, L. Jiang, Y. Song, Highly reflective superhydrophobic white coating inspired by poplar leaf hairs toward an effective "cool roof", Energy & Environmental Science, 4(9) (2011) 3364-3367.
[84] R. Blossey, Self-cleaning surfaces—virtual realities, Nature Materials, 2(5) (2003) 301-306.
[85] L. Cao, A.K. Jones, V.K. Sikka, J. Wu, D. Gao, Anti-icing superhydrophobic coatings, Langmuir, 25(21) (2009) 12444-12448.
[86] T. Soldo, T. Hofmann, Application of hydrophilic interaction liquid chromatography/comparative taste dilution analysis for identification of a bitter inhibitor by a combinatorial approach based on Maillard reaction chemistry, Journal of Agricultural and Food Chemistry, 53(23) (2005) 9165-9171.
[87] T. Bharathidasan, S.V. Kumar, M. Bobji, R. Chakradhar, B.J. Basu, Effect of wettability and surface roughness on ice-adhesion strength of hydrophilic, hydrophobic and superhydrophobic surfaces, Applied Surface Science, 314 (2014) 241-250.
[88] Z. Li, Y. Wang, A. Kozbial, G. Shenoy, F. Zhou, R. McGinley, P. Ireland, B. Morganstein, A. Kunkel, S.P. Surwade, Effect of airborne contaminants on the wettability of supported graphene and graphite, Nature Materials, 12(10) (2013) 925-931.
[89] B. Ramos-Alvarado, S. Kumar, G. Peterson, Wettability of graphitic-carbon and silicon surfaces: MD modeling and theoretical analysis, The Journal of Chemical Physics, 143(4) (2015) 044703.
[90] B. Ramos-Alvarado, S. Kumar, G. Peterson, Hydrodynamic slip length as a surface property, Physical Review E, 93(2) (2016) 023101.
[91] S.Y. Daisy, An Efficient Algorithm for Contact Angle Estimation in Molecular Dynamics Simulations, International Journal of Engineering, 9(1) 1 - 8.
[92] E.E. Santiso, C. Herdes, E.A. Müller, On the calculation of solid-fluid contact angles from molecular dynamics, Entropy, 15(9) (2013) 3734-3745.
[93] Z. Zhang, H. Zhang, H. Ye, Pressure-driven flow in parallel-plate nanochannels, Applied Physics Letters, 95(15) (2009) 154101.
[94] S.K. Kannam, B. Todd, J.S. Hansen, P.J. Daivis, Slip flow in graphene nanochannels, The Journal of Chemical Physics, 135(14) (2011) 016313.
[95] D.C. Marable, S. Shin, A. Yousefzadi Nobakht, Investigation into the microscopic mechanisms influencing convective heat transfer of water flow in graphene nanochannels, International Journal of Heat and Mass Transfer, 109(28 - 39) (2017).

[96] M.S. Green, Markoff random processes and the statistical mechanics of time-dependent phenomena. II. Irreversible processes in fluids, The Journal of Chemical Physics, 22(3) (1954) 398-413.
[97] R. Kubo, Statistical-mechanical theory of irreversible processes. I. General theory and simple applications to magnetic and conduction problems, Journal of the Physical Society of Japan, 12(6) (1957) 570-586.
[98] A. Einstein, Investigations on the Theory of the Brownian Movement, Courier Corporation, 1956.
[99] J. Koplik, J.R. Banavar, J.F. Willemsen, Molecular dynamics of Poiseuille flow and moving contact lines, Physical Review Letters, 60(13) (1988) 1282.
[100] M. Barisik, A. Beskok, Wetting characterisation of silicon (1, 0, 0) surface, Molecular Simulation, 39(9) (2013) 700-709.
[101] R. Bird, W. Stewart, E. Lightfoot, Transport Phenomena 2nd edition John Wiley and Sons, New York, (2002).
[102] X.-Q. Wang, A.S. Mujumdar, Heat transfer characteristics of nanofluids: a review, International Journal of Thermal Sciences, 46(1) (2007) 1-19.
[103] J. Chen, J.H. Walther, P. Koumoutsakos, Strain engineering of Kapitza resistance in few-layer graphene, Nano Letters, 14(2) (2014) 819-825.
[104] M. Moulod, G. Hwang, Water self-diffusivity confined in graphene nanogap using molecular dynamics simulations, Journal of Applied Physics, 120(19) (2016) 194302.
[105] D.B. Tuckerman, R. Pease, High-performance heat sinking for VLSI, IEEE Electron Device Letters, 2(5) (1981) 126-129.
[106] X. Peng, B. Wang, G. Peterson, H. Ma, Experimental investigation of heat transfer in flat plates with rectangular microchannels, International Journal of Heat and Mass Transfer, 38(1) (1995) 127-137.
[107] S. Ghosh, I. Calizo, D. Teweldebrhan, E.P. Pokatilov, D.L. Nika, A.A. Balandin, W. Bao, F. Miao, C.N. Lau, Extremely high thermal conductivity of graphene: Prospects for thermal management applications in nanoelectronic circuits, Applied Physics Letters, 92(15) (2008) 151911.
[108] G.G. Stokes, On the effect of the internal friction of fluids on the motion of pendulums, Transactions of the Cambridge Philosophical Society, 9 (1851) 8-106.
[109] S.-C. Yang, Effects of surface roughness and interface wettability on nanoscale flow in a nanochannel, Microfluidics and Nanofluidics, 2(6) (2006) 501-511.
[110] B.-Y. Cao, M. Chen, Z.-Y. Guo, Liquid flow in surface-nanostructured channels studied by molecular dynamics simulation, Physical Review E, 74(6) (2006) 066311.
[111] W. Qu, G.M. Mala, D. Li, Heat transfer for water flow in trapezoidal silicon microchannels, International Journal of Heat and Mass Transfer, 43(21) (2000) 3925-3936.
[112] C. Bakli, S. Chakraborty, Slippery to sticky transition of hydrophobic nanochannels, Nano Letters, 15(11) (2015) 7497-7502.
[113] J. Towns, T. Cockerill, M. Dahan, I. Foster, K. Gaither, A. Grimshaw, V. Hazlewood, S. Lathrop, D. Lifka, G.D. Peterson, XSEDE: accelerating scientific discovery, Computing in Science & Engineering, 16(5) (2014) 62-74.
[114] C. Vega, J.L. Abascal, Simulating water with rigid non-polarizable models: a general perspective, Physical Chemistry Chemical Physics, 13(44) (2011) 19663-19688.

[115] G. Cicero, J.C. Grossman, E. Schwegler, F. Gygi, G. Galli, Water confined in nanotubes and between graphene sheets: A first principle study, Journal of the American Chemical Society, 130(6) (2008) 1871-1878.
[116] J. Marti, J. Sala, E. Guardia, Molecular dynamics simulations of water confined in graphene nanochannels: From ambient to supercritical environments, Journal of Molecular Liquids, 153(1) (2010) 72-78.
[117] R. Raj, S.C. Maroo, E.N. Wang, Wettability of graphene, Nano Letters, 13(4) (2013) 1509-1515.
[118] R.W. Hockney, J.W. Eastwood, Computer simulation using particles, CRC Press, 1988.
[119] E. Spohr, Effect of electrostatic boundary conditions and system size on the interfacial properties of water and aqueous solutions, The Journal of Chemical Physics, 107(16) (1997) 6342-6348.
[120] Y. Mao, Y. Zhang, Thermal conductivity, shear viscosity and specific heat of rigid water models, Chemical Physics Letters, 542 (2012) 37-41.
[121] P. Linstrom, W. Mallard, National institute of standards and technology (NIST) chemistry webbook, NIST Standard Reference Database, (2005).
[122] R.F. Probstein, Physicochemical hydrodynamics: an introduction, John Wiley & Sons, 2005.
[123] K.V. Sharp, R.J. Adrian, J.G. Santiago, J.I. Molho, The MEMS Handbook, CRC, New York, (2002) 1-33.
[124] S.G. Kandlikar, Heat Transfer and Fluid Flow in Minichannels and Microchannels, Elsevier, 2006.
[125] M. Gad-el-Hak, Differences between liquid and gas transport at the microscale, Technical Sciences, 53(4) (2005).
[126] K.P. Travis, B. Todd, D.J. Evans, Departure from Navier-Stokes hydrodynamics in confined liquids, Physical Review E, 55(4) (1997) 4288.
[127] X.-B. Mi, A.T. Chwang, Molecular dynamics simulations of nanochannel flows at low Reynolds numbers, Molecules, 8(1) (2003) 193-206.
[128] K.P. Travis, K.E. Gubbins, Poiseuille flow of Lennard-Jones fluids in narrow slit pores, The Journal of Chemical Physics, 112(4) (2000) 1984-1994.
[129] J. Lahjomri, A. Oubarra, Analytical solution of the Graetz problem with axial conduction, Journal of Heat Transfer, 121(4) (1999) 1078-1083.
[130] Y. Haddout, J. Lahjomri, The extended Graetz problem for a gaseous slip flow in micropipe and parallel-plate microchannel with heating section of finite length: Effects of axial conduction, viscous dissipation and pressure work, International Journal of Heat and Mass Transfer, 80 (2015) 673-687.
[131] A. Markvoort, P. Hilbers, S. Nedea, Molecular dynamics study of the influence of wall-gas interactions on heat flow in nanochannels, Physical Review E, 71(6) (2005) 066702.
[132] S. Nosé, A molecular dynamics method for simulations in the canonical ensemble, Molecular Physics, 52(2) (1984) 255-268.
[133] W.G. Hoover, Canonical dynamics: equilibrium phase-space distributions, Physical Review A, 31(3) (1985) 1695.
[134] T. Schneider, E. Stoll, Dynamics of the Sine-Gordon Chain, Physical Review Letters, 41(21) (1978) 1429.

[135] R. Khare, P. Keblinski, A. Yethiraj, Molecular dynamics simulations of heat and momentum transfer at a solid–fluid interface: relationship between thermal and velocity slip, International Journal of Heat and Mass Transfer, 49(19) (2006) 3401-3407.
[136] R. Shah, A. London, Laminar Flow Forced Convection in Ducts, Academic Press, New York, 1978.
[137] T.L. Bergman, F.P. Incropera, D.P. DeWitt, A.S. Lavine, Fundamentals of heat and mass transfer, John Wiley & Sons, 2011.
[138] Y.-W. Gu, S. Ge, M. Chen, A molecular dynamics simulation of nanoscale convective heat transfer with the effect of axial heat conduction, Molecular Physics, 114(12) (2016) 1922-1930.
[139] S. Shin, M. Kaviany, T. Desai, R. Bonner, Roles of atomic restructuring in interfacial phonon transport, Physical Review B, 82(8) (2010) 081302.
[140] P.A. Thompson, S.M. Troian, A general boundary condition for liquid flow at solid surfaces, Nature, 389(6649) (1997) 360-362.
[141] T.Q. Vo, B. Kim, Interface thermal resistance between liquid water and various metallic surfaces, International Journal of Precision Engineering and Manufacturing, 16(7) (2015) 1341-1346.
[142] L. Xue, P. Keblinski, S. Phillpot, S.-S. Choi, J. Eastman, Two regimes of thermal resistance at a liquid–solid interface, The Journal of Chemical Physics, 118(1) (2003) 337-339.
[143] X. Yang, Z.C. Zheng, Effects of channel scale on slip length of flow in micro/nanochannels, Journal of Fluids Engineering, 132(6) (2010) 061201.
[144] A. Martini, H.-Y. Hsu, N.A. Patankar, S. Lichter, Slip at high shear rates, Physical Review Letters, 100(20) (2008) 206001.
[145] A.A. Pahlavan, J.B. Freund, Effect of solid properties on slip at a fluid-solid interface, Physical Review E, 83(2) (2011) 021602.
[146] M. Barisik, A. Beskok, Temperature dependence of thermal resistance at the water/silicon interface, International Journal of Thermal Sciences, 77 (2014) 47-54.
[147] V.V. Chaban, O.V. Prezhdo, Water boiling inside carbon nanotubes: toward efficient drug release, ACS Nano, 5(7) (2011) 5647-5655.
[148] S.-S. Hsieh, C.-Y. Lin, Convective heat transfer in liquid microchannels with hydrophobic and hydrophilic surfaces, International Journal of Heat and Mass Transfer, 52(1) (2009) 260-270.
[149] B. Kim, An experimental study on fully developed laminar flow and heat transfer in rectangular microchannels, International Journal of Heat and Fluid Flow, 62 (2016) 224-232.
[150] I. Silvestre, A.W. Barnard, S.P. Roberts, P.L. McEuen, R.G. Lacerda, Folded graphene nanochannels via pulsed patterning of graphene, Applied Physics Letters, 106(15) (2015) 153105.
[151] Y. Mao, Y. Zhang, Molecular dynamics simulation on rapid boiling of water on a hot copper plate, Applied Thermal Engineering, 62(2) (2014) 607-612.
[152] M. Carignano, E. Baskaran, P. Shepson, I. Szleifer, Molecular dynamics simulation of ice growth from supercooled pure water and from salt solution, Annals of Glaciology, 44(1) (2006) 113-117.
[153] A. Stukowski, Visualization and analysis of atomistic simulation data with OVITO–the Open Visualization Tool, Modelling and Simulation in Materials Science and Engineering, 18(1) (2009) 015012.
[154] Excel, Microsoft Corporation, Redmond, WA.
[155] Origin, OriginLab, Northampton, MA.
[156] MATLAB and Statistics Toolbox Release 2015a, The MathWorks Inc., Natick, MA.

APPENDIX

LAMMPS

The Large-scale Atomic/Molecularly Massive Parallel Simulator [27] (LAMMPS, December 7, 2015 version) is exclusively employed for classical molecular dynamics simulations in the scope of this thesis' investigations. Developed by Sandia National Laboratories, LAMMPS is an open source software written in C++ and is the foremost software used to conduct investigative MD simulations through its implementation of MD algorithm methods presented in Chapter 2.

LAMMPS software relies upon two main input files: 1) A data file containing simulation domain specifications, atom types, coordinates, masses, and charges, molecule definitions, bonds, angles, and dihedral and improper quadruplets, and 2) an input file detailing initiation procedures, defined settings, and simulation execution commands.

Simulation Setup and Pre-Processing

Data File

As described in Chapter 2, the VMD outputted data file of the desired graphene – water system fabricated with the use of Packmol is employed for the initial atom configurations within LAMMPS simulations. This file specifies the number of atoms, bonds, and angles, and their respective "types" for atom/molecule identification. Additionally, atom masses and the length, width and height of the simulation box boundaries in the *x*-, *y*- and *z*- axis dimensions are also defined. Atom and molecule type, charge, and coordinates in the specified 3D space of the simulation box are also defined. This is followed by angle and bond details that ensure proper formation and interconnecting of atoms within molecules. The definition of dihedral and improper quadruplets were not employed as they are unneeded within the scope of this thesis.

Input File: Initialization

LAMMPS requires initialization commands in order to define and implement proper simulation conditions for a successful run. These commands are as follows: units, dimension, boundary, atom, bond and angle style, and Newton.

units: The "units" command identifies the type of units employed for MD simulations; the selected type sets the units of all input and output values. These can be set to lj, real, metal, si, cgs, electron, micro or nano, and each specifies differing unit systems. For the purposes of this thesis, the unit system "metal" is employed; this is due to the AIREBO and Tersoff potential files used for graphene description being specifically parameterized for use with "metal" units (please note that reported value units have been converted for presentation with energy units of kJ/mol as this unit is more commonly used within this field of study). "Metal" units are specified as the following: mass = grams/mole, distance = Angstroms, time = picoseconds, energy = eV, velocity = Angstroms/picosecond, force = eV/Angstrom, torque = eV, temperature = Kelvin, pressure = bars, dynamic viscosity = Poise, charge = multiple of electron charge (1.0 is a proton), dipole = charge*Angstroms, electric field = volts/Angstrom, and density = gram/cm$^{\text{dimension}}$.

dimension: The "dimension" command specifies the simulation systems dimensionality and in every investigation simulation, this is set as "3".

boundary: The "boundary" command sets the simulation domain boundary conditions. Set as either periodic (p), non-periodic and fixed (f), non-periodic and shrink-wrapped (s) or non-periodic and shrink-wrapped with a minimum value (m), this allows for specification of simulation box periodicity. Depending on the investigated case, simulations are either conducted with the boundary set as "p p p", specifying periodic boundaries in all three dimensions, or as "p p f" that defines the *x*- and *y*- axis directions as periodic but fixing the *z*-axis direction as non-periodic (boundary conditions will be specified for each investigation in this thesis). A periodic boundary allows for particles to exit one end of the simulation box by crossing the defined boundary and re-enter at the opposite end of the simulation cell. Conversely, when a particle crosses a fixed boundary and moves outside of the simulation domain, the particle will be deleted. Although the "p p f" boundary definition is not ideal for many other studies as it leads to deleted particles, this specification can be coupled with other LAMMPS methods to significantly enhance computational efficiency; specified use of boundary conditions is detailed in each investigation.

atom_style; **bond_style**; **bond_coeff**; **angle_style**; **angle_coeff**: The "atom_style", "bond_style", and "angle_style" determine what parameters are read from the data file and stored by each atom definition. For the purposes of this thesis, the atom style "full", bond style "harmonic", and angle style "harmonic" are selected. The atom style "full" command is selected to define molecules and charges, and signals for the input file to read bond and angles from the data file. In reading these bonds and angles, water molecule bond and angle styles are selected as "harmonic" so to keep equilibrium bond and angle distance/position for the modeling of bond and angle vibrations. Moreover, and although these commands are primarily employed in conjunction with force field specification, the "bond_coeff" and "angle_coeff" further atom/molecule behavioral description with the arguments of "N, K_{bond}, r_0" and "N, K_{angle}, angle", respectively; these are only defined for water molecules as graphene bonds and angles are determined by the earlier discussed AIREBO potential file. N corresponds to the bond/angle number for identification, K_{bond} and K_{angle} are the force energies of the respective O-H bond and H-O-H angle for flexible water molecules, r_0 is the O-H bond length, and angle is the H-O-H angle. With values taken from the previously discussed literature on water models, the arguments for "bond_coeff" are "1" "0.0" (eV/Å^2) and "0.9572" (Å), and the "angle_coeff" arguments are "1" "0.0" (eV/Å^2) and "104.52" (°); K_{bond} and K_{angle} are set to zero as this thesis employs the use of the SHAKE [72] algorithm (later discussed) to model rigid bonds and angles.

Newton: Lastly the command "Newton" determines whether or not to include Newton's 3rd law for pairwise and bonded interactions. As all simulations employ potential models that require this, the command "Newton" is set to "on".

Input File: Atom Definition

read_data: "Read_data", combined with the data file name as an argument, is the command used to signal for the input file to read the atom coordinates, masses, charge, topology information, etc. provided by the data file. LAAMPS uses this data for further processing and simulation.

group; **region**: In complex molecular systems with more than one type of molecule or atom, the commands "group" and "region" are used to define specific sets of atoms with the assignment of a group ID or region ID. Within the usage of the "group" command, atoms can be classified based

on their atom number, type, molecule assignment, etc., and are assigned a group ID; these atoms stay in their assigned group unless a "delete group" command is implemented. Conversely, the "region" command enables for the definition of set regions to allow for atoms to be selected based on their position, rather than atom classification. Moreover, these regions can be converted to a fixed "group" (as previously described), or to a "dynamic group" that allows for selective atom grouping based on their current location; these dynamic groupings can be updated periodically to include or not include atoms at a specific time iteration throughout the simulation duration. These group/region IDs are what is used by the later described commands of "velocity", "fix", "compute", "dump", etc., to prescribe various conditions and implementation methods.

Input File: Simulation Settings

timestep: Vital to most all MD simulation (LAMMPS) procedures is the usage of the "timestep" command; choosing an inadequate timestep (prescribed in the chosen time units) value can cause highly unstable simulation environments or yield insufficient sampling times to collect data. Too large of a timestep can produce conditions where atoms become missing from moving too far and too fast for the various algorithms to keep track of; conversely, specifying too small of a timestep value can yield insufficient access to system evolution characteristics and result in unneeded computational efforts. A time step of "0.001" (ps, or 1.0 fs) is typically chosen to avoid discretization errors as well as allow for sufficient system development within the simulation duration; however, some cases employ timesteps of 1.5 fs and 2.0 fs, and are specified.

neighbor; **neigh_modify**: Within MD simulations, particles and interactions need to be tracked for accurate and efficient computations; to do this, the "neighbor" and "neigh_modify" commands are used to affect the building of pairwise neighbor lists. All atom pairs within a neighbor cutoff distance equal to their force cutoff plus the skin distance are stored in the MD simulation neighbor list, where the skin distance determines how often atoms migrate to new processors. The "bin" style is chosen as the algorithm used to build these lists in all investigations; this style constructs neighbor lists by binning as an operation that linearly scales with N/P, where N is the total number of atoms and P is the number of processors. To effectively avoid dangerous neighbor list builds, the skin distance is set as the recommended value of "2.0" (Å). Moreover, to further avoid problems with neighbor list builds, the arguments for the "neigh_modify" command are specified as "every 1 delay 0 check yes" to instruct the MD algorithm to build neighbor lists on every iterative step if any one atom has moved more than half the skin distance since the last list build.

Input File: Force Field Specifications

As outlined in Chapter 2, force calculations are of vital importance to accurate and realistic results and behaviors. These types of specification commands primarily govern interactions between simulated atoms and are the primary users of computational time and resources with LAMMPS simulations.

pair_style; **pair_coeff**: The "pair_style" and "pair_coeff" commands are employed in the determination of pairwise interactions. Pair potentials, defined between atom pairs within a cutoff distance, are employed as the arguments for these commands. The "pair_style" command sets the formulas employed by LAAMPS to compute pairwise interactions. As a combination of models are employed within complex graphene – water systems, the "pair_style" command is chosen as

"hybrid" for all investigations; this allows for the setup of specified atom-type pairs to interact via differing pair potentials. Within investigations employing the TIP4P water model iterations and the 2nd generation Tersoff Brenner graphene potential, the "pair_style" is set as "hybrid lj/cut/tip4p/long 'otype' 'htype' 'btype' 'atype' 'qdist' 'cutoff' lj/cut 'cutoff' rebo". In this statement defining a hybrid pair style system, the Lennard Jones terms describe long-range interactions [55] while the REBO term describes short-ranged C-C interactions within the graphene sheet. To model inter- and intra- molecular interactions for water molecules, the "lj/cut/tip4p/long" term specifies arguments of which atom types to model as water (otype, htype), their bond and angle types (btype, atype), the distance from the oxygen atom to the massless charge (qdist), and their global cutoff for LJ interactions (cutoff). Moreover, the "lj/cut" term is also employed the determine long-range interactions between graphene and water, and between the intra-layer C-C interactions of the graphene sheet. The short-ranged inter-layer C-C interactions within a graphene sheet are defined with the "rebo" term; its potential formulation (provided by its described below "pair_coeff" argument) specifies this cutoff to be set as the default "2" (Å).

In conjunction with setting the computing formulas by the "pair_style" command, the "pair_coeff" command further specifies the pairwise force field coefficients for the various pairs of atom types. For the long-range atom interactions earlier described, the "pair_coeff" has the arguments: 'I' 'J' 'style' 'ε_{IJ}' 'σ_{IJ}'; these correspond to setting the coefficients for interaction between atom type 'I' and type 'J', followed by their interaction style (or formula as either "lj/cut/tip4p/long" or "lj/cut", within the scope of this thesis), and their defined interaction energy strength (ε_{IJ}) and corresponding distance at which their potential energy is zero (σ_{IJ}). The "pair_coeff" arguments for the short-range C-C interactions within a graphene sheet are defined by calling the location of the AIREBO potential file. As described in Chapter 2, REBO is essentially the same as AIREBO with the exception of a few spline fitting procedures that only describes short-ranged C-C interactions. As such, the defining arguments of "I, J, style, filename, N element names", where (for the purposes of this thesis) I and J are the carbon atom types, the style is specified as "rebo", the calling command that locates the AIREBO potential file for C-C description, and the mapping of AIREBO elements to simulation atom types. This file contains the necessary information to parameterize graphene sheet inter-layer C-C interactions; interaction parameters employed within the scope of this thesis are found in Table 2.1.

kspace; **kspace_modify**; **slab**: The "kspace" command dictates which solver to use to compute long-range Coulombic interactions; the particle-particle particle-mesh solver (PPPM) [118] is primarily employed for these types of calculations. Using Poisson's equation to solve Coulombic interactions, the PPPM technique maps atom charge to a 3D mesh and then interpolates electric fields. When simulating a TIP4P-iteration water model, the PPPM method is corrected as "pppm/tip4p" to account for the massless site incorporated within each water molecule.

Essential to simulations conducted in this thesis, the simulation kspace can be modified with the "kspace_modify" command and specifying the "slab" option [119] with arguments stating a volume factor. Since the PPPM solver requires periodic dimensions ("p p p"), this slab option allows for the PPPM solver to be employed in systems that are periodic in the *x*- and *y*- axis directions, but non-periodic in the *z*-axis direction via specification of "p p f" boundaries; essentially, the system is treated as if it were periodic in the *z*-axis direction to allow for PPPM computations. In doing this, the slab option inserts an empty volume extending along the *z*-axis corresponding to the set volume factor value (3.0 is used as recommended), and adds an

electrostatic correction layer above and below (± *z* direction) the simulation domain to prevent *z*-axis Coulombic computations; thus, interactions across the *z*-axis boundary are effectively removed.

Input File: Fix Options

Commands employed with the "fix" and/or "fix_modify" prefix are used in a variety of different ways to set simulation constraints, and calculate global, per-atom, and local values for outputted data collection. The "fix_modify" command simply helps to better define on what atoms (or group, region, etc.) the fix should be applied and how values are determined.

shake: As previously mentioned, the SHAKE [72] algorithm is employed to apply bond and angle constraints to those specified for water molecules, while the bonds and angles of graphene are modeled with the AIREBO potential. Implemented as "fix, ID, group-ID, style, tol, iter, N, b, a, t, m", this fix defines the fix ID, group on which to impose the fix, the fix style (i.e., shake), accuracy tolerance of the SHAKE solution, the maximum number of iterations in each SHAKE solution, printing of SHAKE statistics at every N timesteps, bond type, angle type, atom type, mass values". In all simulations, this is specified as: "fix", "fix-ID" (user specified name), "group" (for water), "shake", "1e-4", "100", "0", "b", "1", "a", "1"; the arguments of "t" and "m" did not require specification within these investigations.

velocity; **NVT**; **NPT**; **NVE**; **Langevin**: As methods for prescribing simulation ensembles and thermostats, the following described "fix" options and methods are central to determining simulation environment conditions and are essential for realistic representations of atom behaviors and accurate data acquisition. In this thesis, the employed "fix" options will vary based on investigational needs and computational efficiency, and are further identified for their use in each chapter.

The command "velocity", coupled with its "create" style, generates an ensemble of velocities at a specified temperature through the use of a random number generation seeding input. The ensemble of velocities is generated to create a "Gaussian" distribution with a mean of 0.0 and a scaled sigma value to produce the desired temperature. Moreover, it should be noted that this is not the global simulation "ensemble" for statically sampling data (as described below); this is employed to speed up the initial system equilibration processes before data collection.

LAMMPS employs a variety of different fix options to perform time integration for generating positions and velocities for data sampling. In particular, this thesis utilizes the fix "*NVT*", "*NPT*", and "*NVE*" terms to specify the simulation ensemble used for integrating and updating atom positions and velocities. Although conceptually similar, these three fix options greatly differ as they can employ thermostating and/or barostating, or be used in conjunction with outside thermostat/barostat methods.

The fix "*NVT*" (constant number of particle, volume, and temperature) command, corresponding to the canonical ensemble, performs time integration on Nose-Hoover style non-Hamiltonian equations of motions to update atom positions and velocities every timestep for data collection. Intrinsic to this command is the use of Nose-Hoover [132, 133] thermostating with the "temp" setting, which applies thermostating methods only to particles' translational degrees of freedom within a specified group. Within this fix, atom velocity/positions are updated to relax temperature to its desired value, as specified by the "temp" (temperature units, K) command.

Similar to fix "*NVT*" is the "*NPT*" (constant number of particles, pressure, and temperature) command, which corresponds to the isothermal-isobaric ensemble. This ensemble performs Nose-Hoover thermostating and barostating to the simulation domain by adding dynamic variables that are coupled to particle velocities (thermostating) and the simulation volume dimensions (barostating). In addition to setting the desired "temp", a "press" (pressure units, bars) value is also identified as the desired pressure; this can be specified for the entire simulation domain or only a specific group of atoms.

The fix "*NVE*" (constant number of particles, volume, and energy) command, corresponding to the microcanonical ensemble, does not include intrinsic thermostating or barostating methods like those found in the fix "*NVT*" and "*NPT*" commands. However, it is similar in that atom positions and velocities are updated within a specified group; this can be particularly useful within system equilibration, and more importantly within setting specific environmental conditions of complex interacting systems. "*NVE*" possesses the unique ability to set the entire simulation domain as the microcanonical ensemble, and employ external thermostating and barostating fixes to differing groups of atoms or regions (or the global volume) while others are left unaffected. Based on investigative needs, the fix options of "temp/rescale", "temp/berendsen", "langevin", "press/berendsen", etc., can be coupled with "*NVE*" usage as external thermostating or barostating methods to achieve/maintain a desired temperature and/or pressure by means of employing various forms of dynamical models/formulas. Within the scope of this thesis, only the fixing option "langevin" is employed for coupling with instances of "*NVE*" usage; these instances are identified in each chapter. Langevin [134] thermostats (e.g., fix "langevin") employ Brownian dynamics to modify forces acting on each atom; this effectively performs/effects thermostating to a desired temperature. However, as solely a thermostating method, fix "langevin" requires the use of "*NVE*" to perform time integration for updating positions and velocities.

spring/self: The "spring/self" fix command applies a spring force to each independent atom in a group to tether it to its initial position. Employed as "fix, fix-ID (user defined name), group (spring-applied group), spring/self, K (eV/Å), dir (xyz, or any direction combination), this command is used to tether the outer-most graphene wall layers into position to keep dimensions set in place. The spring constant magnitude, K, varies with the number of carbon atoms in a graphene wall and will be specified in each instance of use; "dir" is left as its default argument of "xyz", allowing atoms to be tethered in the *x*-, *y*-, and *z*- axis directions.

addforce: The fix command "addforce" does precisely what its name implies, which is that it adds a force. Within the use of this command, a user-defined amount of force is applied at each timestep to each atom in a particular group; this force is exerted on all or any combination of an atom's *x*-, *y*-, and *z*- axis force components. Employed as "fix, fix-ID (user defined name), group (force-applied group), addforce, f_x (eV/Å), f_y (eV/Å), f_z (eV/Å)", this fix command is exclusively used to apply a flow-driving force within investigations of Poiseuille flow and convection heat transfer. Force magnitudes vary depending on the number of water molecules in a simulation and are specified in each investigation employing this "addforce" command; however, in all cases, forces are only applied in the *x*-axis (f_x) direction, with f_y and f_z specified as "NULL".

ave/time; **ave/spatial**: Defined as "fix" commands to time- or spatially- average global or group-specific values of interest over long periods of time, these fixes are primarily employed to output resultant heat flux, velocity, and temperature data. Data is averaged every specified N number of timesteps and printed at set time intervals (as in the case of "ave/time"); "ave/spatial" furthers this to print spatially averaged values in a specific region in 3D space (areas of interest are defined by specifying *x*-, *y*-, and *z*- axis dimensions). Utilization of these fixes allow for enhanced detailing of atomic behavior for data processing and analysis.

Input File: Compute Commands

temp: The "compute temp" command is used to identify temperatures of specific atom groups and regions for more in-depth data processing and understanding of atomistic behaviors. Although the global temperature of the simulation domain is computed and printed (as later described in the section detailing LAMMPS output options), this is employed provide outputted temperature data on particular groupings and/or regions (e.g., thermostated graphene walls).

ke/atom; **pe/atom**; **stress/atom**; **heat/flux**: The commands of compute "ke/atom", "pe/atom", and "stress/atom" calculate kinetic energy per atom (eV), potential energy per atom (eV), and the amount of stress per atom (bars*$Å^3$), respectively; these can be determined for the global simulation domain or only a specified atom grouping. More importantly, these three terms compute terms are employed as arguments for the compute "heat/flux" command; set as "compute, compute-ID (user defined name), group (compute group), heat/flux, ke-ID, pe-ID, stress-ID", this measures the amount of heat flux into or out of an atom reservoir. This is extensively used within this thesis' heat transfer investigations. Although this compute is typically employed within Green-Kubo methods for thermal conductivity calculations, this thesis utilizes compute "heat/flux" to directly print heat flux data to outputted files for post-processing.

Input File: Output Options

thermo; **thermo_style**: The "thermo" command is used in conjunction with "thermo_style" to print/output calculated data. Formatting of "thermo_style" as "custom", allows the user to manually specify desired information for printing to the log file; data can include global simulation data of: "step", "temp", "press", "ke", "pe", "etot", "volume", "dens", etc., in addition to other specifically computed data as detailed in previous sections (i.e., computed temperature, pressure, kinetic energy, potential, energy, etc.). Moreover, this data is periodically printed to the log file every N time steps as defined in the "thermo" command.

dump: From implementation of the "dump" command, LAMMPS can output snapshots of atomic trajectories (i.e., positions/configurations) at a user defined interval of ever N timesteps. This file is formatted as "custom" to include atom/molecule "id", "type", and 3D "*x*-", "*y*-", and "z-" axis atom positions; further constraints can also be applied. These outputted trajectories can then be visualized with software (e.g., VMD and Ovito), and post-processed for further data acquisition.

run: After setting all simulation initializations, definitions, etc., the "run" command relays the number of timesteps LAMMPS needs to simulate. Simulation durations typically range from 2,000,000 to 10,000,000 (2.0 ns to 10.0 ns), depending on the investigated area.

Data Acquisition and Post-Processing

Although LAMMPS has a variety of techniques and options to directly output values of interest (e.g., thermal conductivity, viscosity, etc.), these become unusable within complex systems having many different tasks and interactions being performed. Therefore, once simulations are complete with the desired information printed to output files, post-processing must be performed to gain a more in-depth perspective on simulation results and to correctly determine values of interest. This thesis employs the software of VMD, Ovito [153], Excel [154], OriginLab [155], and MATLAB [156]. VMD and Ovito are utilized for the visualization of system evolution and subsequent atom positions; Excel, OriginLab, and developed MATLAB codes are all used for sorting and calculating data.

VITA

Drew Champion Marable was born in Knoxville, TN, to the parents of Michael and Leslie Marable. His early childhood was spent in Mauriceville, TX, where he attended Mauriceville Elementary, and for a brief amount of time, Mauriceville Middle School, until his family was relocated back to East Tennessee. There, he attended North Middle School and continued to Lenoir City High School in Lenoir City, TN. Inspired by Mr. Keith Garrett's teachings of nuclear chemistry in his high school AP Chemistry class, Drew chose to pursue a degree in Nuclear Engineering at The University of Tennessee – Knoxville (UTK); in May of 2015, he obtained his Bachelor's of Science degree in Nuclear Engineering from UTK. He then decided to further and diversify his education by pursing a Master's of Science degree, and accepted a graduate research assistantship with Dr. Seungha Shin's Nanoscale Heat Transfer Laboratory, in the Department of Mechanical, Aerospace, and Biomedical Engineering at UTK. Drew is scheduled to graduate with a Master's of Science degree in Mechanical Engineering with a concentration in Thermal – Fluid Mechanics in May 2017.